SLAC-PUB-13999
April 2010

A Design Report of the Baseline for PEP-X: an Ultra-Low Emittance Storage Ring*

Karl Bane, Kirk Bertsche, Yunhai Cai, Alex Chao, Willian Corbett,
John Fox, Robert Hettel, Xiaobiao Huang, Zhirong Huang,
Cho-Kuen Ng, Yuri Nosochkov, Sasha Novokhatski,
Thomas Radedeau, Tor Raubenheimer, Claudio Rivetta,
James Safranek, John Seeman, Joachim Stohr, Gennady Stupakov,
Lanfa Wang, Min-Huey Wang, Uli Wienands, Liling Xiao
SLAC National Accelerator Laboratory, Stanford University
Menlo Park, CA 94025

Abstract

Over the past year, we have worked out a baseline design for PEP-X, as an ultra-low emittance storage ring that could reside in the existing 2.2-km PEP-II tunnel. The design features a hybrid lattice with double bend achromat (DBA) cells in two arcs and theoretical minimum emittance (TME) cells in the remaining four arcs. Damping wigglers are used to reduce the horizontal emittance to 86 pm-rad at zero current for a 4.5 GeV electron beam. At a design current of 1.5 A, the horizontal emittance increases, due to intra-beam scattering, to 164 pm-rad when the vertical emittance is maintained at a diffraction limited 8 pm-rad. The baseline design will produce photon beams achieving a brightness of 10^{22} (ph/s/mm^2/mrad^2/0.1% BW) at 10 keV in a 3.5-m conventional planar undulator. Our study shows that an optimized lattice has adequate dynamic aperture, while accommodating a conventional off-axis injection system. In this report, we present the results of study, including the lattice properties, nonlinear dynamics, intra-beam scattering and Touschek lifetime, RF system, and collective instabilities. Finally, we discuss the possibility of partial lasing at soft X-ray wavelengths using a long undulator in a straight section.

*Work supported by the Department of Energy under Contract No. DE-AC02-76SF00515.

Contents

Chapter 1

Executive Summary

The large circumference tunnel of PEP-II, its high power and low emittance injector, and its infrastructure, combined with the SLAC expertise in high-current operation of PEP-II, present a unique opportunity to design and build an ultra-low emittance, extremely high brightness next-generation synchrotron light source.

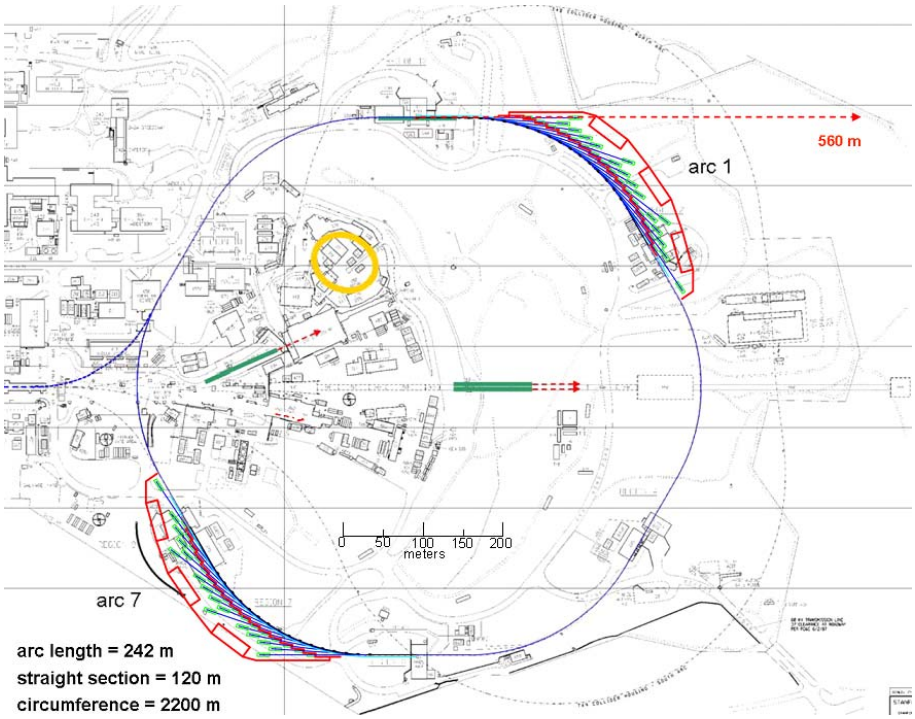

Figure 1.1: A conceptual layout of the PEP-X light source with two experimental halls containing 30 X-ray beamlines reaching a brightness of 10^{22} (ph/s/mm^2/mrad^2/0.1% BW) at 10 keV.

This future light source has a potential to reach high coherence in both transverse dimensions for multi-keV photons and to lase partially in a very long undulator at soft x-ray wavelengths. Achieving these features would make this storage ring-based light source very competitive to a source based on an energy recovery linac (ERL).

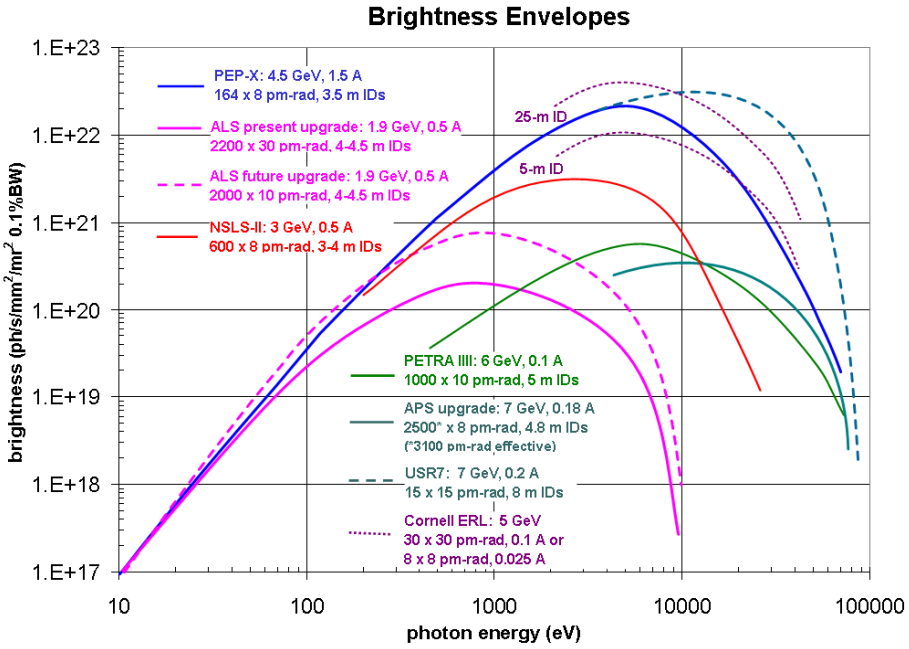

Figure 1.2: Approximate brightness envelopes for representative existing and future ultimate ring light sources assuming non-superconducting undulator lengths as specified in the figure. Higher brightnesses can be reached in these sources by using longer undulators and eventually superconducting undulators. Partial lasing in long undulators may enhance the brightness for soft x-rays at energies <1 keV. The approximate performance of the Cornell ERL [1] is shown for comparison.

Over the past year, we have firmly established a baseline design for PEP-X as an ultra-low emittance storage ring that could reside in the existing 2.2-km PEP-II tunnel. The main parameters of the design are tabulated in Table 1.1. The design features a hybrid lattice with DBA cells in two of the six arcs that provide a total of 30 straight sections for insertion device (ID) beam lines extending into two new experimental halls as illustrated in Fig. 1.1. The remaining four arcs contain TME cells to minimize the emittance. Damping wigglers are used to further reduce the horizontal emittance to 86 pm-rad at zero current for a 4.5 GeV electron beam. At a design current of 1.5 A, the horizontal emittance increases, due to intra-beam scattering, to 164 pm-rad when the vertical emittance is maintained at a diffraction limited 8 pm-rad.

The baseline design will produce photon beams achieving a brightness of 10^{22} (ph/s/mm^2/mrad^2/0.1% BW) at 10 keV in a 3.5-m conventional planar undulator. This brightness is approximately two orders of magnitude higher than the existing 3$^{\text{rd}}$ generation light sources such as ALS and APS and an order of magnitude higher than the NSLS-II and PETRA-III sources currently under construction or in commissioning. As one can see in Fig. 1.2, the design is also very competitive with the proposed ERL-based source at Cornell [2].

Table 1.1: Main parameters of the baseline design for PEP-X.

Energy, E [GeV]	4.5
Circumference, C [m]	2199.3167
Beam current, I [A]	1.5
Horizontal emittance, ϵ_x [pm·rad, 0/1.5 A]	86 / 164
Vertical emittance, ϵ_y [pm·rad]	8
Tunes, $\nu_x/\nu_y/\nu_s$	87.23/36.14/0.0077
Damping times, $\tau_x/\tau_y/\tau_s$ [ms]	20.3 / 21.2 / 10.8
RF frequency, f_{RF} [MHz]	476
Harmonic number, h	3492
Number of bunches, n_b	3154-3422
Bunch length, σ_z [mm]	3.0
Relative energy spread, σ_δ	$1.14 \cdot 10^{-3}$
Momentum compaction, α	$5.81 \cdot 10^{-5}$
Energy loss, U_0[MeV/turn]	3.12
RF voltage, V_{RF} [MV]	8.9
Damping wiggler length [m]	89.3
Length of arc ID straight [m]	4.0
Number of arc ID straights	30
β_x/β_y at low beta ID [m]	3.00 / 6.07
β_x/β_y at high beta ID [m]	16.04 / 6.27

Dynamic aperture both for on- and off-momentum particles is one of the major challenges in the design. The study shows that an optimized lattice, even with alignment and magnetic errors, has adequate acceptance to accommodate a conventional off-axis injection system based on the SLAC linac. The off-momentum aperture allows a minimum Touschek lifetime of a half hour, which is short but acceptable, provided that the powerful linac is used as its injector. Stored current constancy of 1% or less can be maintained with top-up injection every few seconds.

Collective instabilities, driven both by conventional impedance and coher-

ent synchrotron radiation, are evaluated for single bunch or multiple bunches in the ring. A detailed impedance model is constructed from the existing PEP-II cavities, resistive-wall, and a scaled version of the PEP-II components. Our study shows that the bunch current is limited by the vertical head-tail instability driven largely by the narrow resistive wall inside the undulators. For a 6-mm full gap, the single bunch threshold is 0.67 mA, a comfortable margin above the nominal 0.48 mA stored in each of 3154 bunches for 1.5-A operation. Similarly, the resistive-wall impedance also causes a growth rate of 0.14 ms (corresponding to approximately 19 revolution periods) in a coupled-bunch mode for a 1.5-A beam. Clearly, a bunch-by-bunch feedback system is necessary to damp down the vertical motion.

The design utilizes much of the existing infrastructure at SLAC, including the PEP tunnel, its high-power linac and low emittance injector, and the PEP-II RF system. Most importantly, the baseline design does not rely on any new technology developments and is therefore essentially ready to be built.

Our study covers all important aspects of accelerator physics, including the lattice properties, nonlinear dynamics, intra-beam scattering and Touschek lifetime, and collective instabilities. The study will provide a solid foundation and performance benchmark for any future design improvements or configuration ideas that could lead to the construction of the new light source.

Chapter 2

Lattice Design

PEP-X is designed to fit in the existing PEP-II tunnel. For this reason, it adopts the same ring geometry as PEP-II and has the same circumference of 2199.32 m. Fig. 2.1 shows schematic of the PEP-X ring layout with six arcs and six long straight sections which have the same length as in PEP-II. The arcs and the straight sections are denoted by the numbers 1 through 12 in this figure. Positions of the straight sections are kept identical to those in PEP-II, but radial coordinates in the arcs are slightly changed due to the new locations and strengths of the PEP-X bending magnets.

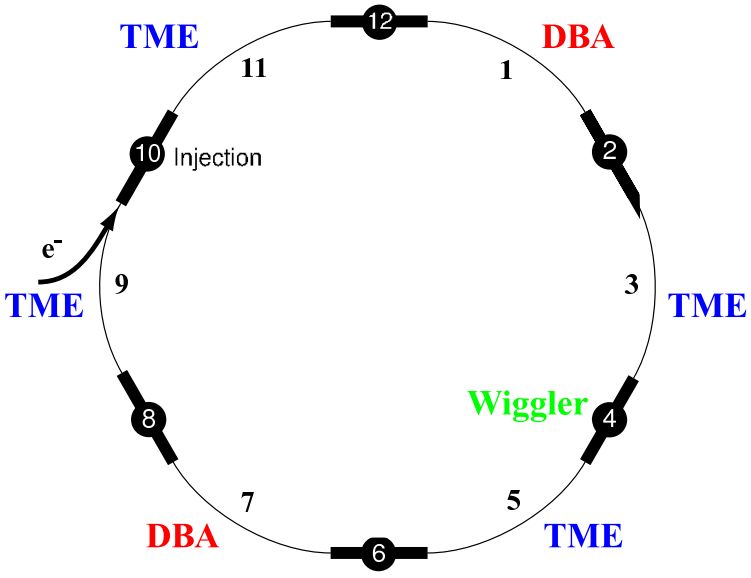

Figure 2.1: PEP-X layout with 2 DBA arcs, 4 TME arcs and 6 straight sections.

The PEP-II e^+e^- colliding machine had two vertically separated rings, where the 3.1 GeV Low Energy Ring (LER) was located on top of the 9

GeV High Energy Ring (HER). PEP-X will have only one ring, therefore it is more practical to locate it at the lower position of the PEP-II HER, about 1 m above the floor. The HER has another advantage over the LER because its magnets are designed for a higher beam energy. Therefore they are stronger and more suitable for potential reuse in PEP-X at 4.5 GeV. For these reasons, the HER is selected for conversion to PEP-X.

The goal of the PEP-X lattice design is to provide at least 24 dispersion free sections for undulator Insertion Devices (ID) and to attain an ultra low horizontal beam emittance in the range of 0.1 nm·rad at 4.5 GeV. To achieve the first goal, Double Bend Achromat (DBA) cells will be implemented in two arcs. They will have one ID straight section per cell. The selected location of the DBA cells in arcs 1 and 7 in Fig. 2.1 is based on the specifics of the PEP-II site geology and the location of existing facilities. The second goal of attaining the low emittance is achieved by using the Theoretical Minimum Emittance (TME) lattice in the other four arcs and a ∼90 m damping wiggler in a long straight section.

2.1 Double Bend Achromat Cells

The length of each arc is 243.2 m as determined by the ring geometry. The number of DBA cells per arc is defined by the cell length which is determined through optimization of the cell optical properties. An important advantage of shorter cells is that each arc can have more ID straights. The shorter cells also have a smaller bending angle θ per dipole and therefore can attain a lower emittance since it scales as $\epsilon_x \propto \theta^3$. The disadvantage is that the available space for IDs and magnets is reduced, which limits the optics flexibility. In the initial PEP-X study, two options have been compared: 16 and 12 DBA cells per arc. The phase advance per cell was chosen near $\pi/2 + n\pi$, which provides conditions for local compensation of second order geometric sextupole aberrations and chromatic perturbation of beta functions in every 4 cells. It was found that the only advantage of the 12 cell option with a longer cell is a longer ID straight. The estimated beam dynamic aperture and predicted photon brightness in both options were similar. Since a higher number of IDs per arc leads to a more cost efficient design, the option with 16 DBA cells per arc has been adopted.

One disadvantage of a standard DBA cell is that it does not provide much flexibility for variation of ID beta functions. That is due to the fact that the strengths of DBA quadrupoles are determined by the value of cell phase advance and the requirement for dispersion cancelation. In the case of 16 DBA cells per arc and optimized values of phase advance near $\mu_x = 3\pi/2$, $\mu_y = \pi/2$, the lowest beta functions at the center of ID straight are limited

to $\beta_x = 10.4$ m and $\beta_y = 8.0$ m. However, further reduction of the ID beta functions is desired for a higher brightness. This is achieved by converting the standard DBA cells into DBA supercells as described in the next section.

2.2 DBA Supercells

In order to provide the availability of low beta ID straights, the 16 standard DBA cells per arc were converted into 8 DBA supercells, keeping the same magnet positions and length of ID straights. In this case, each supercell consists of two standard DBA cells, where the quadrupole strengths are adjusted independently near the two ID straight sections. For a given phase advance per supercell, such a focusing adjustment can lower beta functions in one of the two ID straights, but the other will have higher beta functions to produce an "alternating beta" optics.

Magnet positions and optics functions in the PEP-X DBA supercell are shown in Fig. 2.2, where one of the two 4.0 m ID straights is located at the center and the other is split between the two ends of the supercell in this figure. The supercell is 30.422 m long and it is symmetric with respect to the center of either ID straights. Dispersion is locally cancelled at each ID straight. Beta functions at center of the low and high beta ID straights are adjusted to $\beta_x/\beta_y = 3.0/6.1$ m and 16.0/6.3 m, respectively. In total, the two DBA arcs have 16 low beta and 14 high beta ID straights. Each supercell contains 4 identical combined function dipole magnets, 12 quadrupoles, 6 chromatic sextupoles and 4 harmonic sextupoles. The quadrupoles are arranged in 5 independent families for phase and beta adjustment, and the chromatic sextupoles have two independent families. The chromatic sextupoles are located in regions with non-zero dispersion for correction of linear chromaticity. The harmonic sextupoles are placed between the quadrupoles on either side of the ID straights where the dispersion is zero. They are used to minimize the amplitude dependent tune shift as well as the 3rd and 4th order resonance effects created by the chromatic sextupoles. The additional focusing provided by the combined function dipoles improves the optics flexibility. The 8 supercells in each DBA arc are periodic, except that at each end of the arc the strengths of the last two quadrupoles are adjusted for a match to the adjacent long straight sections.

Optimization of the supercell optics involved a compromise between attaining a low emittance value, low beta functions in the ID straights, maximum momentum compaction factor and maximum dynamic aperture. The low emittance is achieved by minimizing the H-invariant function in the supercell dipoles, and the momentum compaction is increased by maximizing the dipole length. The longer dipole also helped to further reduce the

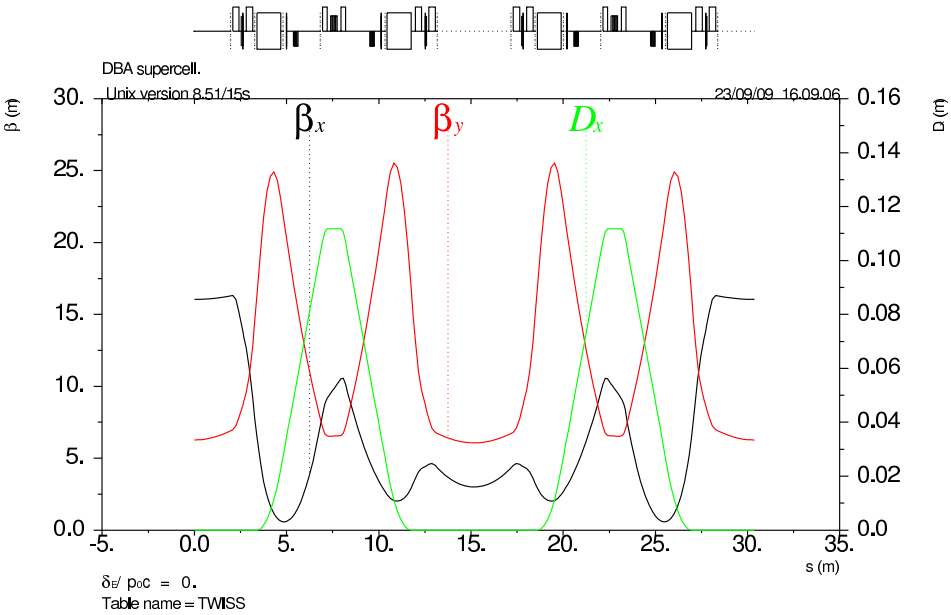

Figure 2.2: Lattice functions in one DBA supercell.

emittance generated in the supercells. Dynamic aperture was maximized by empirically optimizing the strengths of sextupoles and the supercell phase advance. Initially, the phase advance was set to near $\mu_x = 3\pi$, $\mu_y = \pi$ which provides $-I$ transformation between the same family sextupoles resulting in compensation of the 3rd order sextupole resonance effects. The high horizontal phase advance is needed for compensation of horizontal dispersion locally in each half of the supercell, while the vertical phase can be set to a lower value to reduce quadrupole strengths, chromaticity and sensitivity to magnet errors. However, the exact $n\pi$ phase value would amplify the 4th order resonance effects created by the sextupoles. To optimize the phase, particle tracking simulations were performed using LEGO [3]. They showed that dynamic aperture is maximized when the phase advance is slightly detuned from $n\pi$ to $\mu_x = 3\pi\,(1 + \frac{1}{64})$, $\mu_y = \mu_x/3$. This achieves a compromise in compensation of the 3rd and 4th order resonance effects created by the supercell sextupoles.

2.3 Theoretical Minimum Emittance Cells

The main function of the other four arcs is to minimize the PEP-X emittance while maintaining sufficiently large dynamic aperture and maximizing the momentum compaction factor. This is achieved by using a TME cell optics which is capable of reaching three times lower emittance than the DBA cells. Similar to the DBA optics, the TME momentum compaction is increased

by maximizing the length of the dipole magnets. The latter also helped to further reduce the TME generated emittance. By design, the TME cell is not suitable for insertion devices because of a non-zero dispersion and limited free space.

Each of the four TME arcs will contain 32 regular and 2 matching cells. The optics functions in one 7.297 m regular TME cell are shown in Fig. 2.3. The cell is symmetric and it contains one 3.5 m long dipole magnet, 4 quadrupoles and 3 chromatic sextupoles. The quadrupoles are arranged in two independent families for phase adjustment, and the sextupoles have two families for chromaticity correction. The short TME cell has the advantage of a small bending angle per dipole which helps to reduce the TME generated emittance as $\epsilon_x \propto \theta^3$. Phase advance in the TME cell is chosen near $\mu_x = 3\pi/4$, $\mu_y = \pi/4$ which provides nearly $-I$ transformation between identical sextupoles separated by 4 cells for compensation of their second order geometric aberrations. Since this phase value is relatively low, it does not yield the lowest emittance, but it provides a lower chromaticity and sensitivity to magnet errors which help to attain a larger dynamic aperture. Similar to the DBA cells, the optimal value of the TME phase advance was determined in dynamic aperture tracking simulations. As a result, it is detuned by less than a degree per cell to $\mu_x = (3\pi/4)\,(1 - \frac{1}{192})$, $\mu_y = \mu_x/3$ to achieve a compromise in compensation of the 3rd and 4th order resonance effects generated by the TME sextupoles. This small detuning accumulates to $\pi/2$ in the horizontal plane for all 128 TME cells in the ring.

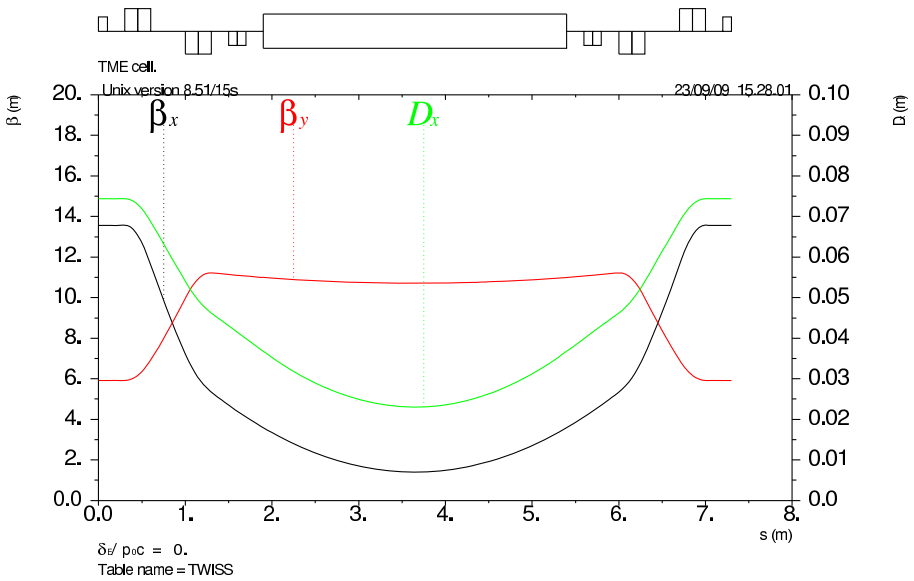

Figure 2.3: Lattice functions in one TME cell.

The TME arc has a matching cell at each arc end which is designed to cancel the TME dispersion, help with the beta match and fit the arc geometry to the existing HER ring. Fig. 2.4 shows the optics functions in one standard and one dispersion suppressor cells at end of the TME arc. The dispersion suppressor cell is 4.846 m long and it contains two quadrupoles and a 35% shorter dipole than in a regular cell.

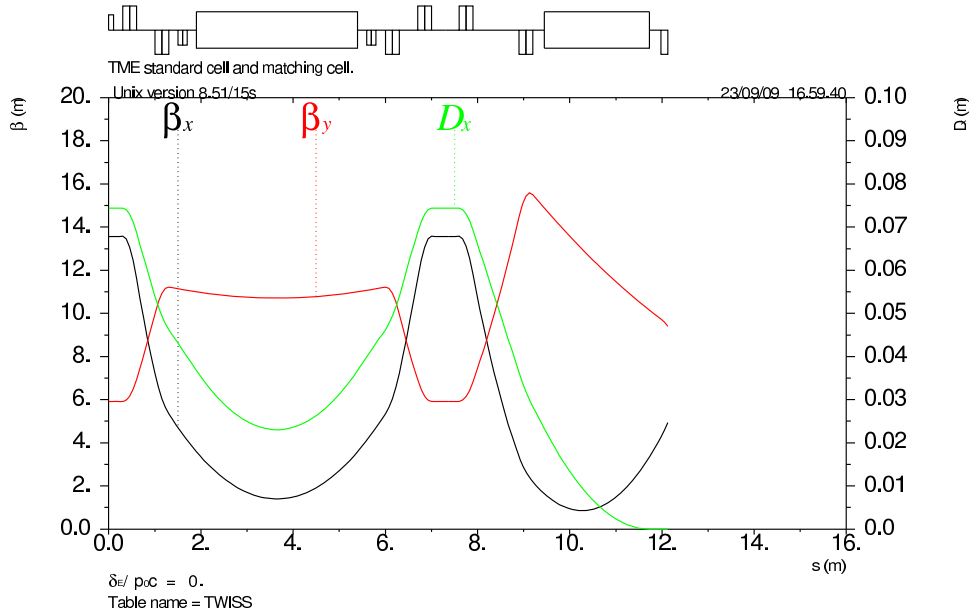

Figure 2.4: Lattice functions in one regular and one dispersion suppressor cells at end of TME arc.

2.4 Long Straight Sections

PEP-X long straight sections have the same length (123.353 m) and the same geometric position as in the PEP-II HER. They will contain the injection system, the RF accelerating cavities, the damping wiggler, and the optics systems for betatron tune adjustment and coupling correction. The injection system will be located in the straight section-10 as shown in Fig. 2.1. The other five straights have identical FODO lattice with 21 quadrupoles per section as shown in Fig. 2.5. The four cells at the center of these straights are exactly periodic, while the cells at either end are used for matching to the adjacent DBA or TME arcs. The first and the last quadrupoles in this FODO lattice are moved closer to the beginning and end of the straight section in order to minimize the matched beta functions. The straight section-4 will contain a ∼90 m wiggler. Therefore the quadrupole strengths in this straight section are adjusted to compensate for the wiggler focusing. The five FODO

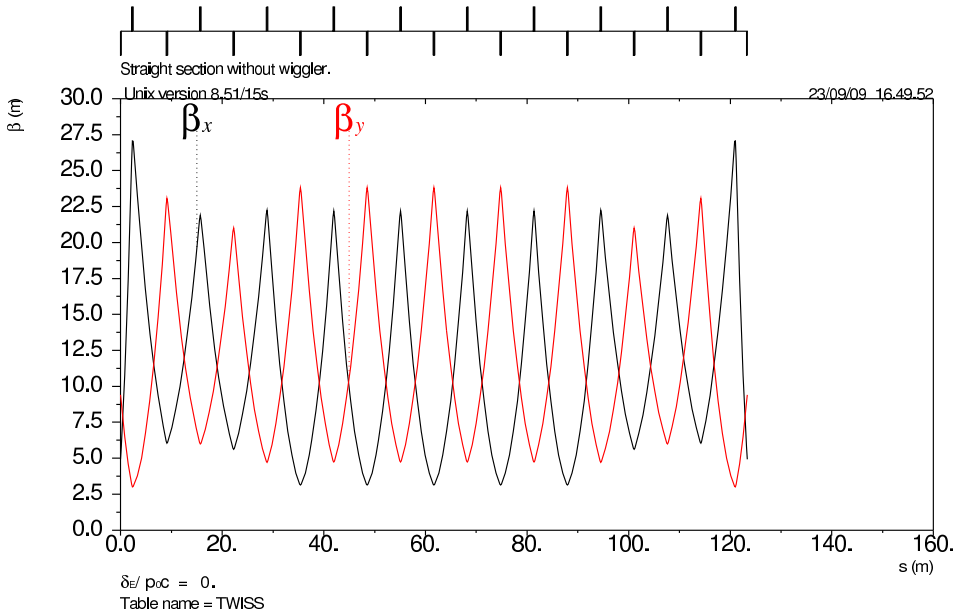

Figure 2.5: Beta functions in a long straight section without wiggler.

straight sections are matched to the same phase advance which can be varied for adjustment of the PEP-X betatron tune.

2.4.1 Wiggler Straight

The DBA and TME arcs yield the horizontal emittance of 0.379 nm·rad at 4.5 GeV. Further emittance reduction requires a strong damping wiggler placed in a region of zero dispersion. Presently, the wiggler is inserted in the straight section-4 as indicated in Fig. 2.1. Alternatively, the wiggler could be split in two parts and accommodated in sections 2 and 6 without significant change to beam parameters. Quadrupole strengths in the wiggler straight section are adjusted to take into account the wiggler focusing while keeping the same phase advance as in the other FODO straights. Therefore, the wiggler beta functions, shown in Fig. 2.6, are somewhat different compared to those of the straights without wigglers. In order to fit into ∼6.3 m gaps between the quadrupoles, the 89.325 m long wiggler is split into 18 identical sections, where each 4.9625 m long section is comprised of 50 wiggler periods. For a strong damping effect, the wiggler has a short 10 cm period and a 1.5 T vertical field as explained in Section 1.6. The present wiggler model uses a periodic sequence of alternating field short dipoles separated by short gaps. Horizontal dispersion is periodic in each 4.9625 m section, as shown in Fig. 2.7, and it is canceled outside of these sections. The wiggler also creates a local horizontal orbit which has the same form and amplitude as

the dispersion.

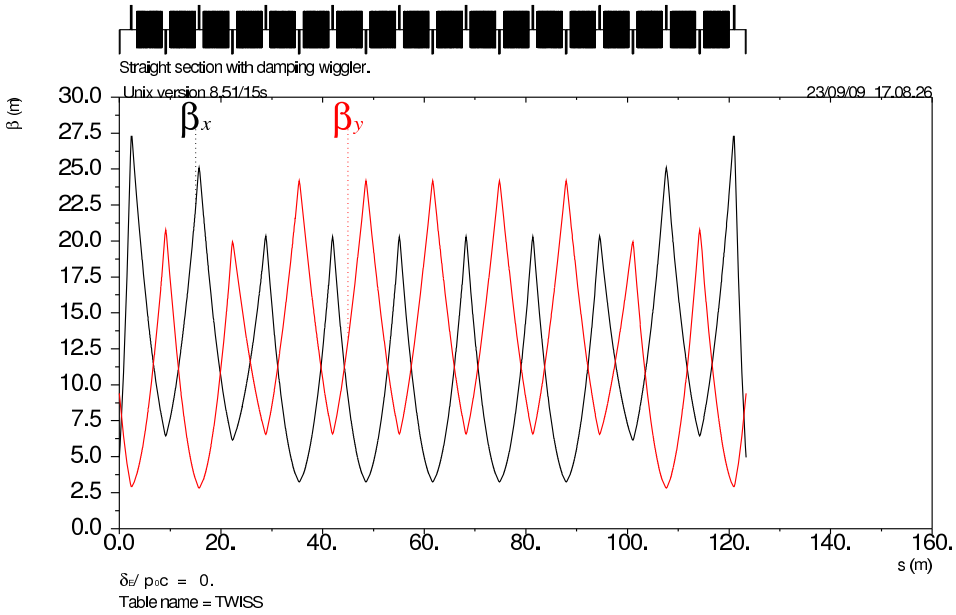

Figure 2.6: Beta functions in the straight section with wiggler.

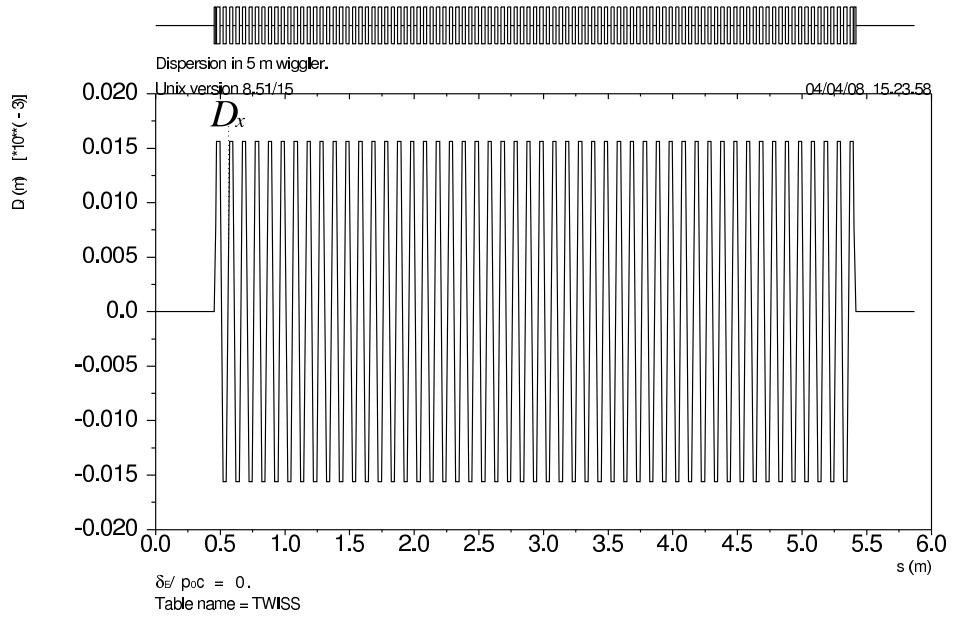

Figure 2.7: Horizontal dispersion in 4.9625 m wiggler section in a half FODO cell.

2.4.2 Injection Straight

The PEP-X injection system adopts the lattice design used in the PEP-II HER injection straight section-10, but it changes the injection from the vertical to the horizontal plane. In addition to the existing HER magnets, four additional quadrupoles are included at the straight ends to improve beta match to the adjacent TME arcs. Beta functions and positions of injection bump magnets in the injection section are shown in Fig. 2.8. The injection point is at the center of the straight where the horizontal beta function is increased to $\beta_x = 200$ m in order to enlarge the size of the horizontal acceptance aperture for the injected beam as discussed in Section 1.7. This acceptance aperture is shifted as close as possible to the injected beam by moving the stored beam trajectory towards the injection septum using the injection bump magnets and pulsed kickers. The four DC magnets can control both the amplitude and angle of the stored beam closed bump, and the two identical kickers separated by 180° in horizontal phase provide an additional symmetric bump.

2.5 Complete Ring Lattice

Lattice functions in the complete PEP-X ring are shown in Fig. 2.9. The chosen order of DBA and TME arcs provide symmetry but, depending on other considerations it can be changed without affecting the main beam parameters. The PEP-X betatron tune dependence on the relative momentum error $\Delta p/p$ is presented in Fig. 2.10 where the linear chromaticity is set to zero. It shows good compensation of the chromatic tune variation in the range of $\Delta p/p = \pm 2.5\%$. This helps to increase the optical momentum acceptance by keeping the off-momentum particles near the design tune and away from strong resonances.

The number of PEP-X dipole, quadrupole and sextupole magnets is shown in Table 2.1. The highly packed TME arcs contain most of the magnets. The orbit correction system will include approximately one dipole corrector and one BPM per quadrupole. The estimated number of independent power supplies is 2 for DBA and TME dipoles, ∼170 for quadrupoles and 5 for sextupoles. The large number of quadrupole supplies is due to the assumption that all insertion devices in the DBA arcs will be different and therefore require a different optical match. A few additional independent sextupole power supplies may be considered for more correction flexibility. The present PEP-X lattice uses the existing PEP-II magnets in the injection section. More existing magnets could be potentially utilized, especially in the long straight sections where the available space is sufficient for the PEP-II quadrupoles.

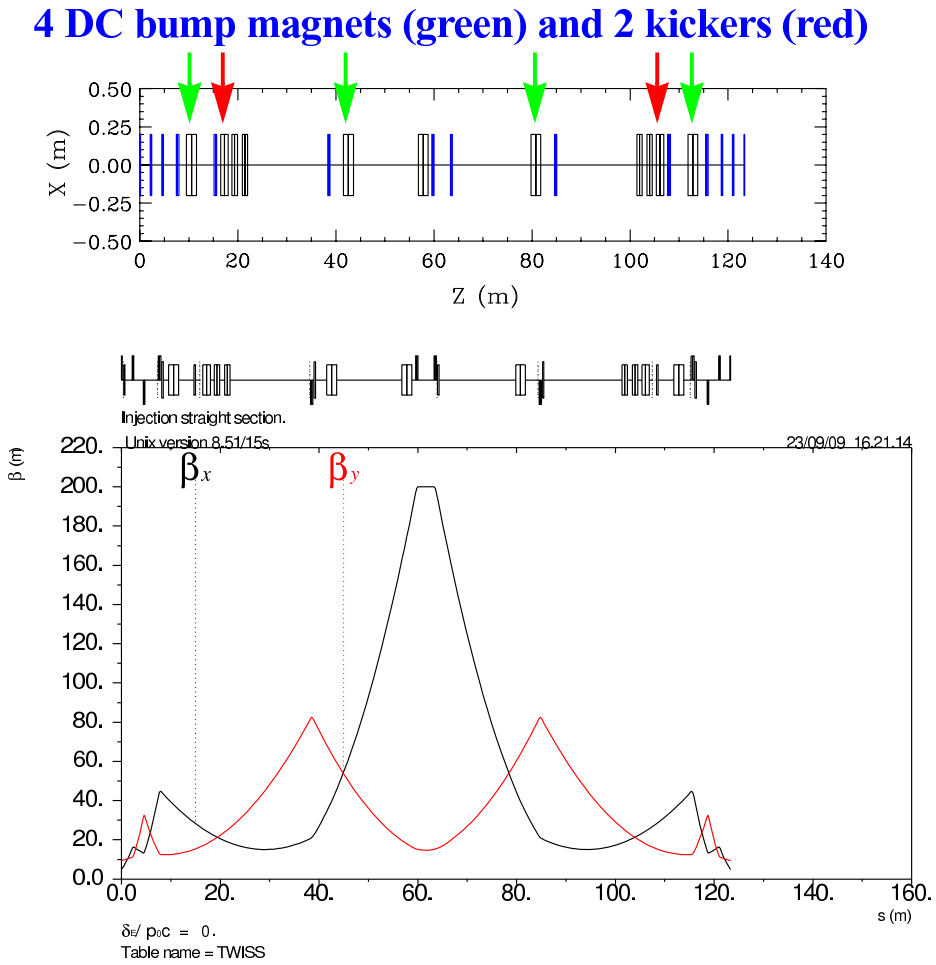

Figure 2.8: Beta functions and location of bump magnets in the injection section.

2.6 Damping wiggler

Emittance generated in the DBA and TME arcs is 0.379 nm·rad at 4.5 GeV. Further reduction to the desired level of 0.1 nm·rad requires a damping wiggler in a region with zero dispersion. The wiggler parameters must be optimized in order to achieve maximum damping efficiency.

The equilibrium horizontal emittance in a ring with a damping wiggler is given by [4]:

$$\epsilon_w = C_q \frac{\gamma^2}{J_x} \frac{I_5^0 + I_5^w}{I_2^0 + I_2^w}, \tag{2.1}$$

where

$$I_2 = \oint \frac{ds}{\rho^2}, \quad I_5 = \oint \frac{\mathcal{H}_x}{\rho^3} ds, \tag{2.2}$$

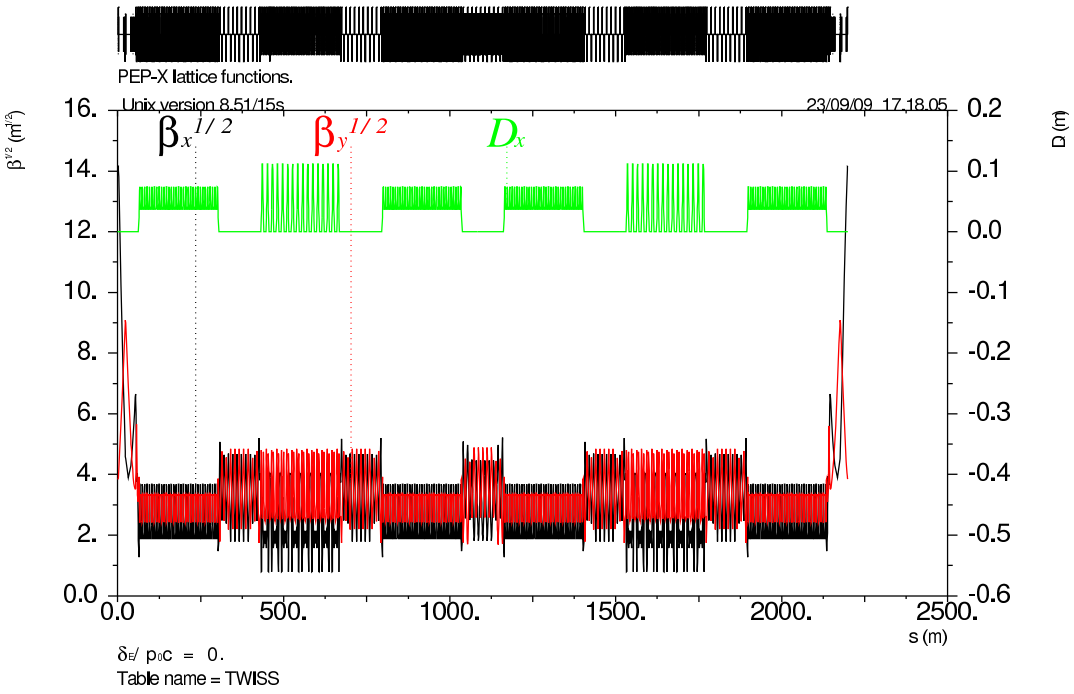

Figure 2.9: Lattice functions in the complete PEP-X ring starting from injection point.

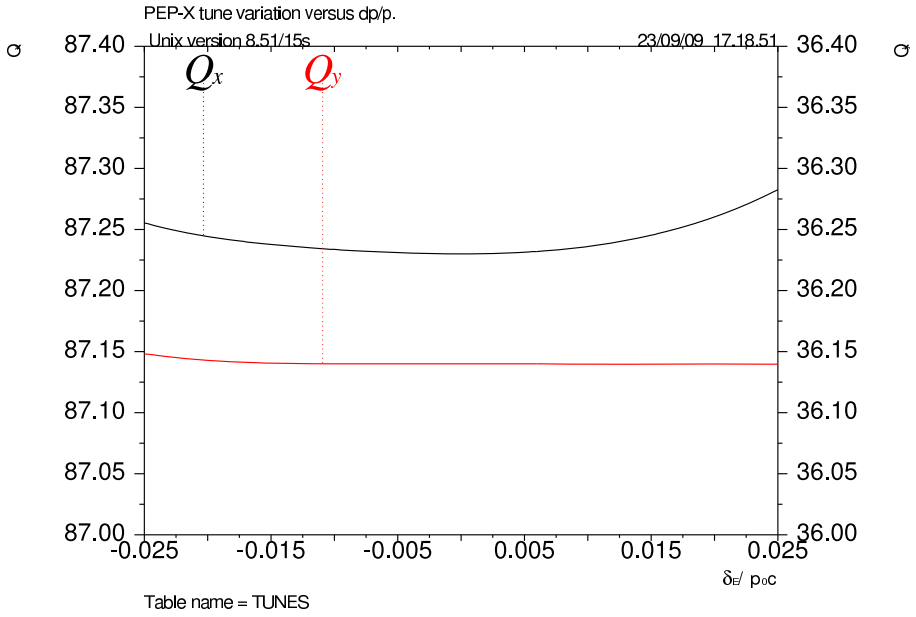

Figure 2.10: PEP-X betatron tune as a function of relative momentum error $\Delta p/p$.

Table 2.1: PEP-X magnet quantities.

1.3 m DBA combined function dipoles	64
3.5 m TME regular dipoles	128
2.275 m TME matching dipoles	8
Total dipoles	**200**
DBA cell quadrupoles	192
TME regular cell quadrupoles	512
TME matching cell quadrupoles	16
FODO straight quadrupoles	105
Injection straight quadrupoles	14
Total quadrupoles	**839**
DBA cell chromatic sextupoles	96
DBA cell harmonic sextupoles	64
TME cell chromatic sextupoles	384
Total sextupoles	**544**

and

$$\mathcal{H}_x = \beta_x {\eta'_x}^2 + 2\alpha_x \eta_x \eta'_x + \gamma_x \eta_x^2, \tag{2.3}$$

$C_q = 3.83 \cdot 10^{-13}$ m, γ is a Lorenz factor, J_x is the horizontal damping partition number, ρ is the bending radius, α_x, β_x, and γ_x are the Courant-Synder parameters, η_x and η'_x are the dispersion and its angle, and the indices "0" and "w" correspond to integration over ring dipoles and wiggler magnets, respectively. For a lattice with one type of ring dipole and one type of wiggler, Eq. 2.1 can be written explicitly in the form of emittance ratio [4]:

$$\frac{\epsilon_w}{\epsilon_0} = \frac{1 + \frac{4C_q}{15\pi J_x} N_p \frac{<\beta_x>}{\epsilon_0 \rho_w} \gamma^2 \frac{\rho_0}{\rho_w} \theta_w^3}{1 + \frac{1}{2} N_p \frac{\rho_0}{\rho_w} \theta_w}, \tag{2.4}$$

where ϵ_0 is the emittance without damping wiggler, $< \beta_x >$ is the average horizontal beta function in the wiggler, N_p is the number of wiggler periods, ρ_w is the bending radius at the wiggler peak field, ρ_0 is the bending radius in the ring dipole, $\theta_w = \lambda_w / 2\pi\rho_w$ is the peak trajectory angle in the wiggler, and λ_w is the wiggler period length. The wiggler efficiency for emittance reduction, therefore, is determined by the wiggler period length λ_w, the value of wiggler peak field B_w, and the total wiggler length $L_w = N_p \lambda_w$.

The PEP-X lattice has two main types of ring dipoles. Therefore the general Eq. 2.1 was used for analytic evaluation of emittance and its dependence on wiggler parameters. The results of this calculation are presented

in Fig. 2.11 which shows the emittance ratio ϵ_w/ϵ_0 as a function of total wiggler length for a 1.5 T wiggler peak field and various values of wiggler period length, assuming wiggler location in the PEP-X long straight section. It indicates that the emittance reduction is most efficient for a wiggler length

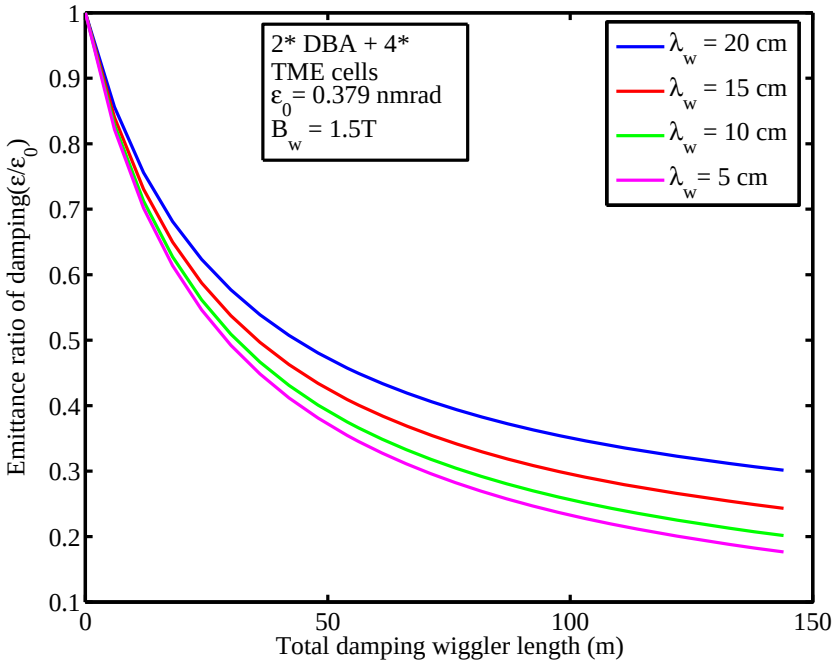

Figure 2.11: Relative emittance reduction, calculated using Eq. 2.1, as a function of total wiggler length for various values of wiggler period length and 1.5 T wiggler peak field.

within ∼100 m. Such a wiggler can fit into one PEP-X long straight section. Fig. 2.11 also shows that a shorter wiggler period results in more damping, but the rate of emittance reduction gradually decreases as the wiggler period becomes shorter and shorter. Fig. 2.11 indicates that for wiggler period of $\lambda_w \sim 10$ cm and wiggler length fitting into one PEP-X long straight section, there is enough damping to reach the desired 0.1 nm·rad emittance. This was later confirmed by numeric calculation using MAD8 [5]. For these reasons and taking into account the available space in the straight section, the total wiggler length was chosen to be $L_w = 89.325$ m.

For lattice symmetry reasons, the wiggler is inserted in the straight section-4, where it is located directly opposite to the injection section-10, thus dividing the ring in two mirror symmetric halves each containing two TME and one DBA arcs. Alternatively, the wiggler may be split into two parts and inserted in sections 2 and 6. In order to fit into ∼6.3 m drifts between the

straight section quadrupoles, the wiggler is split into 18 identical sections, where each 4.9625 m long section is comprised of 50 wiggler periods as shown in Fig. 2.7.

The optimal values of wiggler period length and peak field are determined based on the Eq. 2.1 calculations in Fig. 2.12 and 2.13. Fig. 2.12 presents the emittance ratio ϵ_w/ϵ_0 versus wiggler peak field for various values of wiggler period length. It demonstrates that a stronger damping requires a shorter wiggler period and a higher peak field. However, these conditions require a smaller wiggler gap as illustrated in Fig. 2.13 for a hybrid magnet design. A disadvantage of a small gap is that it reduces the wiggler vertical aperture which results in a larger resistive wall impedance and smaller beam vertical acceptance. The latter may lead to a beam loss and reduction of beam lifetime. To limit these unwanted effects, the wiggler peak field and period length are chosen to be $B_w = 1.5$ T and $\lambda_w = 10$ cm, respectively. These parameters are achievable using the existing magnet technology.

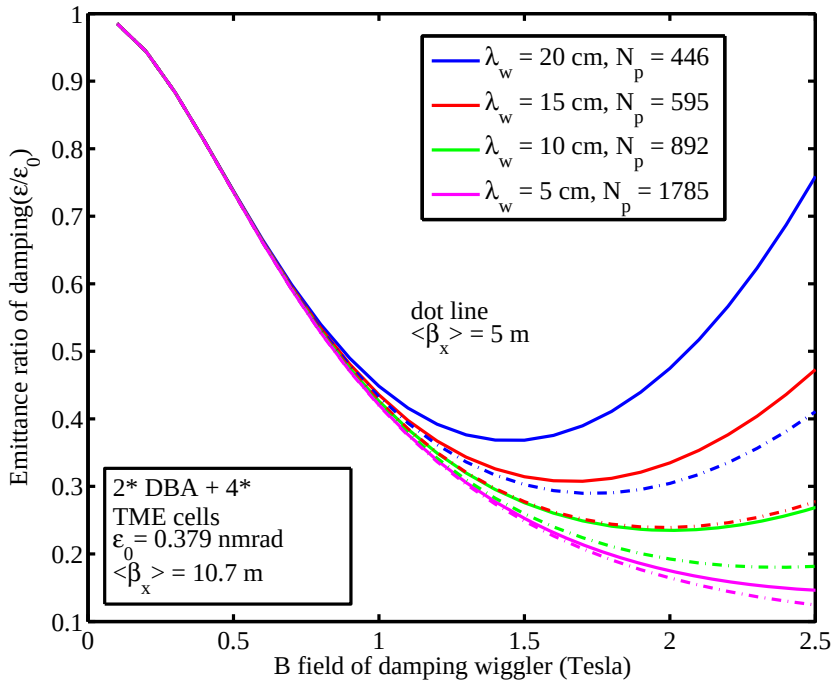

Figure 2.12: Relative emittance reduction, calculated using Eq. 2.1, as a function of wiggler peak field for various values of wiggler period length, $L_w = 89.3$ m, $\epsilon_0 = 0.379$ nm·rad, $< \beta_x >= 10.7$ m (solid) and 5 m (dash-dot), and $J_x = 1$.

The present wiggler model in the PEP-X lattice uses a periodic sequence

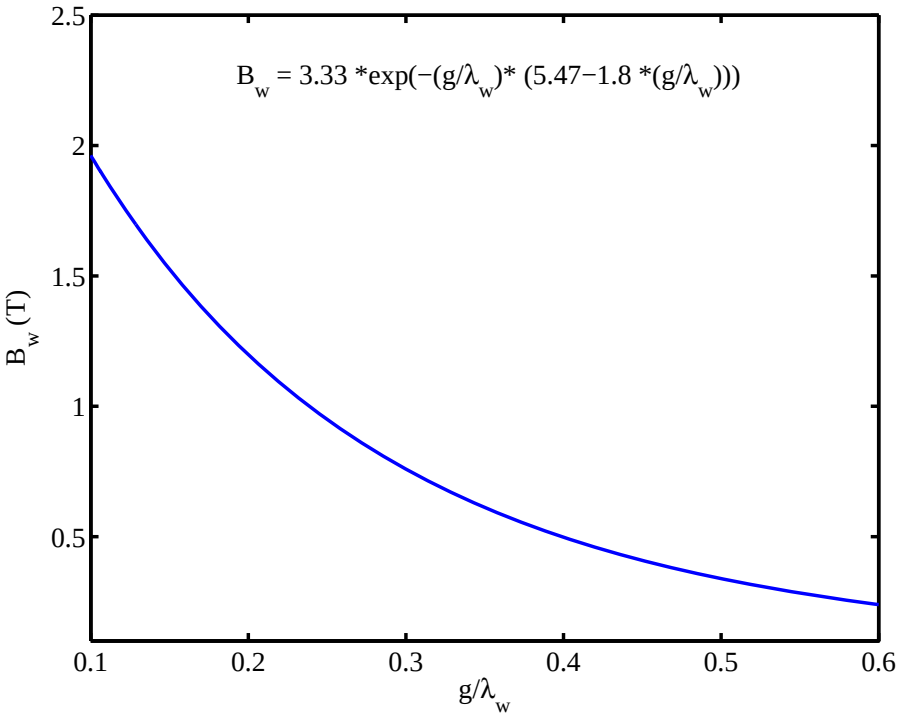

Figure 2.13: Wiggler field versus full wiggler gap g for hybrid magnet design.

of short 2.5 cm dipoles with alternating polarity separated by 2.5 cm gaps. Parameters of the PEP-X wiggler are summarized in Table 2.2, where the damping wiggler is inserted in straight section-4.

Table 2.2: PEP-X wiggler parameters, where g is a full wiggler gap and the emittance is at zero current as calculated by MAD8.

L_w (m)	λ_w (cm)	B_w (T)	g (mm)	ϵ_w (pm·rad)
89.325	10	1.5	15.4	85.7

The damping wiggler creates various negative effects on the PEP-X beam. It increases the rms beam energy spread from 5.5×10^{-4} to 1.14×10^{-3} as calculated by MAD8. It also increases radiation energy loss per turn U_0 from 0.52 MeV to 3.12 MeV resulting in a total beam power loss of 4.68 MW at 1.5 A beam current. This will require additional RF power and special care to deal with the radiation power in the wiggler. A simple estimate of power handling indicates that the 89.325 m wiggler may need to be split into two parts and placed in separate straight sections. Finally, the effects of

intrinsically non-linear fields in the wigglers may reduce the beam dynamic aperture.

2.7 Injection

The PEP-X injection scheme adopts the design of the PEP-II HER except the injection will be changed from the vertical to horizontal plane in order to avoid injected beam oscillations within the small vertical aperture of the insertion devices. The injection system will be located in the straight section-10 as shown in Fig. 2.1. The corresponding lattice layout and beta functions are shown in Fig. 2.8. The PEP-II system includes four DC bump magnets for providing a closed bump with adjustable amplitude and angle for the stored beam at the injection point at the center of the straight section. In addition, two identical pulse kickers, separated 180 degrees apart in horizontal phase, create an additional transient offset.

The diagram of the injection scheme in the horizontal phase space at the injection point is shown in Fig. 2.14. The stored beam horizontal acceptance A_x is represented by the large ellipse with the half-widths of

$$X_A = \sqrt{A_x \beta_x}, \quad X'_A = \sqrt{A_x/\beta_x}, \tag{2.5}$$

where X_A is dynamic aperture and β_x is the ring beta function at the injection point. The septum which provides the last kick for the injected beam is positioned at the outside edge of the dynamic aperture. This location avoids an effective reduction of the dynamic aperture while minimizing the required amplitude for the stored beam injection bump.

In order to obtain the maximum acceptance area for the injected beam on the outside of the septum, the stored beam must be positioned near the septum during injection. This is achieved by an injection bump created by the injection kickers. For minimal beam perturbation and loss at the septum, the minimal distance from the center of the bumped stored beam to the edge of the septum is specified to be $8\sigma_x$ of the stored beam size, where $\sigma_x = \sqrt{\beta_x \epsilon_x}$ and ϵ_x is the horizontal emittance of the stored beam. The septum effective width $W_s = 3$ mm is determined by 1 mm physical thickness and 1 mm allowance for stray field on each side.

Similarly, to minimize the initial injected beam oscillations in the ring, the distance from the center of the injected beam to the septum edge is specified to be $3\sigma_{xi}$, where $\sigma_{xi} = \sqrt{\beta_{xi}\epsilon_{xi}}$ and β_{xi}, ϵ_{xi} are the horizontal beta function and emittance of the injected beam. Therefore, the required minimal size of the stored beam dynamic aperture for injection is

$$(X_A)_{min} = 8\sigma_x + 6\sigma_{xi} + W_s, \tag{2.6}$$

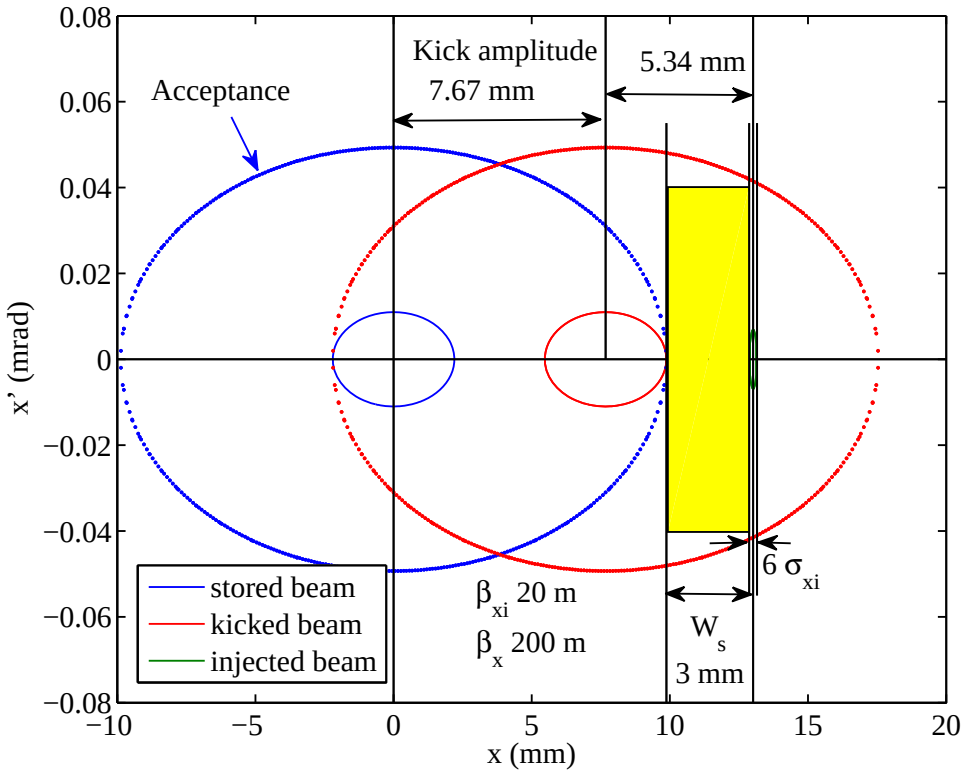

Figure 2.14: Injection phase space diagram showing the stored beam acceptance, the kick amplitude, the effective size of septum and the sizes of the stored and injected beams.

and the corresponding minimal ring acceptance is

$$(A_x)_{min} = \left(8\sqrt{\epsilon_x} + 6\sqrt{\epsilon_{xi}\beta_{xi}/\beta_x} + W_s/\sqrt{\beta_x}\right)^2. \tag{2.7}$$

Eq. 2.7 shows that a large value of ring β_x at the injection point helps to relax the requirement for large ring acceptance by reducing the relative width of the septum and relative injected beam size. The latter can be further reduced by using a lower beta function β_{xi} of the injected beam; however this would increase the injected beam divergence $\sqrt{\epsilon_{xi}/\beta_{xi}}$. Therefore β_{xi} must be optimized for a best match of the injected beam phase space to the ellipse of the stored beam acceptance.

The injection parameters are optimized to be compatible with a large stored beam emittance $\epsilon_x = 0.379$ nm·rad without the damping wiggler. This requires a larger minimal ring acceptance as defined in Eq. 2.7. The

ring horizontal beta function at the injection point is set to $\beta_x = 200$ m, the same as in PEP-II. This value increases the horizontal dynamic aperture a factor of 3 compared to the rest of the ring. Fortunately, the quadrupoles at this high beta peak are rather weak and their generated chromaticity does not exceed the chromaticity from regular arc quadrupoles. With these parameters, the stored beam size at the injection point without wiggler is $\sigma_x = 0.275$ mm. The horizontal dynamic aperture is $X_A = 9.87$ mm as shown in Fig. 3.4 in Chapter 3, and the injection bump amplitude is 7.67 mm as shown in Fig. 2.14. The injection bump is assumed to be produced only by the two identical pulse kickers without the DC bump magnets, where the required strength of each kicker is 1.65 T-m at 4.5 GeV.

For maximum injection acceptance, PEP-X will use an injector with a low normalized beam emittance of $\gamma\epsilon_{xi} \approx 1$ μm·rad, similar to the LCLS injector. In this case, the injected beam beta function is optimized to be $\beta_{xi} \approx 20$ m for a best match to the ring acceptance ellipse. At 4.5 GeV energy, this results in a very small injected beam size $\sigma_{xi} = 0.047$ mm. The corresponding required minimal size of the injection dynamic aperture in Eq. 2.6 is $(X_A)_{min} = 5.48$ mm, well below the PEP-X dynamic aperture of 9.87 mm. This gives ample room for the injected beam and sufficient margin for uncertainties due to the effects of errors not fully included in this analysis.

Chapter 3

Single Particle Dynamics

In order to reach the small equilibrium emittance of achromatic lattice, strong quadrupoles are inevitably needed to reduce dispersion and beta function at dipole magnets. As a result, sextupoles, to correct the natural chromaticity to zero or slightly positive to overcome the head-tail instability, become also stronger. However the presence of strong sextupoles means the introduction of high nonlinearity into the lattice. The nonlinear effects driven by such strong chromatic sextupoles can result in a severe decrease of dynamic aperture. Achieving a large dynamic aperture for on-axis injection and adequate Touschek beam lifetime becomes extremely challenging for a strongly focusing lattice.

In the process of achieving the desired dynamic aperture for the PEP-X design, several guidelines have been applied to minimize the impact of nonlinear effects due to the chromatic correction sextupoles. First, we minimized the strengths of the sextupole required by the linear chromaticity correction by placing the sextupoles at the location where the dispersion is large and the beta functions are orthogonal. Second, we carefully selected the phase advances in TME and DBA cell to minimize the integrated nonlinear effects generated by the sextupoles periodically located in the entire ring. Due to the periodicity of the sextupoles the phase advance between sextupoles could be arranged to cancel certain terms of these nonlinear effects. In a lattice made of n identical cells with $n > 3$ and having a total phase shift of a multiple of 2π, all second order geometrical aberrations will be canceled [6]. Third, we chose the global tunes ν_x, ν_y in the tune diagram to avoid the nonlinear resonances generated by strong sextupoles. A good pair of working tunes should have enough distance away from the major resonance lines in the tune diagram to take into consideration of tune shifts due to the nonlinear effects. Finally, additional harmonic sextupole families, located in the dispersion free section without affecting the linear chromaticity, are used to reduce the tune footprint and to further control the nonlinear effect.

A total length of 89.3 m long damping wigglers are added to achieve the design goal of the emittance of less than 100 pm. The impact of the damping wigglers is investigated. A model of a damping wiggler including the non-linearity is established to study the effect of damping wigglers on the dynamic aperture.

In general, stronger magnets require tighter tolerances of magnetic and alignment errors in the lattice. Our study provides a guideline to the specification of such tolerances. In particular, we studied the effects of magnet multipole errors on the beam dynamics. Correction schemes and simulations to correct the orbit and optics errors are investigated as well.

3.1 Sextupole Scheme and Dynamic Aperture of Bare Lattice

The main purpose of putting sextupoles in the lattice design is to correct the linear chromaticities produced by quadrupoles. The linear chromaticity and sextupole correction is given by

$$\xi_{x,y} = \mp\frac{1}{4\pi}\sum_{k=1}^{N}[(b_2\ell)_k - 2(b_3\ell)_k\eta_{x,k}]\beta_{(x,y),k}, \tag{3.1}$$

Where $b_2\ell$, $b_3\ell$ are the integrated quadrupole and sextupole strengths, and β and η are the beta function and dispersion, and k indicates the different locations of quadrupoles or sextupoles.

The linear chromaticities of the lattice are -138.9 and -78.7 of the horizontal and vertical respectively. There are four families of sextupoles for chromatic correction. One pair named SD, SF are in the TME cell and the other pair SD1, SF1 are in the DBA cell. All the sextupoles are located where the dispersion is comparatively large and the beta functions are well separated as shown in Fig 2.4, 2.2.

Both the strengths of nonlinear resonances and the tune shift terms depend strongly on the cell tune. Therefore the phase advance of a unit cell is chosen to cancel or reduce theses terms after a few unit cells [6]. Phase advances in the TME cell are chosen near $\mu_x = 3\pi/4$ and $\mu_y = \pi/4$ which provide nearly I transformations in both planes for every 8 cells to cancel the second order geometric aberrations. Similarly for the DBA supercells the optimized values of phase advances are chosen near $\mu_x = 3\pi$ and $\mu_y = \pi$. While the lower order resonance terms are canceled out by symmetry for these cell phase advances, the higher order term like the fourth order resonance in the DBA supercells will be amplified over many cells. The lattice

must be slightly detuned, which compromises somewhat the cancelations of the driving terms of third-order resonances. Another reason to detune the cell tune(cell phase advance divided by 2π) away from a rational tune is taking into consideration imperfections of magnet fabrication and engineering tolerances. The imperfections of magnet will introduce higher order magnetic field other than sextupole. Dynamic aperture tracking simulation is used to optimize the phase advance of a unit cell. According to the simulation results the phase advances of the TME cell are detuned by less than a degree to $\mu_x = (3\pi/4)(1 - \frac{1}{192})$, $\mu_y = \mu_x/3$ and the phase advances of the super DBA cell are set to $\mu_x = 3\pi(1 + \frac{1}{64})$, $\mu_y = \mu_x/3$.

The linear chromaticities are corrected to zero by using SD, SF, SD1 and SF1. At the beginning the SD, SF are set to compensate the linear chromaticity of TME cells and the SD1, SF1 to compensate the linear chromaticity of DBA cells. However we find these are not the best settings. We change the strengthes of SF1 and SD1 systematically and then use SF and SD to correct the linear chromaticities to zero. The dynamic aperture tracking is used as the judgement to choose the best setting of sextupole strengths. The final integral strength($2b_3\ell$) of the four sextupole families are SD: -13.094 m^{-2}, SF: 14.232 m^{-2}, SD1: -12.07 m^{-2} and SF1: 18.2 m^{-2}.

Unlike the other light source machines where adjusting the global tunes usually means to re-optimize all the parameters for the non-linear effects, PEP-X has the advantage to fully utilize the local phase cancelation within the DBA and TME arcs and then to adjust the phase advances in the 6 straight section through the FODO cells without affecting the local cancelations. The dynamic aperture scan searching of scan of global tunes by adjusting the quadrupole strengths of FODO cells in the long straight sections are shown in Fig. 3.1. The horizontal and vertical beam σ shown in the colormap are defined by 100 pm horizontal beam emittance and 50 pm vertical beam emittance at the injection point where $\beta_x = 200$ m and $\beta_y = 18.4$ m.

However the dynamic aperture tracking using LEGO shows that the horizontal aperture needs to be improved for the aperture requirement for horizontal injection. A tune footprint shows that the horizontal amplitude dependent tune shift is large and causes the shrinkage of the horizontal aperture. A pair of geometric sextupoles SH1, SH2 are placed between the quadrupoles on either side of the ID straights of the DBA supercell where the dispersion is zero to minimize the amplitude dependent tune shift. The study shows these two sextupoles with the same integral strength of -5 m^{-2} will have the best tune shift amplitude optimization. Though these two geometric sextupoles

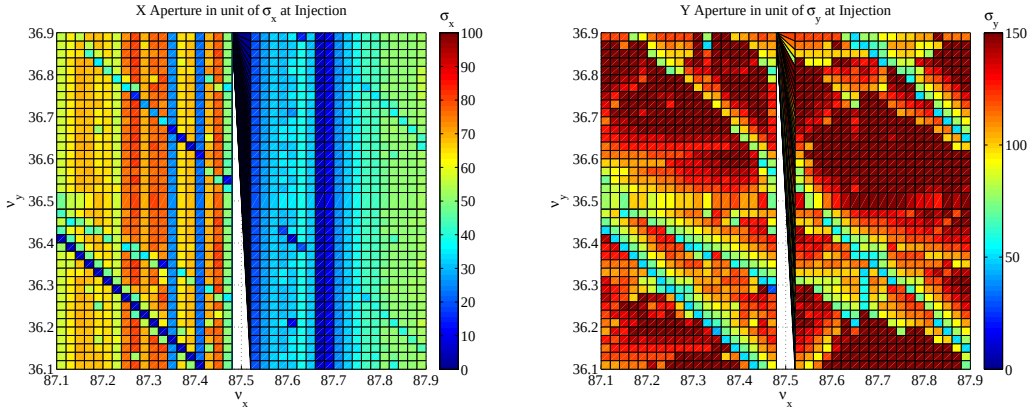

Figure 3.1: Dynamics aperture scan of betatron tunes. Here $\sigma_x = \sqrt{100 \times 10^{-12} * 200} = 0.14$ mm, $\sigma_y = \sqrt{50 \times 10^{-12} * 18.4} = 0.03$ mm.

have the same strengths they will remain separate for future tuning capabilities. The coefficient of leading order amplitude dependent tune shift with and without geometric sextupoles are shown in Table 3.1. Fig. 3.2 shows the tune shift versus the amplitude. The horizontal tune shift versus amplitude is improved significantly at the cost of a slight increment of vertical tune shift with amplitude.

The processes of minimizing the nonlinear effects can be summarized as followings:

- Choose the phase advance of the unit cell to use the repetitive symmetry to combine several identical cells so that the overall first-order transfer matrix is equal to unity (+I) in both transverse planes. In such a system the second-order geometrical (on momentum) aberrations will vanish.

- Finely adjust the phase advance of unit cell of TME and DBA to minimize the higher order nonlinear terms.

- Readjust the combination strengths of sextupoles of SD, SF, SD1, and SF1 while keeping the linear order chromaticities zero.

- Search better global tunes by adjusting the quadrupole strengths in the straight sections to avoid strong resonances with the nonlinear driving terms.

- Add geometric sextupoles and adjust the strengths to minimize the amplitude dependent tune shifts as well as the higher order resonance effects.

Items two to five above can be repeated. Several features are used to help to judge the adjustments in the searching processes, such as: tune shift with momentum deviation as shown in Fig. 2.10, tune shift with amplitude as shown in Fig. 3.2, tune foot print as shown in Fig. 3.5 and chromatic amplitude function shown in Fig. 3.3. Nevertheless, above all, the result of dynamic aperture tracking determines the final setting.

Table 3.1: Coefficient of leading order amplitude dependent tune shift with and without geometric sextupoles SH1, SH2.

	$d\nu_x/d\epsilon_x$	$d\nu_y/d\epsilon_y$	$d\nu_y/d\epsilon_x$
with SH1, SH2	-2.41×10^4	-1.10×10^5	3.02×10^4
without SH1, SH2	-1.39×10^5	-6.94×10^4	2.86×10^4

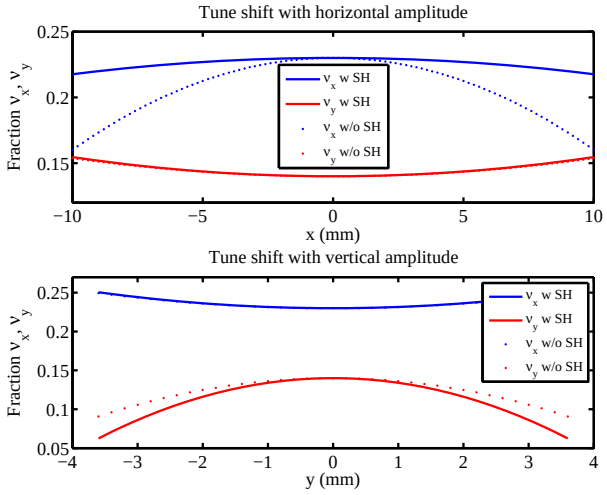

Figure 3.2: Tune shift with amplitude. The solid lines are tune shift with amplitude with geometric sextupole SH1 and SH2. The dots are tune shift with amplitude without geometric sextupole SH1 and SH2.

The final dynamic aperture tracking of the bare lattice at several different energies is shown in Fig. 3.4. The observation point is set at the injection point. Here, and in the following, the bare lattice includes the damping wiggler. The damping wiggler is modeled as pure dipole to provide the necessary damping to achieve the desired small emittance for simulation. The nonlinear effect of the damping wiggler will be discussed in the following section. A 3 σ of 10 nm round beam emittance and $\beta_x = 200$ m, $\beta_y = 18.4$ m

at injection point is shown in Fig. 3.4 as a reference. The horizontal dynamic aperture is sufficient for the horizontal injection if we look at Fig. 2.14.

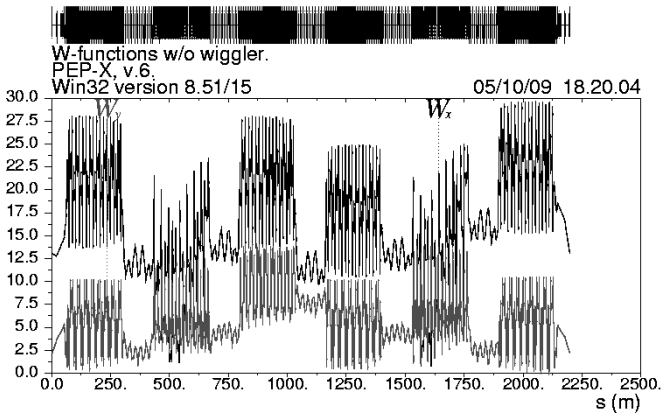

Figure 3.3: Chromatic amplitude function.

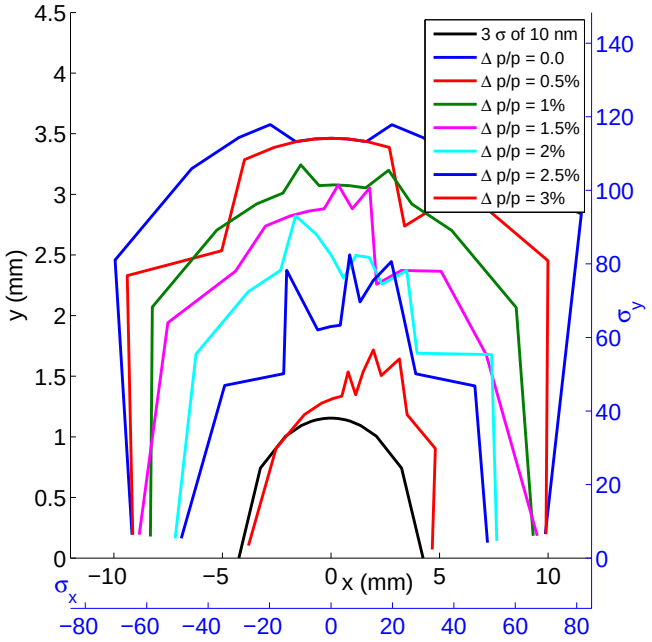

Figure 3.4: Dynamic aperture tracking of the bare lattice at different energy.

3.2 Frequency Map and Phase Space

A frequency map, showing diffusion rate as a function of amplitude or tunes, is an indication of chaotic behavior when the particle motion is close to a

resonance. The diffusion rate is defined by

$$D(\nu_x, \nu_y) = \log_{10}(\sqrt{\Delta(\nu_x)^2 + \Delta(\nu_y)^2}), \tag{3.2}$$

where $\Delta\nu_{x,y}$ is the tune change between the first and second half of the particle tracking with initial amplitude. The frequency map of tune footprint at working tune 87.23, 36.14 with sextupole setting of zero linear chromaticity is shown in Fig. 3.5. The diffusion rate is plotted as a color-weighted value. In the tune footprint several resonance lines can be identified like $\nu_x - 2\nu_y$, $4\nu_x$, $2\nu_x - 3\nu_y$, $2\nu_x + 4\nu_y$, $6\nu_x - 2\nu_y$, $9\nu_x$. Fig. 3.6 shows the frequency map of amplitude dependence of the same beam condition. The horizontal dynamic aperture is limited to 10 mm and the vertical is limited to 3.5 mm.

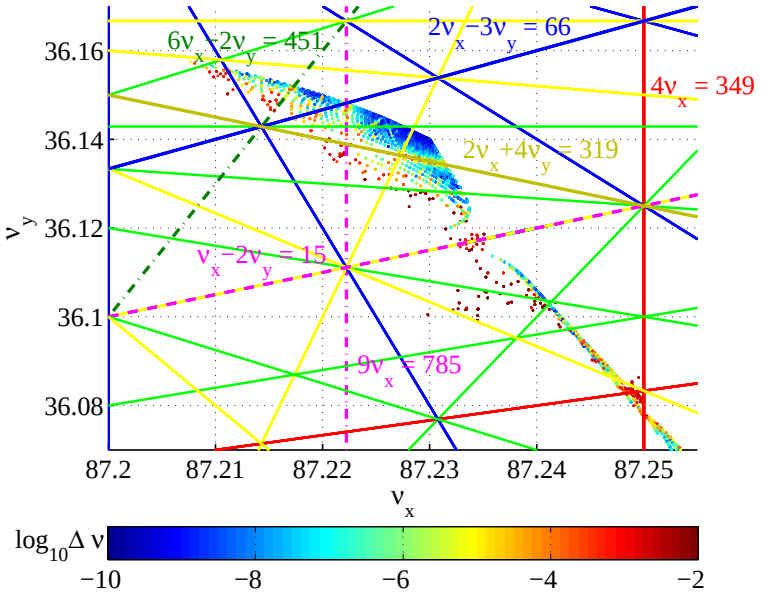

Figure 3.5: Frequency map of tune footprint. The resonance lines are plotted up to sixth order. The resonance lines crossing the footprint which cause tune diffusion are indicated.

Phase space tracking is an alternative way to investigate the particle behavior. Particles with different initial amplitudes are tracked for thousand turns. The turn by turn coordinates are recorded and plotted. As amplitude increased the phase space torus started to be deformed according the order of resonance the particle was approaching. As the particles hit on the separatrix

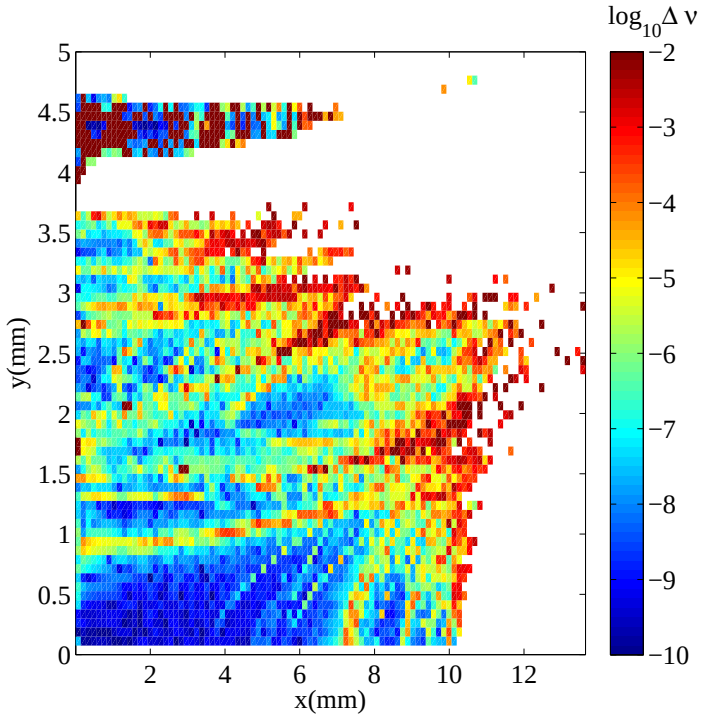

Figure 3.6: Frequency map of amplitude dependent.

the particles started to diffuse and at the end got lost. Fig. 3.7 show the transverse phase space trackings of designed tunes $\nu_x = 87.23$ and $\nu_y = 36.14$ of zero linear chromaticity of on momentum particles. As shown in the figures in the horizontal plane the particle ran into the fifth and the fourth order resonances in the vertical plane.

3.3 Momentum Aperture and Off-Momentum Optics

In a small emittance ring where intra beam scattering(IBS) is severe the momentum aperture becomes one of the dominating factors to determine the beam life time. The momentum aperture is affected by transverse momentum aperture and RF apertures. The transverse momentum aperture $\epsilon_{trans}(s)$ defines as the maximum momentum deviation a particle can get at a Touschek scattering event without being lost on any of the transverse aperture limitation. A particle located in an electron bunch is Touchek scattered to some momentum deviation δ. After this momentum change, the particle

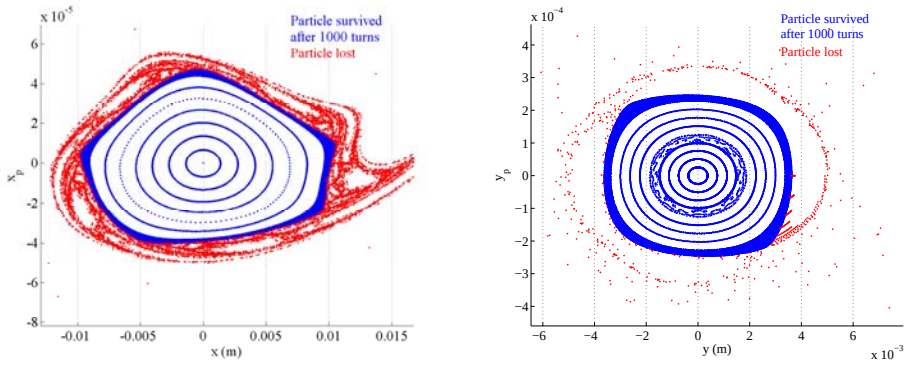

Figure 3.7: Phase space tracking of the horizontal plane (left plot) and the vertical plane (right plot) of on momentum particles. Each torus is constructed by tracking of 1000 turns.

starts an oscillation around a new closed orbit. The oscillation amplitude can be derived as

$$x_{ind}(s,\delta) = \sqrt{\beta_x(s)\mathcal{H}_x(s)}\delta, \tag{3.3}$$

where $\mathcal{H}_x$ is defined by Eq. 2.3. At a given position s the transverse momentum aperture $\epsilon_{trans}(s)$ can be calculated by using

$$\sqrt{\beta_x(s)\mathcal{H}_x(s)}\epsilon_{trans}(s) = \min(x_{phys}(\epsilon_{trans},s), x_{dyn}(\epsilon_{trans},s)), \tag{3.4}$$

The x_{dyn} is dynamic aperture tracked with respect to the closed orbit of the off-momentum δ. In the PEP-X design, the horizontal physical aperture is larger than the dynamic aperture. Therefore the transverse momentum aperture is determined solely by the dynamic aperture. Fig. 3.8 shows the tracking result of off momentum acceptance from LEGO. Fig. 3.11 shows the transverse momentum aperture according to Eq.(3.4). Due to the nonlinear effects, the β_x, β_y and η are energy dependent. The optics functions as function of momentum δ at the injection point are presented in Fig. 3.9. The transverse momentum taking into consideration nonlinear optics due to off momentum is also shown in Fig. 3.11 .

The calculation of RF momentum aperture is related to be the momentum compaction factor. The first order momentum compaction α_1 of PEP-X is 5.81×10^{-5}, which is small. The second order momentum compaction α_2 is 2.78×10^{-4}. The longitudinal Hamiltonian including the α_2 term is

$$H(\phi,\delta) = \omega_{rf}(\alpha_1\frac{\delta^2}{2} + \alpha_2\frac{\delta^3}{3}) + \frac{eV_{rf}}{E_0T_0}[(\cos\phi - \cos\phi_s) + (\phi-\phi_s)\sin\phi_s], \tag{3.5}$$

with a non zero value of α_2 there exist now two stable fix points and two

unstable fix points. The stable fixed points are $(\phi = \phi_s, \delta = 0)$ and $(\phi = \pi - \phi_s, \delta = -\frac{\alpha_1}{\alpha_2})$. The unstable fixed points are $(\phi = \pi - \phi_s, \delta = 0)$ and $(\phi = \phi_s, \delta = -\frac{\alpha_1}{\alpha_2})$. The RF bucket acceptance is deformed compared to the linear case. The deformation depends on the ratio $\frac{\alpha_1}{\alpha_2}$. The longitudinal phase space includes the nonlinear term α_2 is shown in Fig. 3.10. Because $\frac{\alpha_1}{\alpha_2} = 0.21$ is larger than the linear RF bucket momentum acceptance which is 5.6 % at RF gap voltage of 8.9 MV, the deformation of RF energy acceptance is negligible. It's proper that we take the linear RF bucket momentum 5.6 % as the over all RF momentum acceptance, which is larger than the transverse momentum aperture along the whole ring. Therefore the momentum aperture of PEP-X is determined by the transverse momentum aperture due to the dynamic aperture as shown in Fig. 3.11.

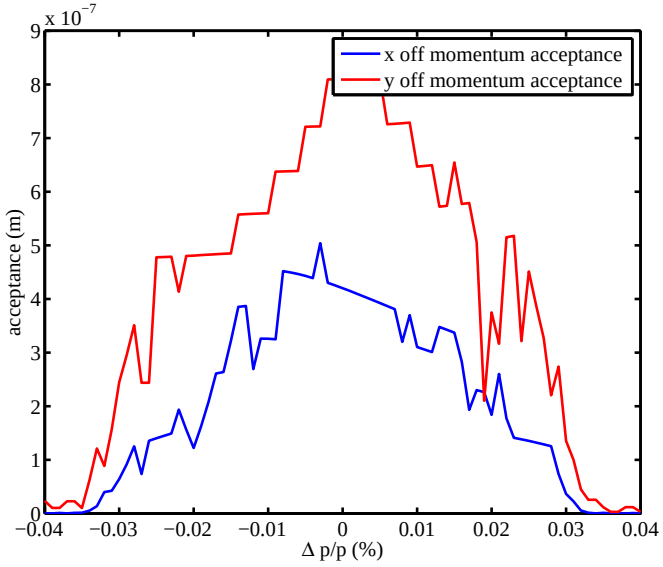

Figure 3.8: Off momentum acceptance of PEP-X.

3.4 Multipole Errors

Systematic and random magnetic field errors will reduce the dynamic aperture further. Their impacts need to be evaluated. Because PEP-X will inherit as many magnets as applicable from the PEP-II HER ring, the tolerances of magnet multipole errors achieved at the PEP II HER are used to simulate the effect of dynamic aperture. The systematic and random magnetic multipole tolerance is shown in Table 3.2. The field errors are defined relative to the main field component $B_m(r)$ normalized at a reference radius r,

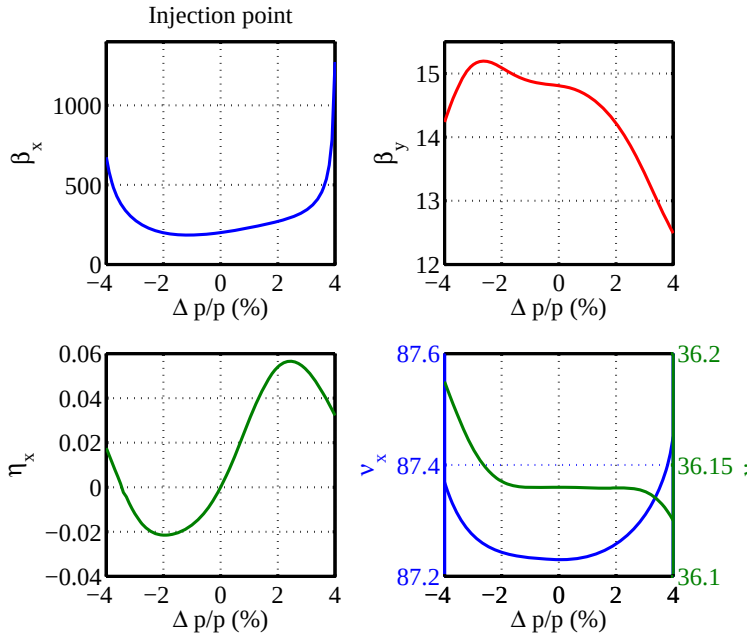

Figure 3.9: Optics functions at the injection point as function of off momentum δ.

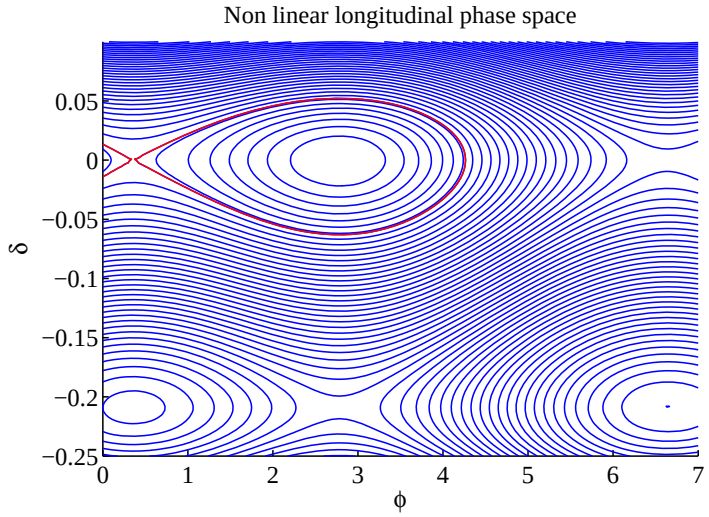

Figure 3.10: Nonlinear longitudinal phase space. The red curve is the separatrix.

$$\frac{B_y + iB_x}{B_m(r)} = \sum_{n=1} (b_n + ia_n)(\frac{x}{r} + i\frac{y}{r})^{n-1}, \tag{3.6}$$

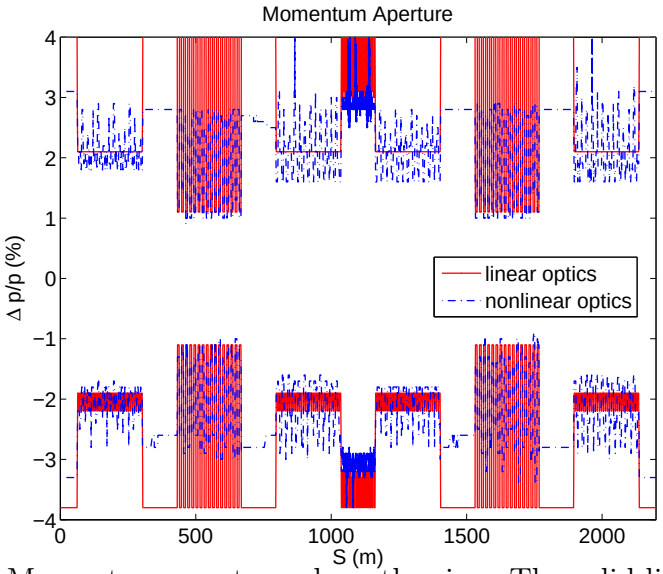

Figure 3.11: Momentum aperture along the ring. The solid line is the transverse momentum aperture of linear optics in Eq.(3.4). The dashed line is the transverse momentum aperture taking into consideration nonlinear optics due to off momentum. Because the RF momentum of 5.6 % is larger than the transverse momentum. The transverse momentum aperture shows here is also the momentum aperture of PEP-X.

where $m = 1$ represents dipole, $m = 2$ represents quadrupole and so on.

For random magnetic errors, ten random seeds are used to simulate the effect for verification of the validity of the tolerance. The dynamic aperture tracking result with systematic and ten seeds of random magnet errors with damping wigglers without multipole field errors of damping wigglers is shown in Fig. 3.12. The nonlinear effect of the damping wiggler with and without mulitpole field errors will be discussed in next section. Comparing to the simulation result of bare lattice in Fig. 3.4 the deduction of dynamic aperture is tolerable.

3.5 Dynamic Effects of the Damping Wigglers

A damping wiggler is a nonlinear device that can potentially reduce the dynamic aperture of a storage ring. For an ideal damping wiggler the first and second field integrals are zeros. Therefore there is no static kick or position change to the electrons. However, electron motion is still affected by the wiggler as a consequence of the sinusoidal trajectories of the electrons and the transverse variation of the magnetic fields inside the wiggler. If

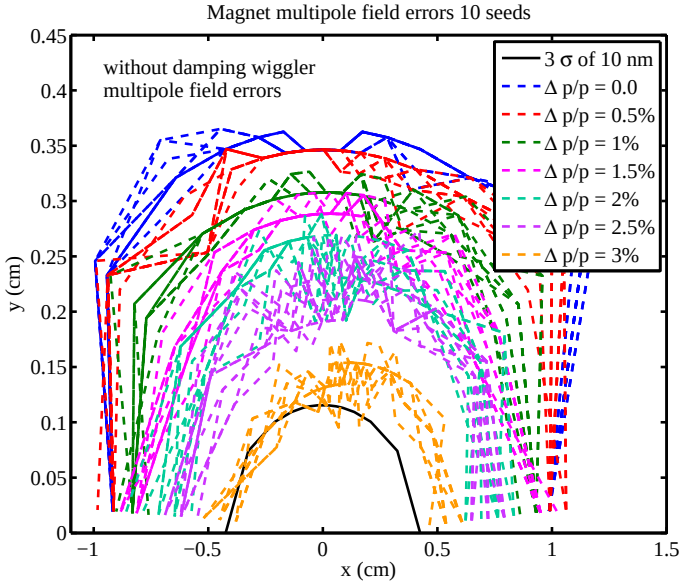

Figure 3.12: Dynamic aperture tracking of systematic and random magnet errors with ten seeds.

Table 3.2: Measured magnetic multipole errors in the magnets of the High Energy Ring of PEP-II.

Multipole errors of dipole at radius $r = 30$ mm				
type	b_3	b_4	b_5	b_6
systematic	1.0×10^{-5}			
rms	3.2×10^{-5}	3.2×10^{-5}	6.4×10^{-5}	8.2×10^{-5}
Multipole errors of quadrupole at radius $r = 44.9$ mm				
type	b_3	b_4	b_5	b_6
systematic	1.03×10^{-3}	5.6×10^{-4}	4.8×10^{-4}	2.37×10^{-3}
rms	5.6×10^{-4}	4.5×10^{-4}	1.9×10^{-4}	
type	b_{10}	b_{14}		
systematic	-3.1×10^{-3}	-2.63×10^{-3}		
rms	1.8×10^{-4}	7.0×10^{-5}		
Multipole errors of sextupole at radius $r = 56.52$ mm				
type	b_5	b_7	b_9	b_{15}
systematic			-1.45×10^{-2}	-1.3×10^{-2}
rms	2.2×10^{-3}	1.05×10^{-3}		

we assume the pole width is sufficiently large and there is no pole shaping, the horizontal variation of the vertical magnetic field can be neglected. The dynamic effect is then primarily in the vertical plane, which can be described

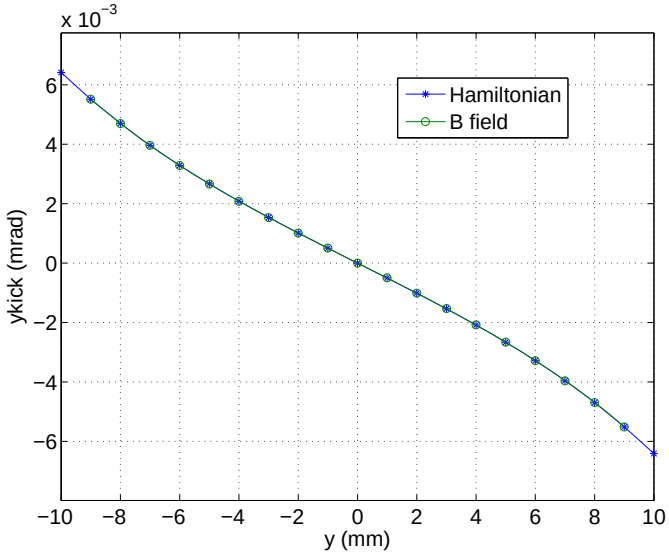

Figure 3.13: Kick received by electrons from one period of the damping wiggler

by a Hamiltonian [7]

$$H_y = \frac{1}{2}p_y^2 + \frac{1}{4\rho^2}y^2 + \frac{k^2}{12\rho^2}y^4 + \frac{k^4}{90\rho^2}y^6, \tag{3.7}$$

where $k = \frac{2\pi}{\lambda_w}$, λ_w is the wiggler period and $\rho = \frac{B\rho}{B_0}$is the minimum bending radius. Higher order terms and coupling terms are neglected in Eq.(3.7).

This effect can be modeled in a tracking code through a tracking table approach [8]. The tracking table is a map of the incoming position coordinates of the electrons to the transverse kicks they receive as they pass the wiggler, which can be built by solving Eq.(3.7) or directly integrating the Lorentz equation with known magnetic field distribution in the wiggler. The wiggler is split into several slices, each slice represented by a drift-kick-drift section.

The PEP-X damping wiggler period is $\lambda_w = 0.1$ m and the peak magnetic field is $B_0 = 1.5$ T. There are a total of 18 identical wiggler sections. Each wiggler section has 50 periods. The vertical kick received from one period of the wiggler is shown in Fig. 3.13, calculated with the two methods suggested above. A tracking table is built for each wiggler section with 50 times stronger kicks than shown in the figure. The impact of the damping wigglers to the dynamic aperture of the ring is studied with the tracking code AT [9]. The MAD model for the PEP-X lattice is converted to AT. The thin wiggler poles for each wiggler section are replaced by one tracking table. This causes only

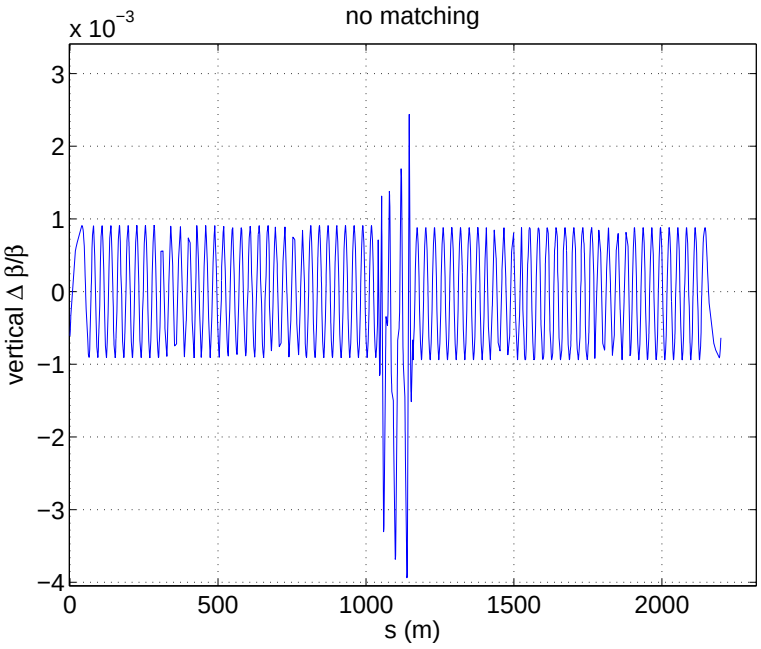

Figure 3.14: Vertical beta beating introduced by replacing thin poles with tracking tables.

very small optics distortion since the vertical focusing from the tracking table is basically the same as the edge focusing effect of the thin poles. The vertical beta beating is shown in Fig 3.14. Dynamic aperture is obtained by starting particles on a transverse grid with initial $x' = 0, y' = 0$, and tracking 1000 turns. Radiation damping and the rf cavity are turned on in this simulation. A comparison of the dynamic aperture for the PEP-X ideal lattice, with or without damping wigglers is shown Fig 3.15. For both the on-energy case and the case with 2% energy error, no large difference is seen.

To study the damping wiggler effect in a more realistic scenario we put linear and nonlinear random errors into the model. Quadrupole and skew quadrupole errors are inserted into the sextupole elements to introduce linear optics error and linear coupling. Systematic and random multipole errors are put into bend magnets, quadrupoles and sextupoles. For both the cases with or without damping wigglers we built 10 random models. Their rms beta beating ranges from 0.5% to 2% and the linear coupling ratio (ratio of vertical emittance to horizontal emittance) is fixed at 1%. The systematic multipole errors are identical to those in Table 3.2. The random multipole errors are similar to what is listed in Table 3.2.

The dynamic apertures for the two cases (with and without damping wigglers) are shown in Fig 3.16. The thick curves represent the average dynamic aperture of the 10 seeds while the thin curves around them represent

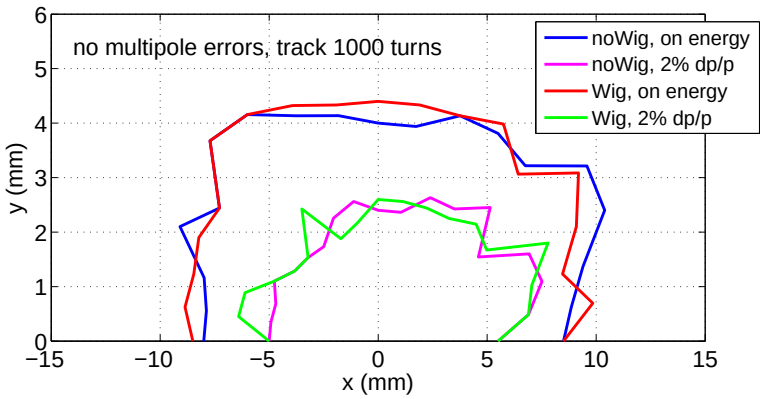

Figure 3.15: On and off-energy dynamic aperture for PEP-X ideal lattice, with or without damping wigglers.

the worst and best values among the 10 seeds.

Comparison of the two cases in Fig 3.16 leads us to conclude that the damping wigglers don't cause a large reduction of dynamic aperture in the PEP-X lattice.

3.6 Alignment and Field Error and Correction Schemes

Quadrupole displacement, dipole field error and dipole rotation are the sources of errors that affect a closed orbit. The closed orbit is generated according to the closed orbit formula

$$\Delta x, y_{co} = \frac{\sqrt{\beta_{x,y}}}{2\sqrt{2}\sin(\pi\nu_{x,y})}\sum_i \Delta\Theta_{(x,y),i}\sqrt{\beta_{(x,y),i}}, \tag{3.8}$$

where $\Delta\Theta$ is the effective kick due to different error source. For dipole field error $\Delta\Theta_x = \frac{\Delta B_1}{B_1}\theta_{bend}$, for dipole rotation $\Delta\Theta_y = \Delta\phi_{rot}\theta_{bend}$ and for quadrupole displacement $\Delta\Theta_{x,y} = \Delta x, y k_1 l_{quad}$. where θ_{bend} is the bending angle of the dipole, ϕ_{rot} is the rotation angle of dipole, $k_1 = \frac{B_2'}{B_1\rho}$. For a random distribution of errors the generated RMS orbit distortions are given by

$$\Delta x, y_{co}^{rms} = \frac{\sqrt{\beta_{x,y}}}{2\sqrt{2}\sin(\pi\nu_{x,y})}\{\sum_i \Delta\Theta^2_{(x,y),i}\beta_{(x,y),i}\}^{1/2}. \tag{3.9}$$

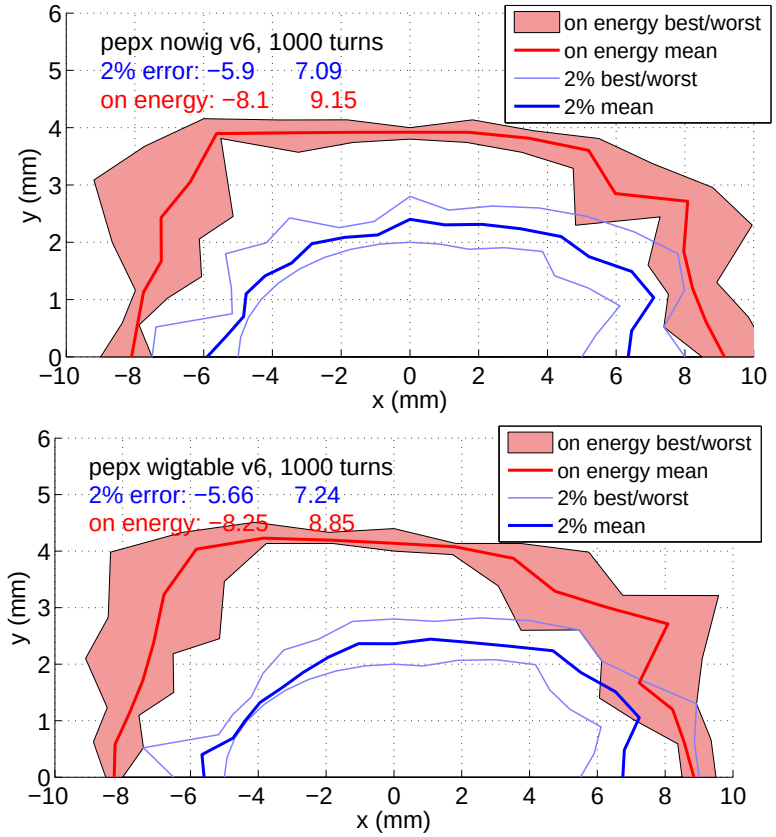

Figure 3.16: On and off-energy dynamic aperture with linear and nonlinear errors. Top: without damping wigglers; bottom: with damping wigglers.

Amplification factors of different error sources can be defined as

$$A_{x,y}^{bend} = \frac{\Delta x, y_{co}^{rms}}{(\frac{\Delta B_1}{B_1})^{rms}, \Delta\phi_{rot}^{rms}} = \frac{\sqrt{\beta_{x,y}}}{2\sqrt{2}\sin(\pi\nu_{x,y})}\{\sum_i \theta_i^2\beta_{(x,y),i}\}^{1/2},$$

$$A_{x,y}^{quad} = \frac{\Delta x, y_{co}^{rms}}{\Delta x, y^{rms}} = \frac{\sqrt{\beta_{x,y}}}{2\sqrt{2}\sin(\pi\nu_{x,y})}\sum_i (k_1 l_{quad})^2\beta_{(x,y),i}\}^{1/2}. \quad (3.10)$$

Fig. 3.17 shows the bending magnet amplification factors of the ring for the reference design tunes. Fig. 3.18 shows the quadrupole amplification factors through the ring. The requirement of transverse alignment tolerances and field errors are summarized in Table 3.3 which is cited from NSLSII conceptual design report [10] at this moment.

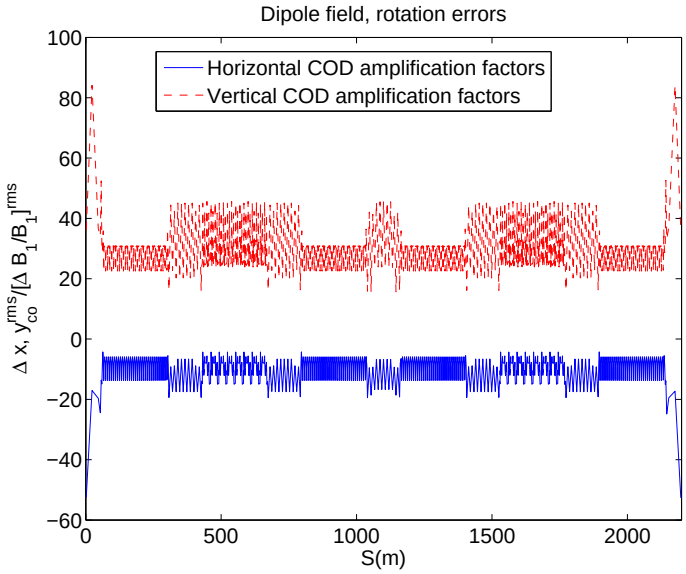

Figure 3.17: Dipole amplification factor.

Table 3.3: RMS values of transverse alignment tolerances and field errors.

	$\Delta x(\mu\text{m})$	Δy (μm)	Roll (m-rad)	$\frac{\Delta B_N}{B_N}$
Dipole	100	100	0.5	1×10^{-4}
Quadrupole	30	30	0.2	5×10^{-4}
Sextupole	30	30	0.2	5×10^{-4}

The orbit errors need to be corrected. The basic concept is to steer the

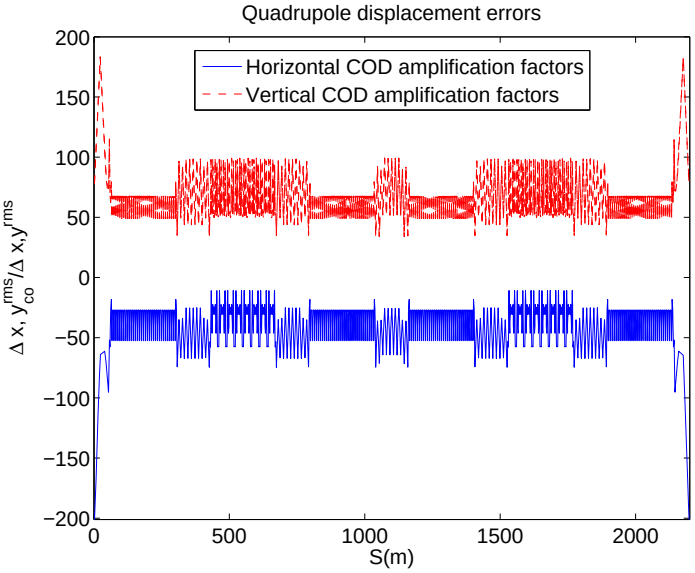

Figure 3.18: Quadrupole amplification factor.

orbit through the center of sextupole magnets. In theory, the dynamic aperture can be restored if the beam orbit is at the sextupole magnetic center. As a rough guideline, the BPMs should be spaced by 90^0 in phase advance and placed close to the sextupoles. In the TME cell the BPMs are put after every sextupole and a pair of horizontal and vertical correctors are put in between focussing and defocussing quadrupoles as shown in Fig. 3.19. In the straight FODO cell, horizontal correctors are put in after a focussing quadrupole and vertical correctors are put in after a defocussing quadrupole; every corrector is preceded by a BPM. In the super cell (two DBAs) the correctors and BPMs are shown in Fig. 3.20. There are a total of 434 horizontal correctors, 434 vertical correctors and 694 double view BPMs.

We first study the case with only quadrupole alignment errors plus the multipole and field error. Ten random seeds of errors were generated in LEGO. The alignment error of a magnet is treated individually relative to the designed orbit in this study. The procedure is first to try to find the closed orbit in the presence of alignment errors and field errors and then apply orbit correction to correct the orbit. We have used the method of SVD to correct the orbit. After the orbit correction, the systematic and random multipole errors are added, followed by coupling, tune and chromaticity correction. After correction of beta beat and dispersion, the orbit, coupling, tune and chromaticity corrections are repeated for several iterations before the on momentum dynamic aperture is tracked. The result is shown in Fig. 3.21. Note that 5 out of 10 random seeds can have solutions of closed

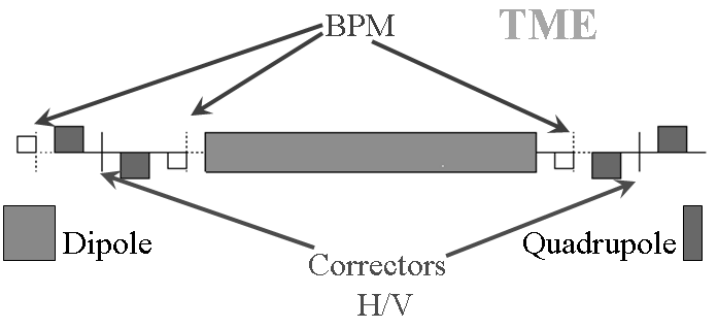

Figure 3.19: Correctors and BPMs in a TME cell.

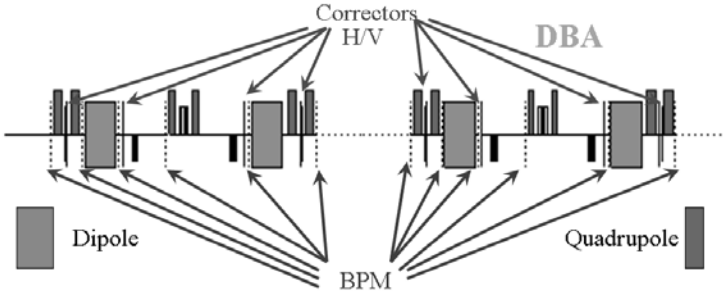

Figure 3.20: Correctors and BPMs in a super cell (two DBAS).

orbits. The residual orbits are shown in Fig. 3.22. The same procedures are applied to track the dynamic aperture including all errors in Table 3.2 and Table 3.3. The dynamic aperture of 4 random seeds out of 10 is shown in Fig. 3.23. The residual orbits are shown in Fig. 3.24. In the case with all errors, the vertical aperture deteriorates, showing large aperture deduction in some random error sets. The change of horizontal dynamic aperture is less severe which is good in sustaining the aperture for horizontal injection. We will need to try to find a better correction scheme to steer the orbit to reduce nonlinearity caused by the orbit. Now the residual orbit is at the hundred μm order which we believe can be further reduced.

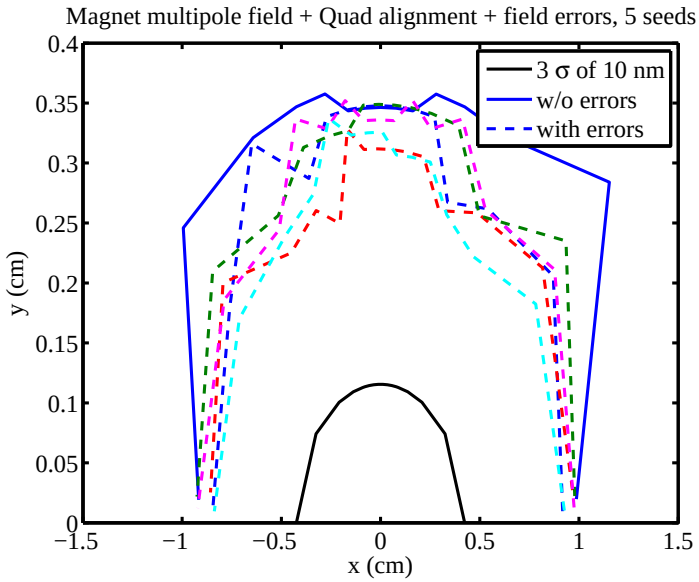

Figure 3.21: Dynamic aperture of PEP-X with quadrupole alignment errors, field errors and multipole errors after correction. The solid line is the aperture of bare lattice.

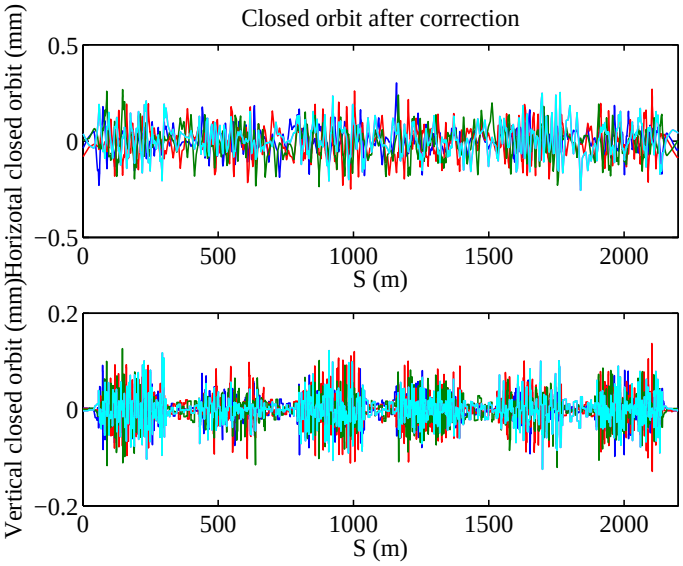

Figure 3.22: Residual orbit after orbit correction of quadrupole alignment errors and field errors.

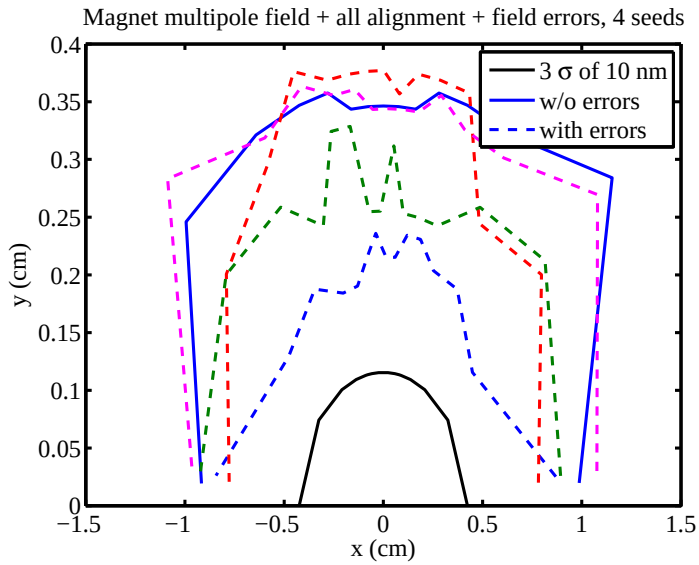

Figure 3.23: Dynamic aperture of PEP-X with errors specified in Table 3.2 and Table 3.3 after correction. The solid line is the aperture of bare lattice.

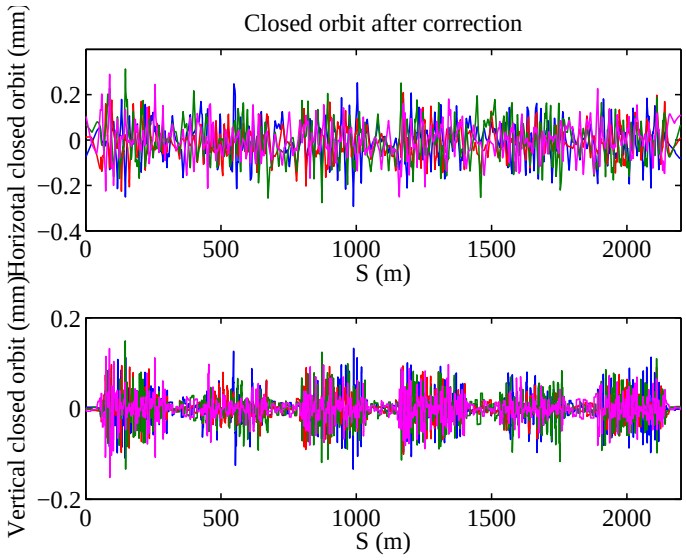

Figure 3.24: Residual orbit after orbit correction of all errors.

Chapter 4

Intra-Beam Scattering and Touschek Lifetime

Intra-beam scattering (IBS) describes multiple Coulomb scattering that in electron machines leads to an increase in all bunch dimensions and in energy spread, whereas the Touschek effect concerns large single Coulomb scattering events where energy transfer from transverse to longitudinal leads to immediate particle loss. In low emittance machines, such as PEP-X, both effects tend to be important.

4.1 Intra-Beam Scattering

For PEP-X IBS calculations we employ the Bjorken-Mtingwa (B-M) formulation [11], using the Nagaitsev [12] algorithm for efficient calculation. We assume that we are coupling dominated, by which we imply that the vertical dispersion can be kept sufficiently small. Then the vertical emittance is proportional to the horizontal emittance,

$$\epsilon_y = \kappa \epsilon_x \ , \tag{4.1}$$

with κ the coupling constant. The nominal (no IBS) horizontal and vertical emittances are given by $\epsilon_{x0} = \epsilon_{x00}/(1+\kappa)$ and $\epsilon_{y0} = \kappa\epsilon_{x00}/(1+\kappa)$, where ϵ_{x00} is a property of the lattice. IBS calculations of the steady-state horizontal emittance ϵ_x and (relative) energy spread σ_p are performed by simultaneously solving

$$\epsilon_x = \frac{\epsilon_{x0}}{1-\tau_x/T_x} \qquad \text{and} \qquad \sigma_p^2 = \frac{\sigma_{p0}^2}{1-\tau_p/T_p} \ , \tag{4.2}$$

where τ_x, τ_p, signify the radiation damping times, $1/T_x$, $1/T_p$, the IBS growth rates, and σ_{p0} the nominal rms energy spread.

B-M gives the local growth rates $\delta(1/T_x)$, $\delta(1/T_p)$, in terms of beam properties and local lattice properties. These rates are calculated for all positions around the ring and then averaged ($\langle\rangle$ means to average around the ring) to give $\langle\delta(1/T_x)\rangle = 1/T_x$, $\langle\delta(1/T_p)\rangle = 1/T_p$, and then Eqs. 4.2 are solved simultaneously. Note that since the growth rates also depend on the beam emittances, energy spread, and bunch length Eqs. 4.2 need to be solved by iteration.

A simplified model of the B-M equations that can be used (with slight modification) to approximate the results for PEP-X is the so-called "high energy approximation" [13]. We present it here since it may more clearly show the parameter dependence of IBS than the B-M equations, though to obtain the numerical results for PEP-X (given below) we will use the more accurate B-M equations. According to this simplified model the IBS growth rate in energy spread is given by

$$\frac{1}{T_p} \approx \frac{r_e^2 c N_b (\log)}{16\gamma^3 \epsilon_x^{3/4} \epsilon_y^{3/4} \sigma_z \sigma_p^3} \left\langle \sigma_H \, g(a/b) \, (\beta_x \beta_y)^{-1/4} \right\rangle \ . \tag{4.3}$$

Here r_e is the radius of the electron, c the speed of light, N_b the number of electrons per bunch, (log) the Coulomb log factor, γ the Lorentz energy factor, σ_z the bunch length, and β_x, β_y, the optical beta functions. Other factors in Eq. 4.3 are defined by

$$\frac{1}{\sigma_H^2} = \frac{1}{\sigma_p^2} + \frac{\mathcal{H}_x}{\epsilon_x} \ , \quad a = \frac{\sigma_H}{\gamma}\sqrt{\frac{\beta_x}{\epsilon_x}} \ , \quad b = \frac{\sigma_H}{\gamma}\sqrt{\frac{\beta_y}{\epsilon_y}} \ , \tag{4.4}$$

$$g(\alpha) = \alpha^{(0.021 - 0.044 \ln \alpha)} \ , \tag{4.5}$$

where $\mathcal{H}$ is the so-called "curly H" dispersion function (see Eq. 2.3). Finally, the horizontal IBS growth rate is given by

$$\frac{1}{T_x} = \frac{\sigma_p^2}{\epsilon_x} \langle \mathcal{H}_x \delta(1/T_p) \rangle \quad . \tag{4.6}$$

Note that Eq. 4.6 is slightly different than the corresponding equation given in Ref. [13], where it reads

$$\frac{1}{T_x} = \frac{\sigma_p^2}{\epsilon_x} \langle \mathcal{H}_x \rangle \frac{1}{T_p} \quad ; \tag{4.7}$$

that version was derived from the present version assuming no correlations

between $\mathcal{H}_x$ and $\delta(1/T_p)$.* The PEP-X lattice, however, has such correlations; for it we find reasonable agreement for the current version of the equation, while the earlier version is typically off by a factor of 2. Finally, note that the high energy IBS approximation given here has validity when a, $b \ll 1$, which for PEP-X parameters holds.

In scattering calculations, like IBS, a Coulomb log term is used to take into account the contribution of very large and very small impact parameter events. Due to the very small impact parameter events the tails of the steady-state bunch distributions are not Gaussian and the standard way of computing (log) overemphasizes their importance. To better describe the size of the core of the bunch we calculate the Coulomb log factor as first proposed by Raubenheimer [14, 15]. For PEP-X, (log) ≈ 13.

A note on the averaging the IBS effect around the ring: An important ingredient for the calculation is the Twiss parameters for the PEP-X lattice. For our lattice we have, from the optics program MAD, the Twiss parameters at the end of every object, with the exception that the bends are split into two equal pieces, with each piece becoming an element. The averaging is performed by rectangular rule quadrature, which in principle can lead to errors. However, spot checks performed by splitting the bends into several pieces produced no significant difference in result.

For our IBS calculations nominal parameters are obtained from Table I, and the lattice used is that described earlier. We assume that potential well bunch lengthening is not significant and that the nominal current is below the threshold to the microwave instability. We consider two modes of operation: (1) where the coupling factor κ is adjusted so that the vertical emittance is diffraction limited at 1 Å, *i.e.* $\epsilon_y = 8$ pm; this is the more normal mode of operation where PEP-X is a synchrotron light source, and (2) where we choose a round beam ($\kappa = 1$), for running an FEL in one of the straight sections. The results of our IBS calculations for the two configurations are shown in Table II, where we give steady-state values of horizontal and vertical emittance, ϵ_x and ϵ_y, energy spread σ_p and bunch length σ_z. We note that for PEP-X, IBS has little effect on σ_p and σ_z. At the normal mode of operation ϵ_x doubles from the nominal case, whereas in the round beam mode it grows by 60%.

In the nominal (low emittance) configuration the horizontal IBS growth rate is $T_x^{-1} = 24.7\ \mathrm{s}^{-1}$ (and the energy growth rate $T_p^{-1} = 9.5\ \mathrm{s}^{-1}$). Note that from the high energy approximation, Eqs. 4.3, 4.6, we obtain $T_p^{-1} = 12.0\ \mathrm{s}^{-1}$ and $T_x^{-1} = 22.9\ \mathrm{s}^{-1}$ (whereas Eq. 4.7 yields $T_x^{-1} = 43.3\ \mathrm{s}^{-1}$). The accumulation around the ring of the horizontal growth rate is shown in Fig. 4.1. We note that, as expected, the growth rate is significant only in regions where there are bends (where $\mathcal{H}_x$ is non-zero): 65% of the total growth occurs in

*Eq. 4.7 was well-known before Ref. [13] and in fact can be found in B-M's report.

Table 4.1: Nominal parameters for PEP-X used in this report. Note that the nominal horizontal emittance $\epsilon_{x0} = \epsilon_{x00}/(1+\kappa)$, with κ the x–y coupling parameter.

Parameter	Value	Units
Energy, E	4.5	GeV
Circumference, C	2199.	m
Average current, I	1.5	A
Bunch population, N_b	2.18	10^{10}
Number of bunches, M	3154	
Relative rms energy spread, σ_{p0}	1.14	10^{-3}
Rms bunch length, σ_{z0}	3.0	mm
Horiz. emittance parameter, ϵ_{x00}	85.7	pm
Horiz. radiation damping time, τ_x	13.5	ms
Long. radiation damping time, τ_p	7.2	ms

Table 4.2: For flat and round-beam cases at the nominal current $I = 1.5$ A: x-y coupling parameter κ and nominal (zero-current) horizontal emittance ϵ_{x0}; steady-state horizontal ϵ_x and vertical ϵ_y emittances, relative energy spread σ_p, and bunch length σ_z; and Touschek lifetime $\mathcal{T}$. Note that $\epsilon_{x0} = \epsilon_{x00}/(1+\kappa)$ with $\epsilon_{x00} = 86$ pm.

κ	ϵ_{x0} [pm]	ϵ_x [pm]	ϵ_y [pm]	σ_p [10^{-3}]	σ_z [mm]	$\mathcal{T}$ [min]
.049	82.	164.	8.0	1.20	3.16	29.
1.	43.	69.	69.	1.17	3.08	92.

the TME arcs and 35% in the DBA arcs.

The dependencies of the steady-state emittances ϵ_x, ϵ_y, as functions of beam current I are shown in Figs. 4.2 and 4.3 (the solid curves). Results are given for $\kappa = .05, .15, .40, 1$. Note that when plotting the results as $(\epsilon_x/\epsilon_{x0})$ *vs.* I the curves for $\kappa = .15, .40$, and 1 are almost the same, varying by less than 5% for $I \leq 3$ A.

We have observed that for PEP-X the growth of longitudinal emittance due to IBS is very small. This means that, to good approximation, σ_p and σ_z can be taken to have their nominal values and one need only solve the first of Eqs. 4.2. In this case the horizontal emittance as a function of peak current can be approximated by a solution (the maximum, real solution) of the equation

$$\left(\frac{\epsilon_x}{\epsilon_{x0}}\right)^{5/2} - \left(\frac{\epsilon_x}{\epsilon_{x0}}\right)^{3/2} = \alpha\left(\frac{I}{I_A}\right) \quad , \tag{4.8}$$

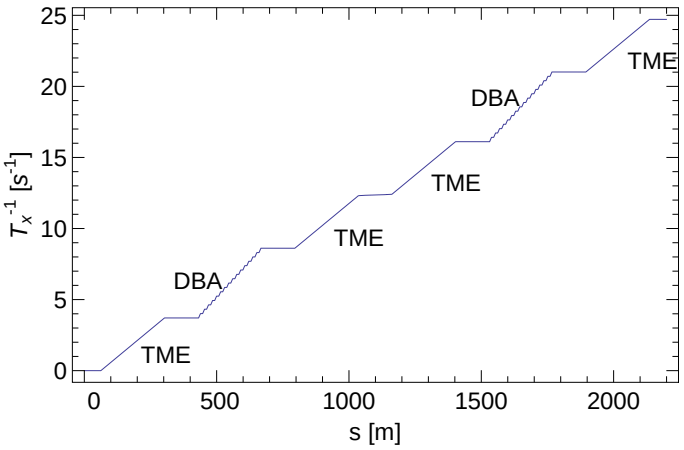

Figure 4.1: Accumulation around the ring of the IBS growth rate in x. The positions where the slope of the curve is nonzero are the TME and DBA arcs.

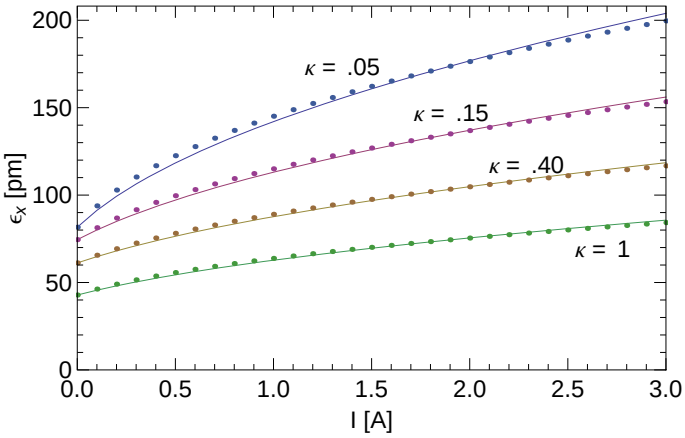

Figure 4.2: Steady-state horizontal emittance as a function of bunch current in PEP-X for $\kappa = 0.05$, 0.15, 0.40, and 1. The dotted curves give the simple 1D approximation, described by Eq. 4.8.

with α a constant obtained by fitting and $I_A = 17$ kA the Alvén current. The vertical emittance follows the same equation, but with $(\epsilon_x/\epsilon_{x0})$ replaced by $(\epsilon_y/\epsilon_{y0})$. To approximately reproduce the curves of Figs. 4.2 and 4.3 from this equation, the constant is taken to be $\alpha = 3570.(1+\kappa)^{2.08}\kappa^{-.69}$ (see Fig. 4.2 and 4.3, the dots).

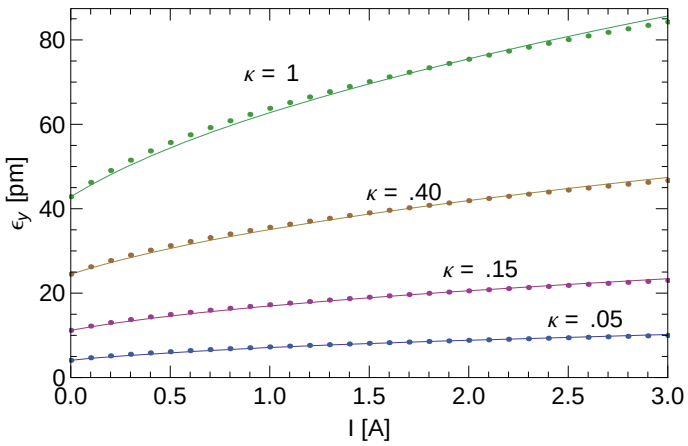

Figure 4.3: Steady-state vertical emittance as a function of bunch current in PEP-X for $\kappa = 0.05$, 0.15, 0.40, and 1. The dotted curves give the simple 1D approximation, described by Eq. 4.8.

4.2 Touschek Lifetime

The Touschek lifetime calculations follow the method of Brück [16], with modifications by Piwinski [17]. With the Touschek effect the number of particles in a bunch decays with time t as

$$N_b = \frac{N_{b0}}{1 + t/\mathcal{T}} \ , \tag{4.9}$$

with N_{b0} the initial bunch population, and $\mathcal{T}$ the Touschek lifetime. Note that the decay is not exponential. The lifetime is given (in the coupling dominated case, assuming no y dispersion) by [17]

$$\frac{1}{\mathcal{T}} = \frac{r_e^2 c N_b}{8\pi\beta^3\gamma^5\sigma_z\kappa^{1/2}\epsilon_x^2} \left\langle \frac{\beta_x^{3/2}\sigma_x^2}{\beta_y^{1/2}\tilde{\sigma}_x^3} \frac{\mathcal{C}(\epsilon_m)}{\epsilon_m} \right\rangle \ , \tag{4.10}$$

with

$$\mathcal{C}(\epsilon_m) = -\frac{3}{2} e^{-\epsilon_m} + \int_{\epsilon_m}^{\infty} \left(1 + \frac{3\epsilon_m}{2} + \frac{\epsilon_m}{2} \ln \frac{u}{\epsilon_m} \right) e^{-u} \frac{du}{u} \ , \tag{4.11}$$

$$\epsilon_m = \frac{\beta_x \sigma_x^2 \delta_m}{\gamma^2 \epsilon_x \tilde{\sigma}_x^2} \ . \tag{4.12}$$

Parameters are average velocity over the speed of light β, relative momentum acceptance δ_m, and beam sizes $\sigma_x = \sqrt{\beta_x \epsilon_x + \eta_x^2 \sigma_p^2}$ and $\tilde{\sigma}_x = \sqrt{\beta_x \epsilon_x + \beta_x \mathcal{H}_x \sigma_p^2}$.

Brück's formula is valid for flat beams ($\epsilon_x/\beta_x \gg \epsilon_y/\beta_y$) and for non-relativistic energies in the beam rest frame ($\gamma^2 \sigma_x^2/\beta_x^2 \ll 1$). For PEP-X these conditions hold well for the nominal, flat beam case but not for the round ($\kappa = 1$) case. Nevertheless, for the time being we assume that, even in the round case, the calculation gives us a rough approximation of the effect.

The Touschek lifetime depends on the momentum aperture in the ring, and thus we have calculated the momentum aperture due to first order optics as a function of location in PEP-X (see Fig. 4.4): In tracking, at a given position s a beam particle is given a relative (positive) momentum kick δ_m, and it undergoes betatron oscillation. The largest value of δ_m for which the particle survives defines the positive momentum aperture at position s. Then the same is done for a negative momentum kick. From the plot we see that the typical value of momentum aperture for PEP-X is $\delta_m \sim \pm 2\%$.

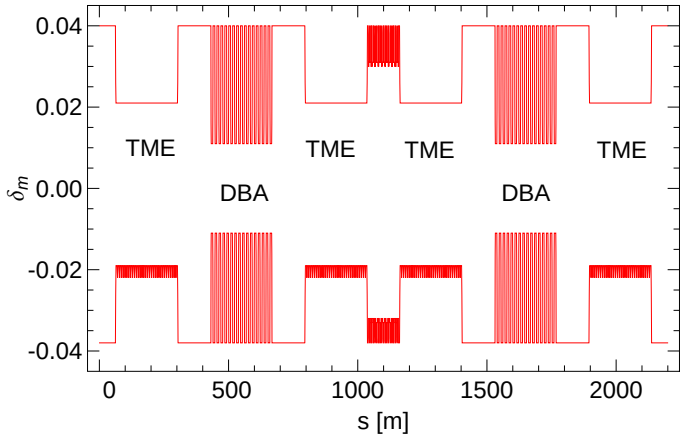

Figure 4.4: The momentum acceptance due to the linear optics, δ_m, for PEP-X. This function is used in finding the Touschek lifetime. The locations of the TME and DBA arcs are also indicated in the figure.

Using the δ_m as shown in Fig. 4.4, Touschek lifetimes were calculated for the nominal and round-beam cases in PEP-X (see the last column of Table 4.2). Note that these calculations are based on the IBS determined, steady-state beam sizes (otherwise the results would be much smaller). In the nominal, diffraction limited case $\mathcal{T} = 29$ min; in the round-beam case $\mathcal{T} = 92$ min. In Fig. 4.5 we plot the accumulation around the ring of the Touschek growth rate. We see from the plot that the Touschek effect is rather evenly distributed around the ring, even in the straights, though a slightly

steeper slope than average can be seen in the two DBA arcs. In more detail, we find that in the TME arcs, which take up 44% of the circumference, about 48% of the Touschek effect occurs; in the DBA arcs, which take up 22% of the circumference, 28% of the Touschek effect occurs. This all suggests that in order to significantly improve the Touschek lifetime by working on the optics will require improvements throughout the ring, in the arcs as well as in the straight regions.

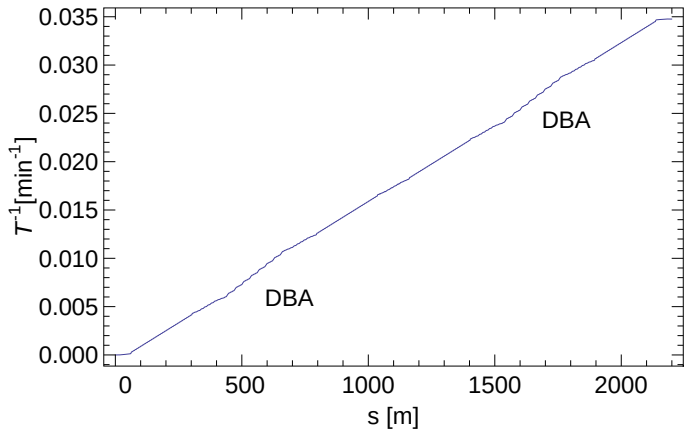

Figure 4.5: Accumulation around the ring of the Touschek growth rate in the nominal PEP-X configuration. A slightly steeper slope than the average can be seen in the two DBA arcs.

4.3 Top-Up Injection

In Section 4.2 the Touschek lifetime, which dominates beam lifetime in PEP-X, was calculated to be 29 minutes for the nominal 158 x 8 pm-rad lattice having an average of 0.475 mA, or 3.49 nC, in each of 3154 bunches (1.5 A, 11000 nC total). With this lifetime, bunch charge, and total stored charge, would decay by 10% in ∼3 minutes. As with present day 3rd generation light sources, the performance of PEP-X for users will be greatly enhanced if "top-up" injection, with beam line safety shutters open, is used to reduce the variation in average ring current to a small value in order to minimize changes in photon intensity on experimental samples and heat load on beam line optical components over the course of experiment data acquisition periods. Several modern light sources have reduced this variation to less than 1% and as low as 0.1% in some cases. In the following we explore the injection requirements for attaining these levels of current constancy for PEP-X.

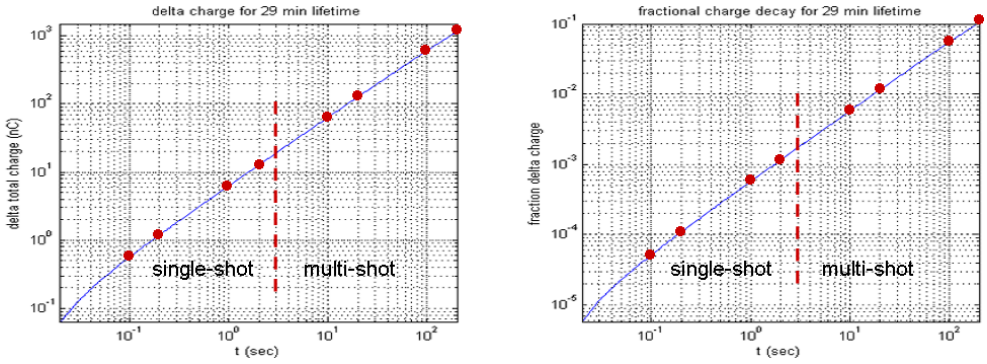

Figure 4.6: Fractional change (left) and absolute change (right) in charge as a function of time for PEP-X with 1.5-A stored current (11000 nC) and a 29-minute lifetime. Red dots indicate some of the possible injection rates and modes. The dividing line between single- and multi-shot modes is approximate and depends on linac charge capability.

Figure 4.6 depicts the fractional and absolute changes in total stored charge as a function of time for the assumed 1.5-A, 29-minute lifetime operating conditions. The graph on the left indicates that, for example, 1% current constancy can be maintained by injecting beam every 20 seconds, and injecting every 2 seconds yields 0.1% constancy. The graph on the right shows the actual value of the charge that would have to be replaced per injection cycle as a function of time.

The number of injection shots that are needed to replace lost charge depends on the single-shot charge capability of the injector linac. Assuming a capability of 1-1.5 nC for single-bunch injection and ∼10-15 nC for multibunch injection (typical values that might be increased with linac development), it can be seen that multiple linac shots would be needed per injection cycle if the time interval between cycles exceeds the order of 0.1 second for single-bunch injection and the order of 1 second for multibunch injection. If single-shot injection time scales are met, than the constancy of stored charge would be better than 0.1%.

Bunch Charge Variation

To better understand the details of the decay and restoration of bunch charge q_b for a machine having such a short lifetime τ, consider that for Toucshek-dominated lifetime where bunch dimensions remain essentially constant, Eq. 4.10 asserts

$$q_b(t)\tau(t) = q_{bavg}\tau_{avg} = constant = Q_b \tag{4.13}$$

where q_{bavg} and τ_{avg} are the average bunch charge and lifetime, respectively (q_{bavg}= 3.49 nC, τ_{avg}= 29 min, and Q_b= 6073 nC-s for 1.5-A operation with ϵ_y= 8 pm-rad). The decay of bunch charge is then

$$q_b(t) = q_b(0)e^{-t/\tau(t)} \cong \frac{q_b(0)}{q_b(0)t/Q_b + 1} = \frac{q_b(0)}{t/\tau(0) + 1}, \ for\ small\ t/\tau \quad (4.14)$$

where $q_b(0)$ is the initial bunch charge, $\tau(0)$ is the lifetime for charge $q_b(0)$, and the approximation is to better than 5% when t <0.2τ. The average charge q_{bavg} over a time interval t_{binj} between injections for a given bunch is

$$q_{bavg}(t) = \frac{1}{t}\int_0^t q_b(t)dt = \frac{Q_b}{t_{binj}}\ln(q_{bmax}t_{binj}/Q_b + 1) \quad (4.15)$$

from which the maximum charge q_{bmax} immediately after injection (=$q_b(0)$)is

$$q_{bmax} = \frac{Q_b}{t_{binj}}(e^{q_{bavg}t_{binj}/Q_b} - 1). \quad (4.16)$$

The bunch charge that must be replaced at injection is given by the difference between q_{bmax} and q_{bmin}, where q_{bmin} is found from Eq. 4.14. Because all other bunches must receive an injection shot before a given bunch can receive its next shot, the time interval t_{binj} is some multiple of the injection repetition period T_{linrep} (= $1/f_{linrep}$ where f_{linrep} is the linac repetition frequency) that depends on the number of injected bunches per shot. For example, with single-bunch injection for each of n_b = 3154 stored bunches from a 5-Hz injector, $t_{binj} = n_b T_{linrep}$ = 631 seconds. For this case the maximum charge, minimum charge and injected charge q_{binj} for a bunch having 3.49-nC average charge are

$$q_{bmax} = 4.21 \text{ nC}$$
$$q_{bmin} = 2.93 \text{ nC}$$
$$q_{binj} = 1.28 \text{ nC}$$

This amplitude modulation of +20% and -16% about the average charge is reduced to the 12% level when 15-bunches are injected every 2 seconds, with t_{binj} = 3150/15 x 2 seconds = 420 seconds, although the total stored charge modulation is increased from .01% to 0.1%.

Bunch Fill Patterns

The variation of bunch charge in the time interval between injections is reflected in the pattern of bunch charge in the storage ring, which depends on the sequence of bunches that are selected for injection. Figure 4.7 depicts

the evolution of the charge profile for a stored bunch train that is refilled with the 15-bunch, 0.5-Hz injector rate mentioned above, where successive groups of 15 bunches are refilled on each injection shot. Over the course of the $3150/15 = 210$ injection shots needed to replenish all bunches, the profile pattern propagates along the bunch train, with the lowest charge group of bunches refilled on the next shot. While there is a $\pm \sim 12\%$ variation in charge along the bunch train, the average total charge remains constant to 0.1%.

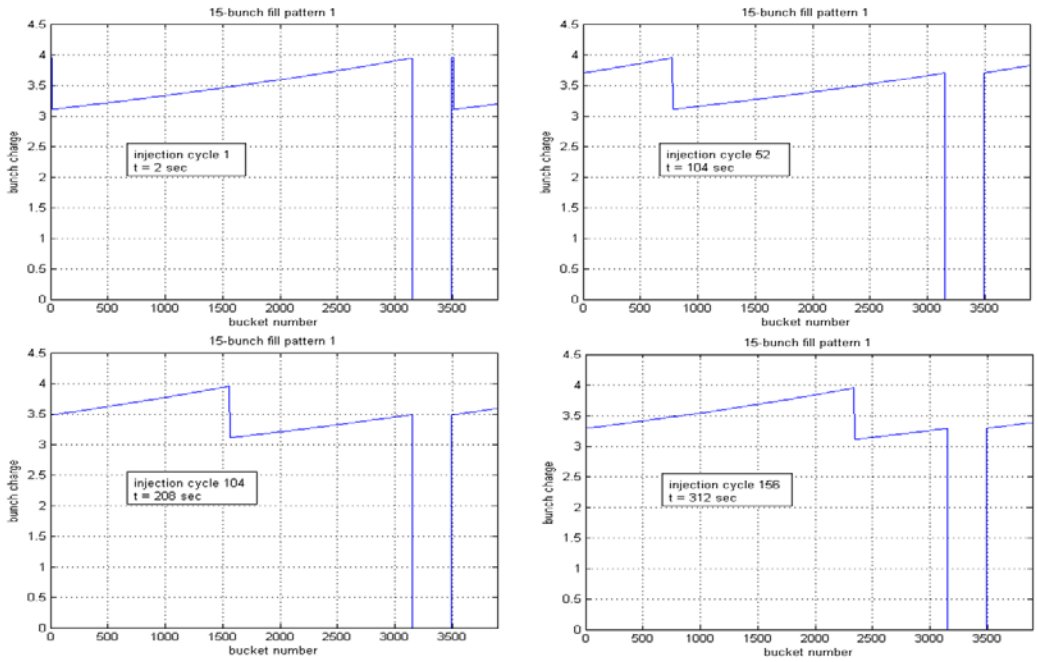

Figure 4.7: Progression of charge profile for bunches stored in 3150 out of 3492 buckets with 15-bunch injection every 2 seconds with 29-min lifetime. 210 injection shots over 420 seconds are needed to refill all bunches. While bunch amplitude modulation is ~25%, the average total charge at any time is stable to 0.12%.

The consequences of this charge amplitude modulation must be considered by the user if it is not filtered out by averaging over several ring revolution periods or by "notching" out the variation by synchronizing data acquisition with respect to the injection time and averaging over a revolution period or a multiple of it. The repetition rate for the modulation pattern can be increased, possibly improving signal smoothing and reducing the sensitivity to the modulation, by altering the injection sequence. Figure 4.8 shows two examples where the injection sequence has been modified to sequentially fill groups of 15 bunches separated by $3150/10 = 315$ buckets, reducing the data integration period needed to reach highly constant average bunch charge by a factor of as much as 10 from that shown in Figure 4.7.

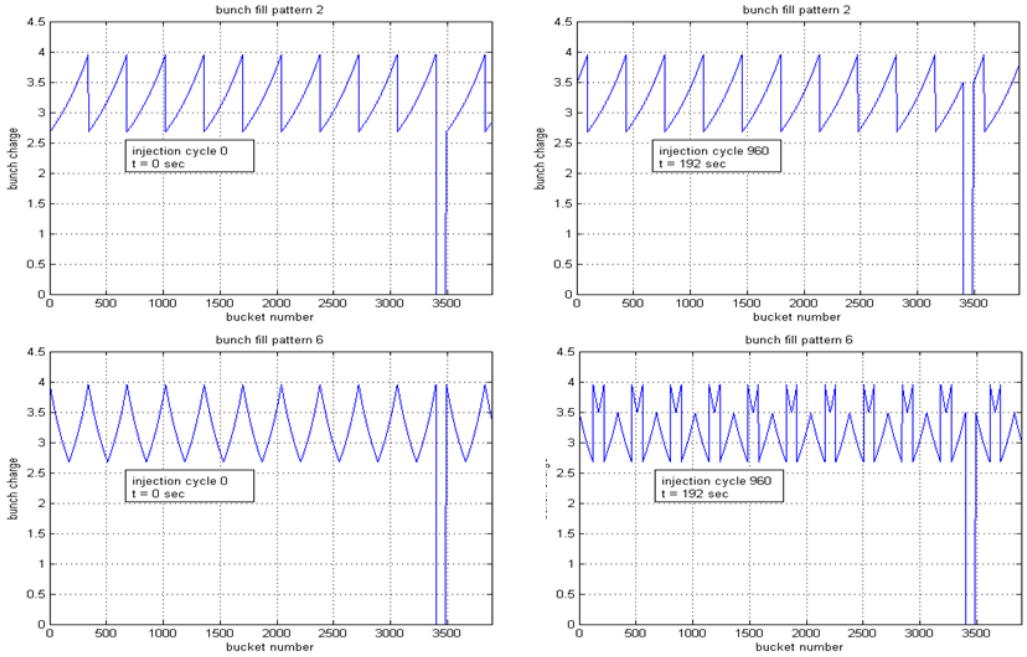

Figure 4.8: Alternative bunch charge profiles that reduce the integration time required to reach a high level of averaged charge constancy to less than one revolution period. In these cases, 3400 bunches with 29-minute lifetime are filled with single-bunch injection from 5-Hz linac over a period of 680 seconds. While the bunch amplitude modulation is ∼38% peak-to-peak, the average total charge at any time is stable to ∼0.01%.

Other bunch profiles are possible, and determining optimal patterns deserves further study.

Injection Orbit Transient

To identify which of the various top-up injection rates and modes are acceptable for users, we derive some approximate estimates of the impact these modes would have on beam quality. For simplicity we assume that a fraction f_{kick} of the stored beam, given by the ratio of the kicker pulse width to the length of the entire stored beam bunch train, is kicked horizontally with the same amplitude by an imperfectly closed kicker bump (using multiple kicker magnets) and that these kicks are repeated every injection cycle time interval T_{cy}. In reality, different bunches within the kicker pulse will receive different amplitude kicks depending on the matching of the individual kicker magnet waveforms and the timing of the bunches with respect to the waveform. The fraction f_{kick} depends on the detailed ring filling pattern and the kicker pulse width. Using the PEP-II kickers, which have a half-sine pulse width of 0.4

μs, f_{kick} = ~0.06 in the 3154-bunch case (6.626 μs bunch train length) and ~90 bunches are kicked.

The kicked bunches will execute coherent betatron oscillations that decay with the horizontal damping time constant τ_x (13.5 ms), unless they are damped more quickly by a fast transverse multibunch feedback system. Damping times on the order of a few tenths of a millisecond might be provided with such a feedback system. Besides simple betatron oscillations, the bunches may exhibit more complex beam dynamics as well, such as size and energy oscillations, amplitude-dependent tune shifts, oscillation decoherence, etc., but all of this behavior will decay with x as well and does not qualitatively alter the following discussion and for simplicity we consider only the coherent betatron oscillations. These oscillations cause orbital position and angle displacements of the kicked bunches at each beam line source point that evolve on a turn-by-turn basis with the betatron frequency (31.35 kHz for the nominal PEP-X lattice). The betatron motion will result in the oscillatory displacement of the radiation from the perturbed bunches in position and angle in the beam line.

While the detailed effect of these perturbations depends on the particular optical configuration of each beam line, perhaps the most sensitive consequence shared by the majority of beam lines is that they will cause the photon beam to move transversely in a small downstream aperture, resulting in variations of transmitted flux through the aperture. Transverse beam displacement in an unfocused beam line is dominated by angular orbit variations at the source point, and that for focused beam lines is dominated by positional orbit variations. Such apertures, which may only be a small number of sigmas of the transverse beam size, are used quite commonly to collimate the beam, limit incident power on downstream optics, or to select a coherent cross-section of the beam. As an example, a transverse beam displacement of order 3 sigmas of the transverse beam size in a 3-sigma aperture will cause a near 100% loss in transmitted intensity for the kicked bunches. Since the PEP-X source point rms beam dimensions will be on the order of a few tens of microns and a few microradians, it is highly likely that kicked bunch amplitudes will be on the order of a few sigmas of the beam size, causing large variations in transmitted photon flux from those bunches through small apertures for the duration of the betatron oscillations.

The impact of injection-induced intensity variations past an aperture is potentially mitigated by at least two filtering processes: 1) the fact that only a fraction f_{kick} of the total number of bunches are perturbed, and 2) averaging of data in the user detector data processing system. Other filtering mechanisms may also be present, such as the inherent signal integration provided by the detector medium itself, but, for this discussion, we consider this effect to be folded into the data averaging process. If one considers the

reduction in beam intensity past a small aperture on the first turn around the ring after the injection kick, it is likely that the radiation from the kicked bunches could entirely miss the apertures in some of the beam lines. The transmitted intensity averaged over one turn could then be reduced by as much as the fraction f_{kick}. If intensity is averaged over many turns, the reduction is $<f_{kick}$ since the beam from the kicked bunches oscillates in and out of the aperture. The longer the averaging period, the less the kick-induced intensity variation in the averaged data. If the data is averaged over a few transverse damping times (of order 50 ms and 0.5 ms without and with transverse feedback, respectively), then virtually no intensity fluctuations are detected for single-shot injection modes, just a small reduction in averaged intensity that would differ from an average taken over a period without an injection transient. Data averaging must extend over the duration of multi-shot injection modes, which could be on the order of a second or more, to filter out the related intensity variations.

The averaging period required to reduce intensity variations to acceptable levels for a given experiment depends on the orbit perturbation amplitude, f_{kick}, aperture dimensions, optics and detector details, and the ability of the user to normalize data to real-time incident intensity. With this latter capability the tolerance for absolute intensity stability can be relaxed, but in many cases the normalization is only effective over a limited dynamic range of intensity variations and it does not necessarily compensate for nonlinearities in the measurement system. Without effective data normalization, many experiments require absolute intensity stability at the 0.1% level over the course of their data acquisition periods. This is especially true for high resolution spectroscopy where the photon energy is scanned and very small changes of sample response are measured. The requirement for a 0.1% level of stability implies that either the injection-induced orbit perturbation must be reduced to a very small level, or sufficient averaging must be invoked, or data acquisition must be gated to blank out the injection transient, or a combination of all of these is needed. Data gating or some other form of timing synchronization with unperturbed bunches will be required for high-bandwidth experiments having data acquisition times less than beam damping times. An extreme case of a high bandwidth experiment is one that measures the time response of a sample pumped by a laser pulse and probed by a single x-ray pulse from a single bunch on a single turn. This experiment will require a gating system to ensure that the probe bunch is unperturbed by the injection kick.

Injection Duty Cycle

The time interval between injection cycles T_{cy} becomes important for experiments that rely on data gating, in relation to the disturbance period T_{inj} of the injection shot(s). The fractional duty cycle f_{duty} of an unperturbed beam is

$$f_{duty} = 1 - T_{inj}/T_{cy} \tag{4.17}$$

For single-shot injection, either single- or multi-bunch, the disturbance time T_{inj} can be taken to be $\sim 4\tau_x$ (= ∼50 ms or ∼2 ms, without and with a transverse feedback system), although more time may be needed to damp large amplitude oscillations to a small fraction of the beam size. For multi-shot injection with n shots, $T_{inj} = nT_{linrep}+ \sim 4\tau_x$, where $T_{linrep} = 1/f_{linrep}$ is the linac multi-shot repetition period. Fractional duty cycles for various injection mode examples are given in Table 4.3.

Table 4.3: Unperturbed beam duty cycle fraction f_{duty} for single- and multi-shot injection modes having various orbit perturbation periods T_{inj} and injection cycle times T_{cy}, assuming 1.3 nC per bunch from the injector in single-bunch mode. Damping times of 4 τ_x (τ_x = 13.5 ms without transverse feedback and is estimated to be 0.5 ms with feedback) are assumed to be sufficient to reduce oscillation amplitudes to a small fraction of the beam size; more time may be needed for large amplitude oscillations.

shot mode	# shots	bunch /shot	Q_{inj} [nC]	$\Delta Q/Q$ [%]	T_{inj} [s] no/with fdbk	T_{cy} [s]	f_{duty} no/with fdbk
single	1	1	0.63	0.006	0.050 / 0.002	0.1	0.500 / 0.980
single	1	1	1.28	0.01	0.050 / 0.002	0.2	0.750 / 0.990
single	1	15	6.3	0.06	0.050 / 0.002	1	0.950 / 0.998
single	1	15	12.7	0.12	0.050 / 0.002	2	0.975 / 0.999
mult, 10 Hz	100	1	127	1.2	10.050 / 10.002	20	0.498 / 0.500
mult, 10 Hz	10	15	127	1.2	1.050 / 1.002	20	0.948 / 0.950
mult, 30 Hz	100	1	127	1.2	3.383 / 3.335	20	0.831 / 0.833
mult, 30 Hz	10	15	127	1.2	0.383 / 0.335	20	0.981 / 0.983
mult, 60 Hz	100	1	127	1.2	1.717 / 1.669	20	0.914 / 0.917
mult, 60 Hz	10	15	127	1.2	0.217 / 0.169	20	0.989 / 0.992
mult, 10 Hz	100	15	1270	12	10.050 / 10.002	200	0.950 / 0.950
mult, 30 Hz	100	15	1270	12	3.383 / 3.335	200	0.983 / 0.983
mult, 60 Hz	100	15	1270	12	1.717 / 1.669	200	0.991 / 0.992

It is clear from the examples shown in the table that, to maximize f_{duty}, multibunch linac operation is preferred for either single-or multi-shot injection modes and that, with no transverse feedback system, longer intervals between injections with rapid refills (i.e. with 60-Hz linac repetition rate) will

yield higher duty factors at the expense of reduced stored charge constancy. A transverse multibunch feedback system will be effective in increasing duty cycle for single-shot injection modes.

Radiation Safety

With a 29-minute lifetime and frequent top-up injection to maintain a 1.5-A stored beam with high constancy, the total average charge loss rate will be 6.3 nC/s, with charge restored from a 6.3-nA injector. The associated beam loss and injected beam power is ∼30 W. The 29-minute lifetime as calculated assumes that stored beam losses will be distributed around the ring at points where off-energy, Touschek-scattered particles hit a physical vacuum chamber aperture. These loss points are likely to be located at small-aperture chambers, such as those for insertion devices, or in chambers of limited width where the horizontal dispersion is large. Some fraction of the lost particles will generate radiation in sectors of the ring containing beam lines where it must be intercepted by shielding walls or localized shielding configurations that reduce the radiation dose rates in areas of human occupation to acceptably low levels as specified by the radiological control standards at SLAC (typically <0.1 mrem/hr). Tunnel roof shielding must be sufficient to reduce sky-shine to acceptable levels as well. While a detailed study of radiation shielding requirements have not yet been conducted, it is anticipated that they are relatively standard and will be met in general with concrete wall thicknesses in beam line areas of <5 feet.

Top-up injection with safety shutters open poses a potential additional radiation hazard that must be mitigated. Not only will the radiation dose rates generated by injected beam loss be larger than those during ambient beam storage, which must be accommodated by the beam line shielding configuration, but there is a small chance that, due to mis-configuration of lattice magnet field strengths or some mismatch in injected and stored beam energy, some or all of the injected electrons could propagate down an open beam line, causing excessive instantaneous radiation levels on the experimental floor. Fortunately there are methods to eliminate this scenario, as implemented by several light sources already, that include detecting the presence of stored beam before permitting top-up injection (thus assuring that magnetic field strengths are at their nominal levels), installing interlocks on critical magnet power supplies to guarantee they are operating at safe levels, installing a beam energy collimator in the injection line to assure that injected and stored beam energies are matched, etc. Detailed injected beam loss studies are required to determine the components needed for such a top-up injection safety system. The complexity of this study might be greatly reduced in the PEP-X case since there is ample, uncluttered room in the

tunnel on each long beam line to install a clearing magnet that would bend any wayward electrons down to the floor before reaching the shielding wall penetration, providing the necessary radiation safety.

Summary

The following conclusions about top-up injection into PEP-X with a 29-minute lifetime can be drawn from the above discussion:

- Stored current constancy of <0.1% to ∼1% can be achieved with a linac injector.
- The unperturbed beam duty cycle as well as the degree of current constancy should be considered in selecting injection modes and rates. The highest duty cycles are reached with multi-bunch injection and they are reduced with multi-shot injection.
- Experimental data filtering and gating methods will be required to mitigate the effects of stored beam orbit transients during frequent top-up injection.
- The fraction of stored beam that is perturbed at injection is reduced with shorter kicker pulse width. A pulse width less than the present 0.4 μs for PEP-II kickers would be beneficial.
- The amplitude of the stored orbit perturbation depends on the quality of the closed-orbit bump they produce, which in turn depends on the matching of individual kicker magnets in amplitude, pulse width, rise- and fall-times, and timing. The possibility to minimize the perturbation by kicker waveform matching is maximized when the kicker bump is contained within a single straight section having no intervening quadrupoles and sextupoles that would cause amplitude-dependent kicks and bump mismatch during the kicker rise- and fall-times. It might be possible to implement an alternate injection scheme to greatly reduce the orbit transient using a single pulsed multipole magnet, where the stored beam passes through the zero-field center and the injected beam passes off-center to receive a transverse kick.
- The duration of the stored beam orbit transient can be greatly reduced using a fast multi-bunch transverse feedback system.

Chapter 5

RF System

5.1 Ring and RF Parameters

The main task of the PEP-X RF system is to provide the power to the beam necessary to compensate the beam energy losses and to control the longitudinal beam stability in the ring. The main parameters of the machine, which will be used in this chapter, are shown in Table 5.1. The majority of the

Table 5.1: Main parameters of the machine.

Parameter	Symbol	Value	Units
Beam energy	E	4.5	GeV
Beam current	I	1.5	A
RF frequency	f_{RF}	476.0015	MHz
Revolution frequency	f_{rev}	136.312	kHz
Bunch spacing	τ_b	2.1	ns
Harmonic number	h	3492	
Number of bunches	n_b	3154-3422	
Energy loss	U_0	3.12	MeV/turn
Momentum compaction	α	$5.81 \cdot 10^{-5}$	
Relative energy spread	σ_δ	$1.14 \cdot 10^{-3}$	
Longitudinal damping time	τ_s	10.8	ms
Total RF voltage	V_{RF}	8.9	MV

beam losses comes from the synchrotron radiation in bending magnets and wigglers. The main part of this radiation is incoherent radiation power, which is proportional to the beam current and the fourth power of the beam energy. There is also a small amount of coherent synchrotron radiation (CSR), which is proportional to the square of the beam current. The beam also

loses energy due to wake fields, which are excited in the beam pipe vacuum elements. Wake fields include short-range and long-range fields. Short-range fields are mainly resistive-wall and geometrical wake fields. Long-range fields include higher order modes (HOMs) excited in the RF cavities or kickers and geometrical cavities in the beam pipe, for example between in and out tapers. The power of the wake fields, like the power of CSR, is proportional to the square of the beam current. Total beam losses are:

$$P_{beam} = U_0 \times I + Z_{HOM} \times I^2 \tag{5.1}$$

The averaged HOM impedance is proportional to the bunch spacing τ_b and loss factor K of the ring:

$$Z_{HOM} = \tau_b \times K \tag{5.2}$$

The ring loss factor must not include the loss factor of the cavity main mode. The loss factor strongly depends upon the bunch length. The natural (zero current) bunch length may be calculated using the formula

$$\sigma_z = \frac{c\sigma_\delta}{f_{RF}} \times \sqrt{\frac{\alpha h}{2\pi} \times \frac{E}{eV_{RF}\cos(90^0 - \phi_s)}} \tag{5.3}$$

where synchronous phase should satisfy the equation:

$$\sin(90^0 - \phi_s) = \frac{U_0}{eV_{RF}} \tag{5.4}$$

Synchrotron oscillation tune and synchrotron frequency are calculated using these formulas:

$$\nu_s = \sqrt{\frac{\alpha h}{2\pi} \times \frac{eV_{RF}\cos(90^0 - \phi_s)}{E}} \tag{5.5}$$

$$f_s = \nu_s f_{rev} = \nu_s \frac{f_{RF}}{h} \tag{5.6}$$

Values for these parameters and synchrotron loss power, calculated from the ring parameters (Table 5.1) are shown in Table 5.2. There must also be additional power to compensate the main mode Joule losses in the room-temperature cavities. This power is proportional to the square of the total RF voltage and inversely proportional to the shunt impedance of a cavity and the number of cavities:

$$P_{cav} = \frac{V_{RF}^2}{2Z_{sh}N_c} \tag{5.7}$$

Table 5.2: Other parameters of the machine.

Parameter	Symbol	Value	Units
Synchrotron phase	ϕ_s	69.5	degrees
Synchrotron tune	ν_s	0.0077	
Synchrotron frequency	f_s	1.054	kHz
Bunch length	σ_z	3.0	mm
S. R. Power	P_{SR}	4.68	MW

With unmatched conditions when the beam is not perfectly coupled to the cavity, some power will be reflected back from a cavity. We must also include this in the total power consideration. The reflection coefficient can be described by the formula:

$$\Gamma = 1 - \frac{\alpha_{cav}}{1 + \frac{P_{beam}}{(\beta+1)P_{cav}}} \tag{5.8}$$

where α_{cav} and β are geometrical parameters of a cavity. *beta* represents also the coupling coefficient or coupling factor. The reflected power is proportional to the incident power and reflection coefficient squared:

$$P_{ref} = P_{in} \times \Gamma^2 \tag{5.9}$$

So the total incident power will be the sum of beam power loss, cavity losses and reflected power

$$P_{in} = P_{beam} + P_{cav} + P_{ref} \tag{5.10}$$

5.2 Beam and RF Power

Preliminary analysis for possible RF system design can be found in reference [18]. The choice of the RF voltage and number of cavities is based on the bunch length, the maximum operational voltage in a cavity and the maximum transmitted and reflected power through a cavity RF window necessary to separate the cavity vacuum from the waveguide. The existing coupling factor may limit the total beam current because of large reflected power with unmatched conditions. For the PEP-X RF system we propose to re-use the main elements of the PEP-II RF system such as klystrons, modulators, circulators and cavities with coupling boxes. SLAC PEP-II RF operational experience shows that the power limit for each cavity window is 500 kW [19]. Stable operational voltage in one cavity should be limited to 750-800 kV to avoid cavity arcs. One klystron may supply power for two cavities. Pa-

rameters of a PEP-II cavity are shown in Table 5.3. Detailed information about calculated and measured parameters of the longitudinal and transverse modes of the PEP-II cavity is given in reference [20]. For a given coupling

Table 5.3: PEP-II cavity parameters

Parameter	Value	Units
RF frequency	476	MHz
Shunt impedance Z_{SH}	3.8	MOhm
Unloaded Q_0	32000	
Z_{SH}/Q_0	117	Ohm
Coupling factor β	3.6	
Maximum incident power	500	kW
Maximum cavity voltage	0.75-0.9	MV

factor we may optimize the transmitted power to the beam. The ratio of the incident power to the beam loss, as a function of a ratio of the beam losses to PEP-II cavity losses, is shown in Fig. 5.1

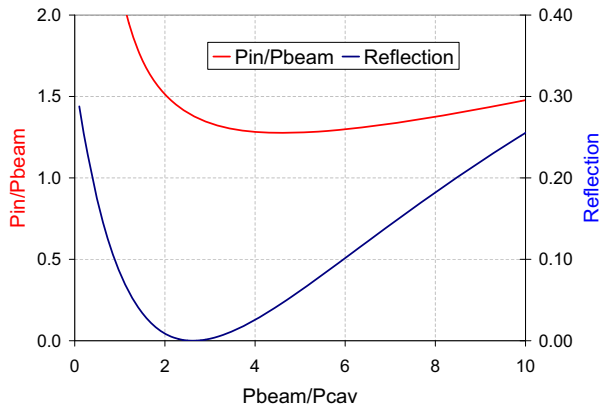

Figure 5.1: Efficiency of the transmitted power to the beam and reflected coefficient squared as a function of the ratio of beam losses to cavity losses. Coupling factor $\beta = 3.6$.

With the PEP-II coupling factor($\beta = 3.6$), the minimum reflected power is achieved when beam losses are 2.2 times larger than the cavity losses. However, the minimum incident power is achieved with a higher ratio of beam to cavity power (4 to 6). Based on this optimization for the PEP-X parameters and taking into account power and voltage limits we can calculate the necessary number of cavities and klystron (stations), and the supply power. For the HOM power calculation we use the PEP-II LER impedance. Table 5.4 shows the RF parameters for three possible cases.

Table 5.4: Number of RF stations/cavities and RF power($\beta = 3.6$)

Number of RF stations	6	7	8
Number of RF cavities	12	14	16
Voltage per cavity [MV]	0.74	0.63	0.56
HOM power [MW]	0.24	0.24	0.24
All cavity losses [MW]	0.87	0.74	0.65
Total reflected power [MW]	0.56	0.82	1.1
Reflected power from one cavity [MW]	0.047	0.059	0.069
Incident power for one cavity [MW]	0.53	0.46	0.42
Power from one RF station [MW]	1.06	0.92	0.84
Total incident power [MW]	6.34	6.49	6.68
Power consumption (50% efficiency) [MW]	12.68	12.98	13.37

In the first case we need only 6 klystrons and 12 cavities; however the cavity voltage and transmitted power reach their maximum values. For a combination of 7 or 8 klystrons, voltage and transmitted power are much more relaxed, but power consumption is larger. We assume that klystrons have 50% efficiency.

We can consider using 6 stations and having two spares if the impedance of the detuned four cavities will not introduce bunch instability. The klystrons required, plus several spares, exist at SLAC, although more klystrons may eventually need to be built to replenish the supply as tubes age. We can also change the coupling factor in order to decrease the reflected power and power consumption. Table 5.5 shows that we could gain more than one megawatt of power by changing the coupler factor from 3.6 to 6 by modifying only the coupler box (Fig 5.2.)

We can change the coupling with a change of the small dimension of the waveguide leading to the coupler slot (Fig. 5.2) for 1/4 of a wavelength, forming a quarter-wave transformer. The waveguide impedance varies directly with this dimension. A coupling factor of up to 6 is achievable without changes to the cavity itself. Since the quality of the match varies only slowly with β, we may optimize for a fixed coupling factor for all cavities.

5.3 Gap Transient and Frequency Detuning

The existence of an ion-clearing gap in the electron bunch train causes a change in cavity voltage and phase along the bunch train. The cavity voltage change further causes a change in synchronous phase of the electron bunches. The result is a turn-by-turn "phase transient" or "gap transient." The phases

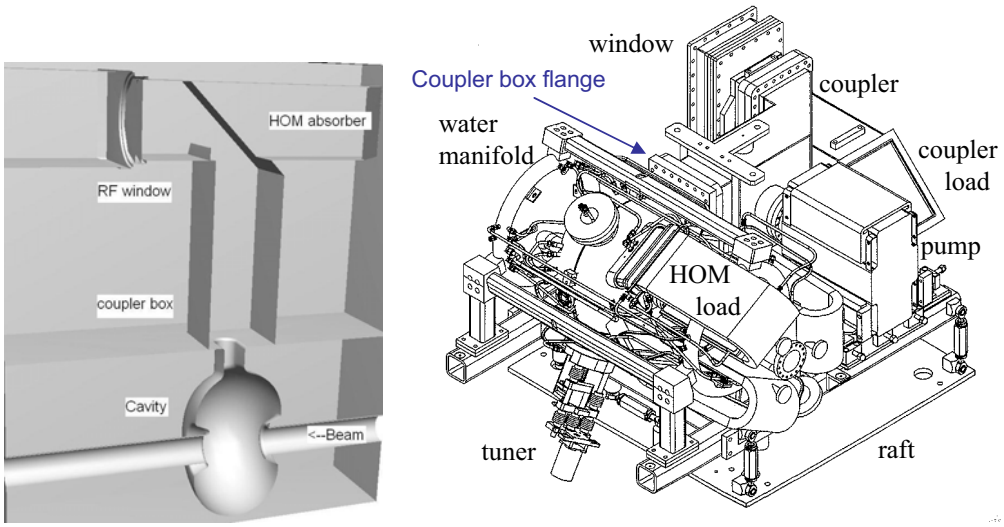

Figure 5.2: PEP-II cavity, coupler box and RF window.

of the electron bunches will be modulated at the revolution harmonics. The phase shifts along a bunch train are shown in Fig. 5.3 for 16 cavities with the PEP-II coupling (left plot) and for 12 cavities and a modified coupling of 6 (right plot). To avoid resonant instability at the main frequency (i.e.

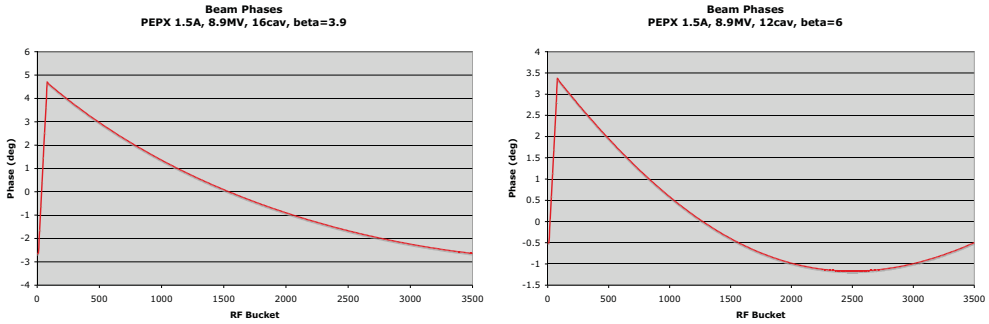

Figure 5.3: Phase transient. Left plot: 16 PEP-II cavities and no change in cavity coupling.Right plot: 12 cavities with coupling changed to 6.

to compensate for beam loading), the RF cavities must be detuned from resonance according to the following formula:

$$\delta f = -f_{RF} \times \frac{Z_{sh}}{Q_0} \times \frac{I}{V_{RF}} N_c \tag{5.11}$$

For the PEP-X parameters the maximum detuning is 108 kHz for 12 cavities and 152 kHz for 16 cavities that is below and and above one revolution harmonic. The feedback system must be designed to damp this -1 mode.

Table 5.5: Number of RF stations/cavities and RF power ($\beta = 6.0$)

Number of RF stations	6	7	8
Number of RF cavities	12	14	16
Voltage per cavity [MV]	0.74	0.63	0.56
HOM power [MW]	0.24	0.24	0.24
All cavity losses [MW]	0.87	0.74	0.65
Total reflected power [MW]	0.1	0.22	0.36
Reflected power from one cavity [MW]	0.008	0.016	0.02
Incident power for one cavity [MW]	0.49	0.42	0.37
Power from one RF station [MW]	0.98	0.84	0.74
Total incident power [MW]	5.89	65.89	5.94
Power consumption (50% efficiency) [MW]	11.77	11.77	11.88

We can check beam stability for higher order modes using the same approach as in reference [21]. HOM cavity impedance must be less than the stability threshold defined by the beam and ring parameters including the radiation damping time τ_s

$$Z_{th}(\omega) = \frac{4\pi E \nu_s}{\alpha \tau_s N_c I \omega} \tag{5.12}$$

Figure 5.4 shows the impedance of a PEP-II cavity ([20]) and thresholds for 12 and 16 cavities. The left peak is a fundamental mode at 476 MHz. All cavity HOMs are below the threshold, so no feedback to damp HOMs is required.

5.4 RF Systems

RF stations are located in the support building (Fig. 5.5). Each station consists of a 2 MW (90 kV, 23 A) high voltage power supply (HVPS), a 1.2 MW klystron amplifier with a high-power circulator for protection of the klystron from reflected power, and a power splitter (Magic-tee with a 1.2 MW RF load) followed by a waveguide distribution system from the surface level down to the tunnel ending by two cavities. The RF distribution is via a WR2100 waveguide, chosen primarily for low group delay. Each cavity has three HOM loads [22]. For safety, these loads were specified for up to 10 kW dissipation each.

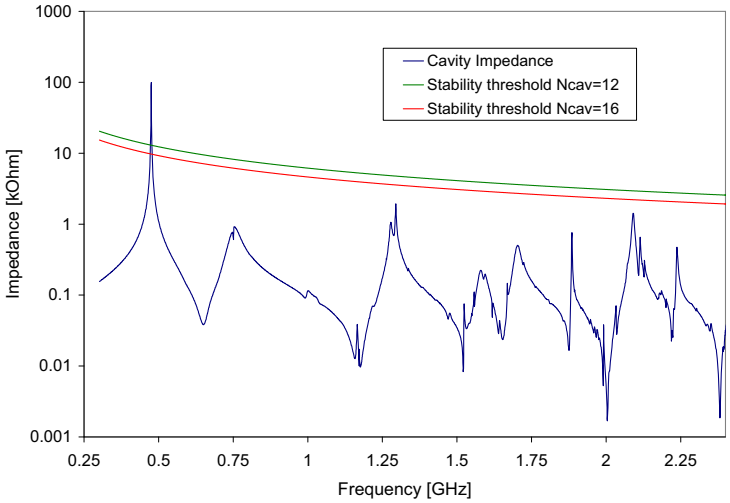

Figure 5.4: Impedance of a PEP-II cavity (blue line) and thresholds for 12 (green line) and 16 cavities (red line).

5.4.1 Low Level RF System

A low-level RF system provides control and feedback for stable multi-bunch high current operation. There are several feedback loops (Fig. 5.6). The direct loop is required for lowering the cavity impedance to reduce multi-bunch oscillations of the beam. Functionally the direct loop keeps the gap voltage constant as set by a DAC reference over an 800 kHz bandwidth. The loop compares the combined baseband field signals of a station's cavities to the reference generated by the gap module. The resultant error signal is up-converted to RF and drives the klystron. The direct loop contains a PID controller with an integral compensation for smoothing out the ripple caused by the klystron high voltage power supply and lead compensation that increases the bandwidth and gain of the loop. The direct feedback loop options control the optional functions of the direct loop: frequency offset tracking, integral compensation and lead compensation. The frequency offset tracking loop takes out the phase shift caused by the detuning of the cavities during heavy beam loading. It is used as a diagnostic for adjusting the waveguide network. The comb loop provides additional impedance reduction for the cavities at specific synchrotron frequency sidebands around the revolution harmonics of the beam. It operates over a bandwidth of 2 MHz and includes a 1 turn delay. The tuner loop tunes and maintains each cavity at resonance. It corrects for thermal frequency variations and compensates cavity beam loading by keeping the phase relationship between forward power and cavity field, as seen by the cavity probe, constant. The relevant phases are measured by digital IQ detectors and the loop is completed in software con-

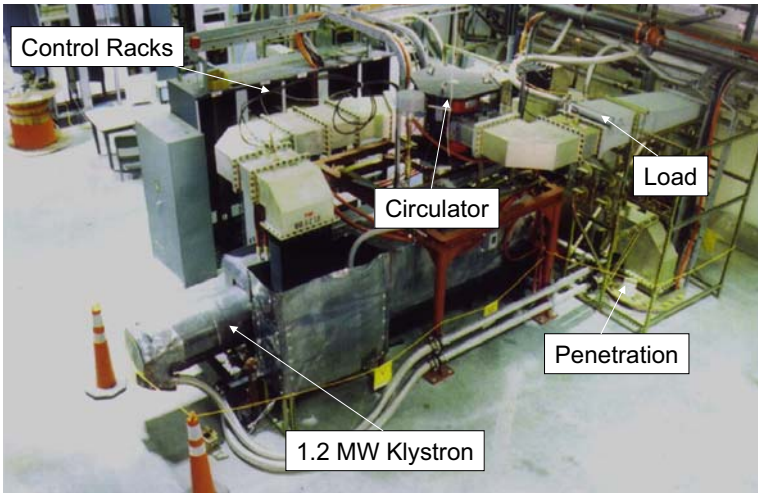

Figure 5.5: PEP-II RF station.

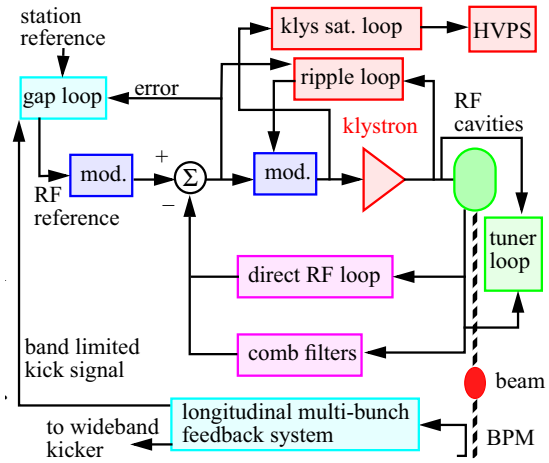

Figure 5.6: Block diagram of RF feedback circuits.

trolling the tuner position via a stepping motor. The HVPS loop adjusts the voltage to the klystron to provide sufficient output power to operate the station under whatever gap voltage or beam loading is requested. Functionally the loop keeps the klystron operating at about 10% below saturated output power. The loop measures the drive power at the input to the klystron and compares it to the ON CW drive power set-point. Based on the error, the set-point for the high voltage power supply is adjusted upward for excessive drive and downward for insufficient drive. This is a slow loop with about a 1 Hz bandwidth. The DAC loop is a slow (0.1 Hz bandwidth) loop in software which functionally keeps the measured gap voltage of the station equal to it's requested "Station Gap Voltage" by adjusting the DAC in the gap voltage feed-forward module. The ripple loop is intended to remove amplitude and

phase ripple in the klystron output power but at the time it is only utilized to keep the low bandwidth phase across the klystron and drive amplifier constant as the klystron voltage is varied. The gap feed forward loop is required to tell the direct loop to ignore the effects of the ion-clearing gap in the beam bunch train. Functionally the loop learns about the variation in the klystron drive caused by the beam gap and adds an equal variation in the reference signal so that the error signal driving the klystron stays unchanged. This loop adapts fully in about 1000 beam revolutions. The longitudinal feedback woofer is the third cavity impedance reduction loop along with the direct loop and the comb loop. It derives it's information from the lowest beam oscillation modes detected by the longitudinal multi-bunch feedback system and uses one RF station in each ring as a powerful longitudinal kicker.

Chapter 6

Impedance Calculations

Most of the vacuum chamber components have complex geometries, and thus numerical simulations are required in order to evaluate their effects on the beam as well as their operational performances. The calculations will address the following potential issues for the ring

- *Broadband impedance* - short-range wakefields contributed by all the vacuum chamber components which may lead to single-bunch instabilities
- *Narrow-band impedance* - long-range wakefields from resonances in cavity-type structures which may lead to coupled-bunch instabilities
- *Beam heating* - higher-order-mode (HOM) power generated by the beam may produce excessive heat loads, especially for those vulnerable components such as bellows
- *Device performance* - determine whether pickup devices such as BPM and kickers meet operational requirements

The vacuum chamber components used in the impedance calculations are primarily based on the PEP-II designs. In PEP-X, the straight sections remain the same as the PEP-II's, using circular beampipes with a radius of 48 mm. The arc sections of the PEP-X vacuum chamber adopt an elliptical cross section with horizontal and vertical axes of 75 mm and 25 mm, respectively. The geometries of some vacuum chamber components such as the BPM need to be scaled or adjusted in order to fit in the elliptical chamber. For those components that are new to PEP-X such as the undulator and wiggler chambers, their dimensions are adapted from existing light sources.

The calculations carried out here will focus on the determination of the broadband impedance of individual vacuum chamber components. Narrow-band impedances appear mostly in the rf cavity, and they are the same as

those of PEP-II's, which have been calculated and compared with measurements. For completeness, both the measured longitudinal and transverse narrow-band impedance of the PEP-II rf cavity will be listed in the following subsections.

6.1 Longitudinal Broadband Impedance

The wakefields of the major vacuum chamber components for PEP-X are calculated using the finite-element time-domain code T3P [23]. The goal is to determine the contributions of individual components to the longitudinal broadband impedance budget. In the following subsection, a brief description of each vacuum chamber component will be given, and its longitudinal short-range wakefield will be calculated using the nominal bunch length of 3 mm. In the subsequent sections, a longitudinal broad-band impedance model will be developed by fitting to the short-range wakefields.

6.1.1 Wakefield Calculations

RF cavity

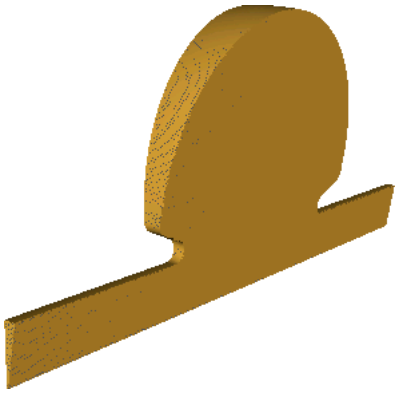

Figure 6.1: The PEP-II rf cavity, showing a 10° slice in the azimuthal direction.

The PEP-II rf cavity consists of a power input coupler at the cavity top and three HOM couplers placed at 120 degrees to each other. The details of the couplers can be ignored in evaluating the short-range wakefield, and a simplified cylindrically symmetric model as shown in Fig. 6.1 is used for the calculation.

Beam position monitor (BPM)

The design of the BPM needs to take into account the effects of impedance, heating and signal sensitivity. The BPM for PEP-X consists of four buttons

placed symmetrically around the beampipe. Based on a recent PEP-II BPM design, the diameter of the button is chosen to be 7 mm, with a ceramic ring for vacuum seal located between the button and the coax (see Fig. 6.2).

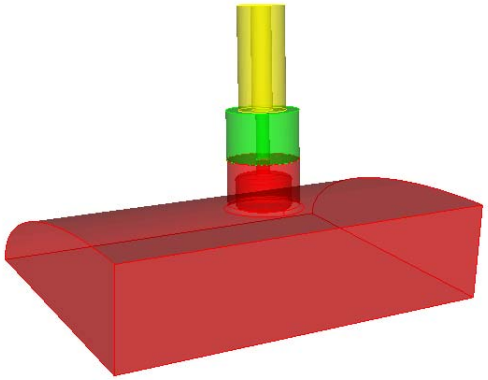

Figure 6.2: A quarter model of the BPM, showing a button located at the top wall of the vacuum chamber.

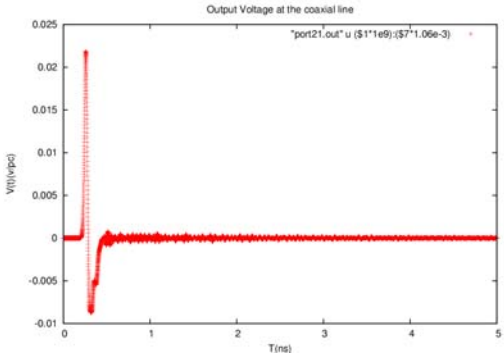

Figure 6.3: BPM response to a passing bunch.

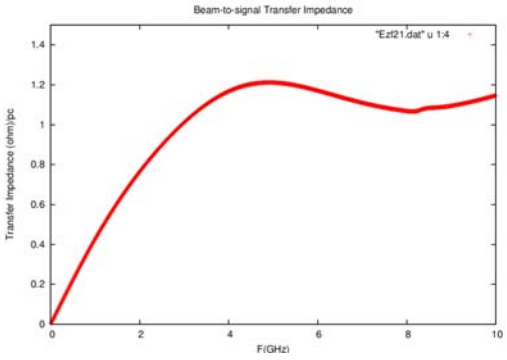

Figure 6.4: Transfer impedance of the BPM.

In addition to determining the short-range wakefield caused by a beam transit, the signal sensitivity of the BPM can also be obtained by monitoring the signal propagating in the coaxial cable. The signal at the coax as a function of time is shown in Fig. 6.3 and the transfer impedance for the signal is shown in Fig. 6.4. The transfer impedance at 1 GHz is found to be 0.4 Ω.

Undulator taper

The undulator transition connects the undulator elliptical chamber with major and minor axes 50 mm x 6 mm to the normal elliptical vacuum chamber with major and minor axes of 75 mm x 25 mm. The transition is chosen to have an angle of 5.71 degrees (1 to 10 aspect ratio) in the vertical direction. Since the transition goes up at the downstream side of an undulator

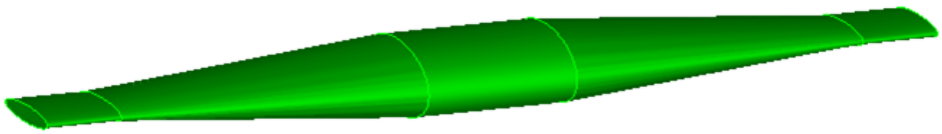

Figure 6.5: Undulator transitions.

chamber and down at the upstream side of another, a geometry as shown in Fig. 6.5 is used to facilitate the wakefield calculation.

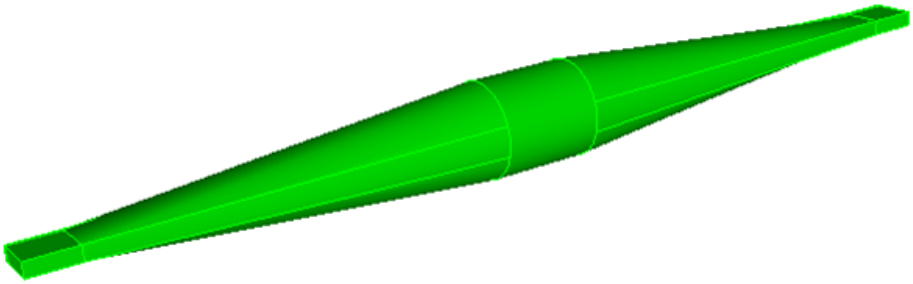

Figure 6.6: Wiggler transitions.

Wiggler taper

The wiggler transition connects the wiggler chamber with rectangular cross section 45 mm x 15 mm to the normal circular straight section vacuum chamber with 48 mm radius. The transition is chosen to have an angle of 5.71 degrees (1 to 10 aspect ratio) in the vertical direction. Since the transition goes up at the downstream side of an undulator chamber and down at the upstream side of another, a geometry as shown in Fig. 6.6 is used to facilitate the wakefield calculation.

Bellows

The impedance of a bellows is determined by the gaps of the sliding fingers and a mask located nearby to shield synchrotron radiation. A mask with 2 mm height placed azimuthally around the vacuum chamber wall is used for the calculation. As expected, the wakefield due to the finger gaps is much smaller compared to that of the mask.

Arc chamber slot

A pumping slot of 8 mm width is located at the far side of the elliptical chamber, and thus its impedance is expected to be low. Tapers inside the slot at both ends further reduce the impedance (see Fig. 6.7). The total

Figure 6.7: Arc chamber slot. Shown here is a half model with the slot located at the left hand side.

wakefield of 720 slots is found to be very small and their contribution to the impedance budget can be ignored.

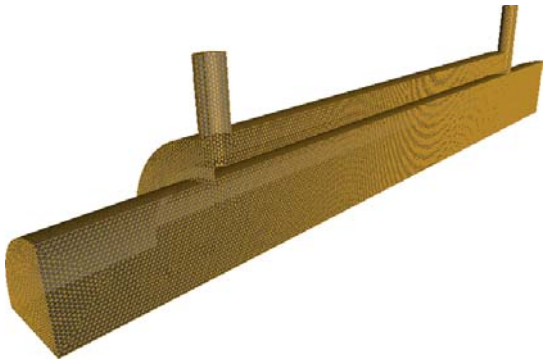

Figure 6.8: Half model of the transverse feedback kicker.

Transverse feedback kicker

The PEP-II transverse feedback kicker consisting of two electrodes is used for the calculation (see Fig. 6.8).

Injection kicker

A DELTA-type injection kicker with 12 mm wide slots between the electrodes is used for the calculation (see Fig. 6.9).

The breakdown of the short-range wakefield of the vacuum chamber components is shown in Fig. 6.10, where the wakefield of a component has been multiplied by its total number in the ring . Note that the wakefields of the kickers, arc-chamber and bellows slots are scaled upward by a factor of 10. It can be seen that the dominant contributions to the impedance budget come from the rf cavities, undulator and wiggler tapers, BPMs and resistive wall.

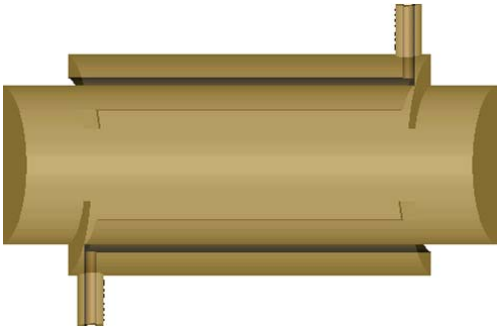

Figure 6.9: Half model of the injection kicker.

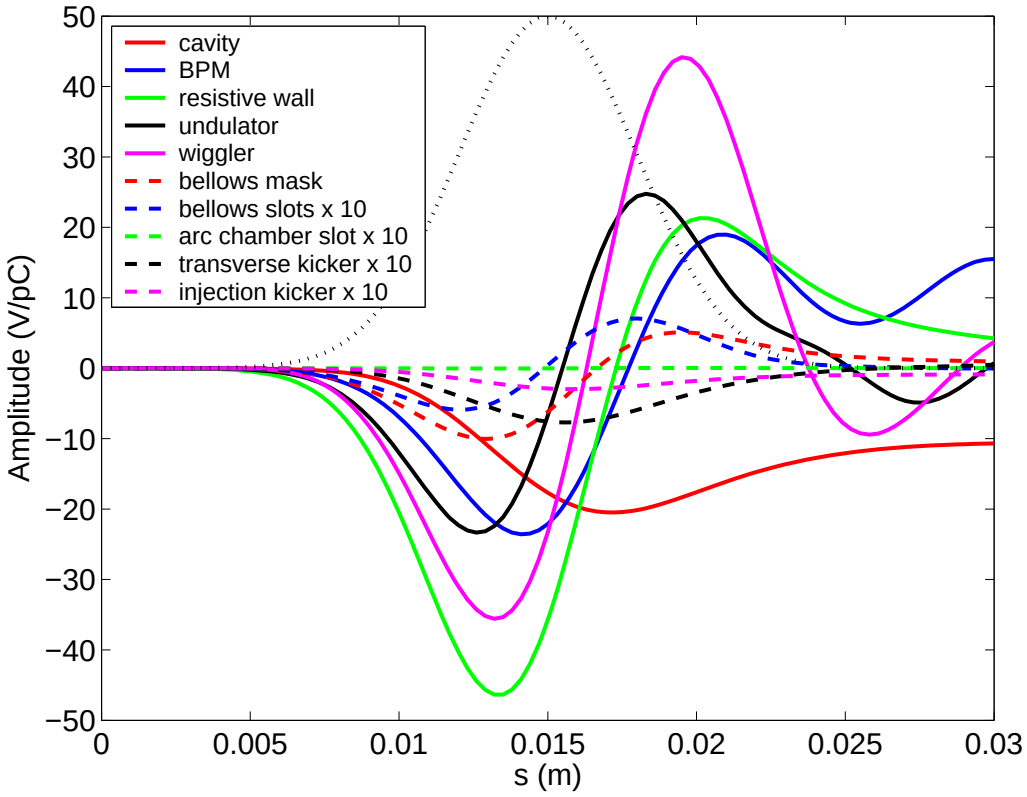

Figure 6.10: Contributions of vacuum chamber components to the total longitudinal short-range wakefield of the ring. Note that the wakefields of the kickers, arc chamber and bellows slots are scaled upward by a factor of 10.

6.1.2 Longitudinal Broadband Impedance Model

We generate wake functions corresponding to a length $\sigma_z = 0.5$ mm for all impedance objects in the ring. The contributions from the individual objects are finally summed up, to yield a wake that can be used as a pseudo-Green function in instability calculations. A second goal of this work is to obtain an impedance budget, a table that can give us an idea of the relative importance of the impedance sources, at nominal bunch length.

We have two comments concerning this work:

- The choice of $\sigma_z = 0.5$ mm for the pseudo-Green function when the nominal bunch length is 3 mm is possibly adequate though somewhat arbitrary. An effect of this choice is to artificially damp instabilities whose wave number $k \gtrsim 2$ mm^{-1} (where we have little information about the impedance). As more information about the high frequency behavior of the impedance (of components) becomes available, one can consider the use of an even shorter driving bunch.

- The wakes are calculated considering the various vacuum chamber objects in isolation. The possible interaction between different objects, however, should in the future also be addressed.

Our present attempt at obtaining the impedance of the PEP-X vacuum chamber is still relatively crude and incomplete. As more becomes known concretely about the PEP-X vacuum chamber design, a more accurate and complete wake representing the ring will be able to be obtained.

Resistive Wall Wake

The resistive wall wakefield induced by a Gaussian bunch of length σ_z in a round metallic beam pipe of radius a, length ℓ, and conductivity σ_c is given by

$$W(s) = \frac{c\ell}{8\sqrt{2}\pi a}\frac{1}{\sigma_z^{3/2}}\sqrt{\frac{Z_0}{\sigma_c}}\, f(s/\sigma_z)\ , \tag{6.1}$$

where

$$f(x) = \sqrt{|x|^3}e^{-x^2/4}\left(I_{1/4} - I_{-3/4} \pm I_{-1/4} \mp I_{3/4}\right)\Big|_{x^2/4} \qquad x \gtrless 0\ . \tag{6.2}$$

Here c is speed of light, $Z_0 = 377\ \Omega$, and $I_n(x)$ is the modified Bessel function of the first kind of order n. In our convention $s = 0$ is the location of the center of the bunch with $s > 0$ behind the bunch center, and $W > 0$ indicates energy gain. Note that Eq. 6.1, and other equations used in this section can be found in Ref. [24].

In Table 6.1 we give the four types of beam pipes found in PEP-X, including their total length, cross-sectional shape and dimensions (a_x and a_y are the half-heights in the horizontal and vertical directions), and type of metallic coating and its conductivity. We note that only in the straights do we have round beam pipes. In the case of a non-round pipe Eq. 6.1 is modified simply by the inclusion of a multiplicative coefficient that is not equal to 1. K. Yokoya has shown that the coefficient, for both elliptical and rectangular cross-sections, differs by only a few percent from 1, if a in Eq. 6.1 is replaced by the smaller of a_x and a_y (for PEP-X this is always a_y) [25]. In our calculations we ignore this difference and let the coefficient be 1. In computing the total resistive wall wake component for PEP-X we properly weight the contribution of the beam pipe type i by the factor $\ell_i/a_{yi}\sqrt{\sigma_{ci}}$. For the resistive wall component the total loss factor (minus the weighted average of the wake) at nominal bunch length is $k_{loss} = 21.2$ V/pC.

Table 6.1: PEP-X beam pipe chamber types, giving total length, cross-sectional shape, half-height in x and y, type of metal coating, and conductivity σ_c of the coating.

Type	Total Length [m]	Shape	(a_x, a_y) [mm]	Metal	σ_c [Ω^{-1}m^{-1}]
Arcs	1417	Elliptical	(37.5, 12.5)	Al	3.5×10^7
Straights	580	Round	(48.0, 48.0)	Al	3.5×10^7
Undulators	105	Elliptical	(25.0, 3.0)	Cu	5.9×10^7
Wigglers	90	Rectangular	(22.5, 7.5)	Cu	5.9×10^7

RF Cavity Wake

The cavity beam pipe radius $a = 48$ mm; it has nose cones with a minimum gap of $g = 222$ mm (see Fig. 6.1). The computed wake, for one RF cavity at nominal bunch length, is shown in Fig. 6.11 (the blue curve). Also given is the shape of the bunch distribution λ (in yellow; the head is to the left).

For short bunches ($a/\sigma_z \gg 1$) a cavity-like structure can be well approximated by the diffraction model. Note that in our case $a/\sigma_z = 16$ is indeed large. The diffraction wake of a Gaussian bunch is given by

$$W(s) = \frac{Z_0 c}{4\pi^{3/2} a}\sqrt{\frac{g}{\sigma_z}} f(s/\sigma_z) \ , \tag{6.3}$$

with

$$f(x) = \sqrt{|x|}e^{-x^2/4}\left(I_{1/4} \mp I_{-1/4}\right)\Big|_{x^2/4} \qquad x \gtrless 0 \ . \tag{6.4}$$

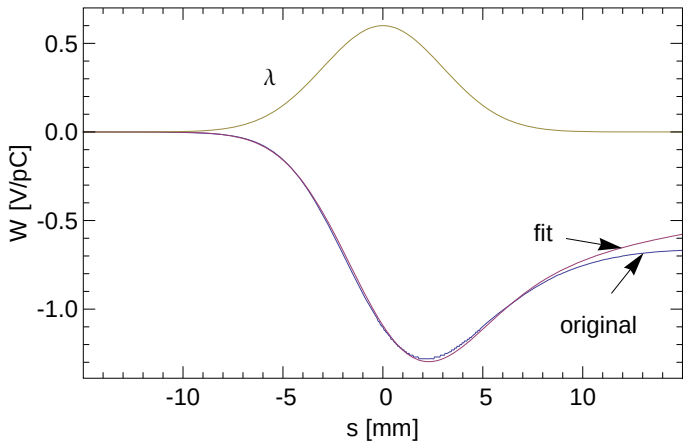

Figure 6.11: The RF cavity wake for a $\sigma_z = 3$ mm Gaussian bunch (blue), and the fit to the diffraction model (red). Also shown is the bunch shape λ (with head to the left).

If we take the minimum approach of the nose cones as the gap $g = 222$ mm, we obtain a wake that has the same shape but is 15% larger in amplitude than the numerical result. We reduce the overall scale factor by 15% and get good agreement (see Fig. 6.11); this is the function we use to represent the cavities. The loss factor at nominal bunch length, due to the cavities, is 14.7 V/pC.

Beam Position Monitors (BPMs)

The BPMs consist of four buttons that impinge on the beam pipe (see Fig. 6.2 for the general layout). Based on a recent PEP-II BPM design, the diameter of each button is chosen to be 7 mm, and there is a small groove around it to isolate it from the beam pipe. The wake of a BPM at $\sigma_z = 0.5$ mm bunch length is given in Fig. 6.12 (the blue curve). We see ringing and beating in the wake behind the bunch.

Convolving the wake by the nominal Gaussian ($\sigma_z = 3$ mm), we obtain the nominal *bunch* wake. From it we find that the loss factor at nominal bunch length is 0.014 V/pC; due to the 839 BPMs in PEP-X, it is 11.8 V/pC in total.

To estimate the inductance of wakes we fit the bunch wake (at nominal length) to that of a resistor plus inductor in series; *i.e.* to

$$W(s) = -Rc\lambda(s) - Lc^2\lambda'(s) \ , \tag{6.5}$$

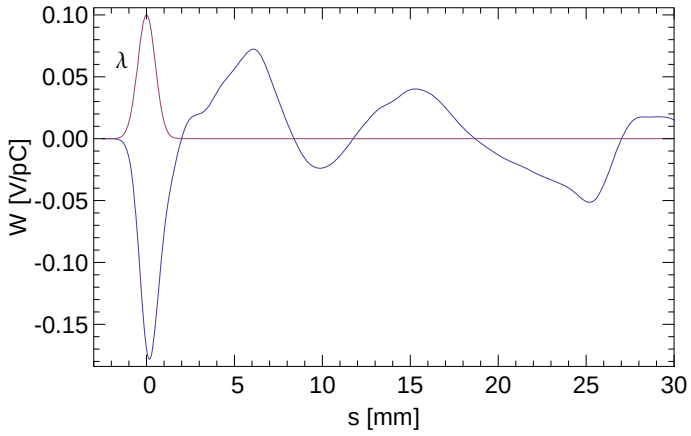

Figure 6.12: The BPM wake for a $\sigma_z = 0.5$ mm Gaussian bunch (blue). Also shown is the bunch shape λ (with head to the left).

with fit parameters R the resistance and L the inductance, and $\lambda(s)$ the longitudinal (Gaussian) charge distribution. For the PEP-X BPMs we obtain $R = 0.6\ \Omega$ and $L = 0.004$ nH for each bpm; $R = 479\ \Omega$ and $L = 3.2$ nH for the 839 bpms in the ring. 11.3 V/pC.

Undulator Tapers

Transitions are required from the elliptical undulator chambers to the elliptical arc chambers (see Table 6.1). It was decided to use tapers with an angle of 5.71° in the vertical direction (see Fig. 6.5 for a pair of such tapers). Note that the 3D wake was obtained for a pair of transitions in the configuration of a shallow cavity, with the separation of the two transitions greatly foreshortened (due to practical considerations); this will result in some inaccuracy in the wake. The computed wake, at $\sigma_z = 0.5$ mm, for a pair of undulator tapers is shown in Fig. 6.13.

For the undulator transitions at nominal bunch length we find that, for each transition pair, $k_{loss} = 0.06$ V/pC, $R = 3.\ \Omega$ and $L = 0.29$ nH; for all 30 undulator taper pairs $k_{loss} = 1.8$ V/pC, $R = 92.\ \Omega$ and $L = 8.8$ nH.

Wiggler Tapers

The damping wiggler transitions connect the wiggler chamber, with rectangular cross-section with half-heights $(a_x, a_y) = (22.5, 7.5)$ mm, to the straights, with round cross-section of radius 24 mm. The angle of transition was chosen to be 6° in the vertical direction.

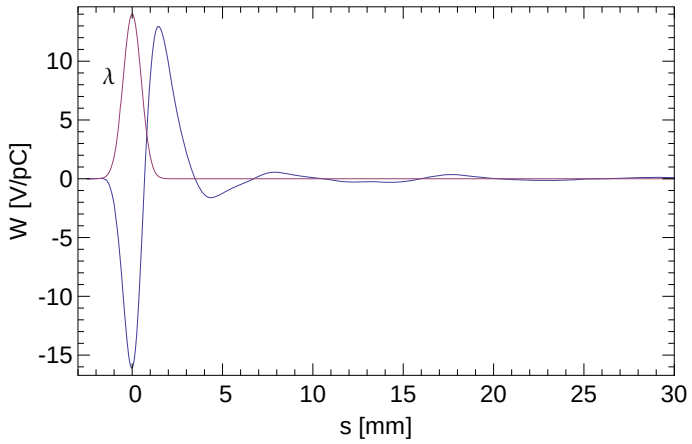

Figure 6.13: The wake for a pair of undulator transitions, for a $\sigma_z = 0.5$ mm Gaussian bunch (blue). Also shown is the bunch shape λ (with head to the left).

The $\sigma_z = 0.5$ mm wake of the 3D wiggler transitions is difficult to obtain, so for the time being we take a 2D calculation of the 2D taper that inscribes the actual 3D one to represent the wiggler transition wake. In PEP-X the wiggler tapers will be separated from one another by many meters of beam pipe, much larger than the catch-up distance $\sim a^2/2\sigma_z$, which is ~ 55 mm in the case of entering the insertion ($a = 7.5$ mm, $\sigma_z = 0.5$ mm) and is ~ 600 mm in the case of entering the large beam pipe ($a = 24$ mm). So the wake should be almost the same as for the case where the transitions are separated by infinitely long pipes, which is the case we calculate.

We numerically calculate the wake of a 2D in-taper, a 6 degree transition from a 24 mm radius pipe to a 7.5 mm pipe, and we call it $W_{in}(s)$. Then the wake of a symmetric pair of transitions is given by

$$W(s) = W_{in}(s) - \frac{Z_0 c}{2\pi} \ln(b/a)\lambda(s) \ , \tag{6.6}$$

where a and b are respectively the radius of the small and large beam pipe. The wakefield for one pair of wiggler transitions thus obtained is shown in Fig. 6.14.

For the wiggler transitions at nominal bunch length we find that, for each transition pair, $k_{loss} = 0.26$ V/pC, $R = 12.\ \Omega$, and $L = 0.74$ nH; for all 16 undulator taper pairs $k_{loss} = 4.2$ V/pC, $R = 195.\ \Omega$, and $L = 11.9$ nH.

Other Components

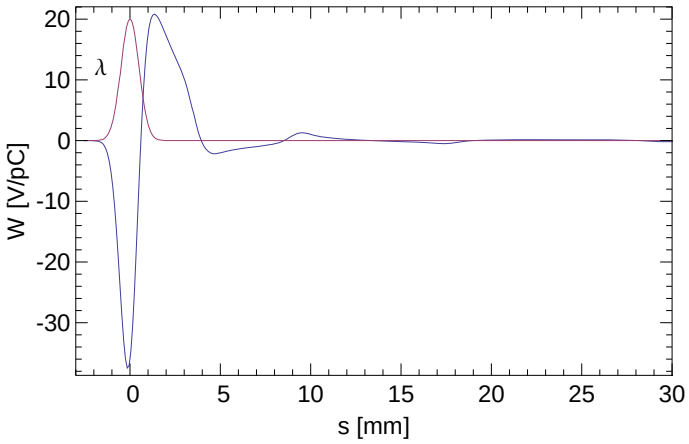

Figure 6.14: The wake for a pair of wiggler transitions, for a $\sigma_z = 0.5$ mm Gaussian bunch (blue). Also shown is the bunch shape λ (with head to the left).

We have also computed the wakes of 720 bellows slots and bellows masks. We find these objects to be very inductive to the nominal PEP-X beam: the total inductance is .3 nH and 2.7 nH, respectively, for the two types of bellows objects, and the total loss factor is nearly zero and 3.7 V/pC, respectively.

We have also computed the wakes of 2 transverse feedback kickers and 2 injection kickers. We find these objects to be very resistive to the nominal PEP-X beam: the total resistance is 9.73 Ω and 3.78 Ω, respectively, for the two types of kickers, and the total loss factor is 0.28 V/pC and 0.11 V/pC, respectively.

6.1.3 PEP-X Ring Wake and Impedance Budget

In Fig. 6.15 we present the total wake contributions (at $\sigma_z = 0.5$ mm) of the different types of impedance objects—resistive wall, wiggler transitions, undulator transitions, BPMs, and RF cavities—in the PEP-X ring. We see that the dominant contributors at this bunch length are the resistive wall wake and the undulator and wiggler transitions. These wakes when summed and added to the small contributions of the bellows slots and masks give the pseudo-Green function wake that we use in the simulations, to be presented in the microwave instability calculations given in the following section.

In Table 6.2 we give the impedance budget at nominal bunch length ($\sigma_z =$ 3 mm), showing the loss factor k_{loss} (obtained from the original computed wakes) and the R and L parameters, when Eq. 6.5 is fit to the wakes, for

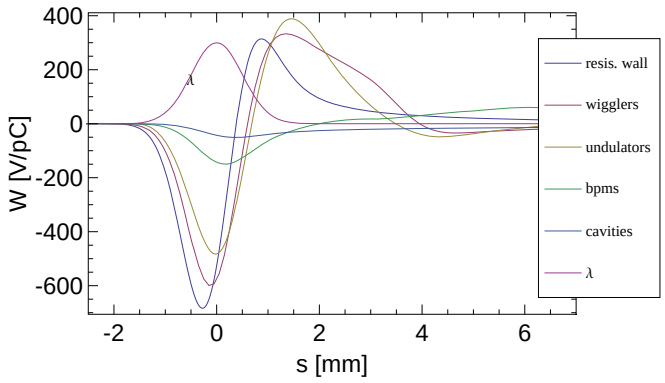

Figure 6.15: The important contributors to the PEP-X wake at $\sigma_z = 0.5$ mm: the resistive wall, the wiggler tapers, the undulator tapers, the BPM's and the RF cavities. The wakes are weighted by the number of these objects that are found in PEP-X. Also shown is the bunch shape λ (with head to the left).

all the vacuum chamber objects considered. Note that, for the RF cavities, the fitted L has no physical meaning; in reality such cavities have a resistive and *capacitive* character at PEP-X–type bunch lengths. The total loss factor for PEP-X is 57.5 V/pC; for the fits the total $R = 2.3$ kΩ and the total $L = 38.2$ nH. Although our models are somewhat crude, this table gives an indication of the relative contributions to the real and imaginary parts of the impedance of the various objects in the PEP-X vacuum chamber.

Table 6.2: Impedance budget for PEP-X. Given are the object name, the loss factor k_{loss}, the effective (fitted) resistance R and inductance L of each object; the object count N_{obj} and the contribution to the total k_{loss}, R, and L in the ring. Impedance values given were calculated at the nominal bunch length, $\sigma_z = 3$ mm.

Object	**Single Contribution**			**Total Contribution**			
	k_{loss}[V/pC]	R [Ω]	L [nH]	N_{obj}	k_{loss}[V/pC]	R [Ω]	L [nH]
RF cavity	.92	30.4	–	16	14.7	487	–
Undulator taper (pair)	.06	3.0	.29	30	1.8	92	8.8
Wiggler taper (pair)	.26	12.0	.74	16	4.2	195	11.9
BPMs	.014	.6	.004	839	11.8	479	3.2
Bellows slots	.00	.0	4e-4	720	.0	.0	.3
Bellows masks	.005	.2	.004	720	3.7	142	2.7
Resistive wall wake					21.3	880	11.3
Total					57.5	2275	38.2

6.2 Longitudinal Narrow-Band Impedance

RF cavity

The properties of the longitudinal modes of the rf cavity including damping effects of the HOM couplers have been measured [26]. Table 6.3 lists the measured mode frequency, R/Q and the loaded Q for a single PEP-II cavity. For coupled bunch instability studies, one needs to multiply the R/Q by the number of cavities (16) used for PEP-X.

BPM

The longitudinal wakefield of the BPM has a long tail of oscillations at large distances, indicating the existence of trapped modes in the buttons. The impedance spectrum is shown in Fig. 6.16. Two prominent peaks in the relevant frequency range can be seen. The field pattern of the resonant mode at around 11.65 GHz is shown in Fig. 6.17.

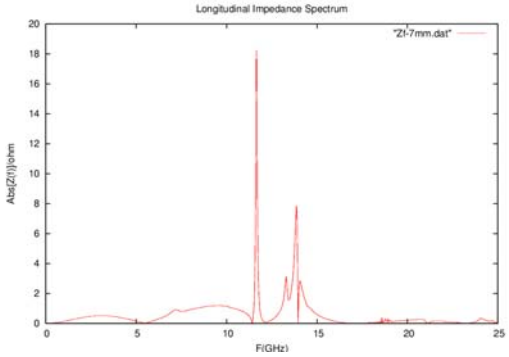

Figure 6.16: Longitudinal impedance spectrum of BPM.

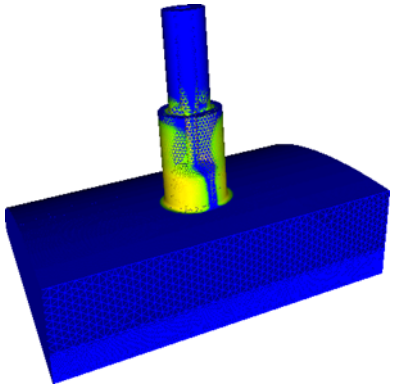

Figure 6.17: A trapped mode in BPM.

6.3 Transverse Narrow-Band Impedance

RF cavity

The properties of the transverse modes of the rf cavity including damping effects of the HOM couplers have been measured [26]. Table 6.3 lists the measured mode frequency, R/Q (at 4 cm offset) and the loaded Q for a single PEP-II cavity. For coupled bunch instability studies, one needs to multiply the R/Q by the number of cavities (16) used for PEP-X.

Frequency (GHz)	R/Q (Ω)	Q
0.475	117.3	14218
0.768	44.6	18
1.009	0.43	128
1.283	6.70	259
1.295	10.3	222
1.595	2.43	300
1.710	0.44	320
1.820	0.13	543
1.898	0.17	2588
2.121	1.82	338
2.160	0.053	119
2.265	0.064	1975

Table 6.3: Impedance of measured longitudinal modes of PEP-II RF cavity.

Frequency (GHz)	R/Q@4 cm (Ω)	Q
0.792 (V)	9.96	115
1.063 (V)	50.4	27
1.133 (V)	1.29	54
1.202 (V)	0.56	871
1.205 (H)	0.90	723
1.346 (H)	3.96	323
1.327 (V)	5.58	611
1.420 (V)	5.31	1138
1.425 (H)	3.30	414
1.540 (H)	1.57	73
1.542 (V)	0.50	92
1.595 (V)	0.51	145
1.599 (H)	0.29	146
1.670 (H)	3.61	377
1.676 (V)	4.63	783
1.749 (V)	0.10	1317
1.756 (H)	0.12	2664

Table 6.4: Impedance of measured transverse modes of PEP-II RF cavity. (V) and (H) indicate mode polarizations in the vertical and horizontal directions, respectively.

Chapter 7

Collective Effects

Our analysis of beam instabilities is based on the wakefields computed in Chapter 6. In the following we will focus on three subjects: microwave instability, coherent synchrotron radiation (CSR) wakefield, and multibunch transverse instability due to the resistive wall impedance.

In the calculations that follow we use the parameters of the ring from Table 7.1.

Circumference C, (m)	2199.32
Average current I, (A)	1.5
Number of bunches, n_b	3154
Peak current $\hat{I}_b$, (A)	140
Nominal bunch current I_b, (mA)	0.476
ν_x	87.23
ν_y	36.14
ν_s	0.0077
α	5.81×10^{-5}
σ_z, (mm)	3.0
σ_p	1.14×10^{-3}
Damp. time, long. τ_s, (ms)	10.8
Average β function β_y, (m)	9.7
Revolution period T_0, (μs)	7.33
RF voltage V_{RF}, (MV)	8.9
Energy loss U_0, (MV)	3.12

Table 7.1: Parameters used in calculations and simulations.

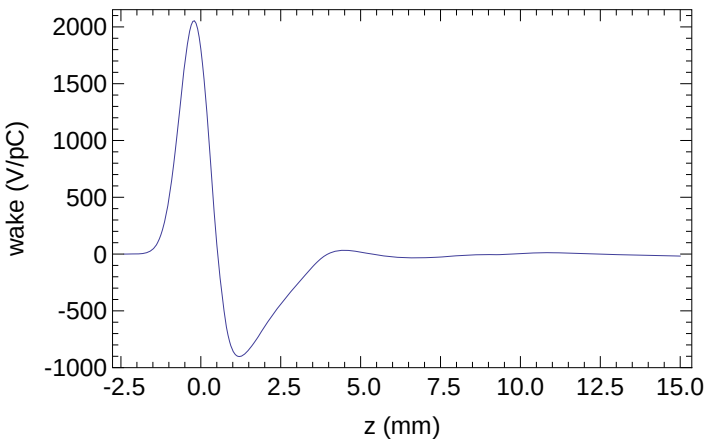

Figure 7.1: Longitudinal wakefield for a 0.5 mm bunch. Positive values of the wake correspond to energy loss, and positive values of the coordinate z is behind the source particle.

7.1 Microwave Instability

For analysis of the microwave instability we used a longitudinal pseudo-Green function computed in Chapter 6 which includes contributions from the resistive wall, BPMs, RF cavity, undulator and wiggler tapers, bellows, masks, slots and the kickers. This function is shown in Fig. 7.1. It corresponds to the wakefield of a bunch with rms length of 0.5 mm.

As a first step in stability analysis, one usually solves the Haissinski equation and finds an equilibrium longitudinal distribution of the bunch modified by the wake. An example of such a solution, for the nominal total beam current of 1.5 A, is shown in Fig. 7.2. One can see a distortion of the bunch shape and an increased rms bunch length from the nominal 3 mm (at zero current) to about 3.8 mm.

Two different simulation techniques were employed to study the microwave instability. In the first one we used a linearized Vlasov solver which computes the growth rate of the instability for a given wake and parameters of the beam. In the second one we used a Vlasov-Fokker-Planck (VFP) solver [27] to simulate longitudinal beam dynamics. The solver not only finds the threshold of the instability, but also simulates evolution of the beam dynamics above the instability threshold.

The result of the analysis with the linearized solver is shown in Fig. 7.3. It shows the computed growth rate as a function of the beam current in

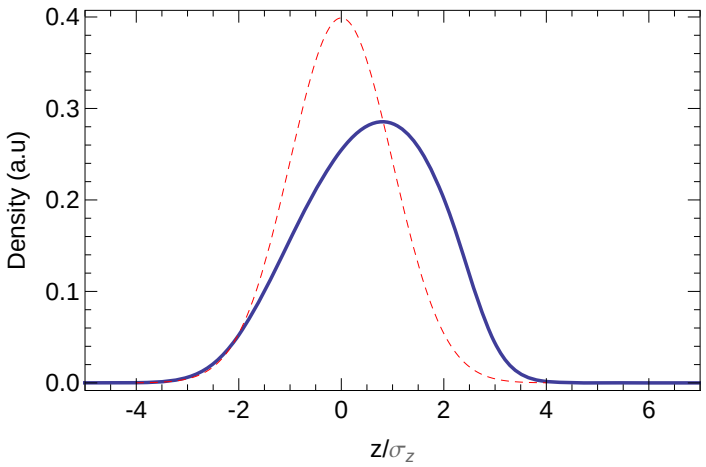

Figure 7.2: Longitudinal beam density distribution obtained from solution of the Haissinski equation. The red dashed line shows the distribution without the wakefield effects (at zero current), and the solid blue line shows the distribution with account of the wake (for the nominal beam current). The head of the bunch is at positive values of z.

the range 6 A $< I <$ 7 A, which indicates a threshold of the instability at about $I \approx 6.3$ A. The horizontal line shows the level of the damping rate (corresponding to the damping time of 10 ms) due to the synchrotron damping of the synchrotron oscillations.

This result was corroborated in simulations performed with the VFP solver shown in Fig. 7.4. It demonstrates a stable equilibrium at 6 A, and a relatively mild instability at the beam current of 7 A. Note that the instability results in sawtooth oscillations of the beam length with amplitude of about a fraction of one percent.

As we see from the simulations, for the currently computed longitudinal wakefield, the threshold of the microwave instability considerably exceeds the nominal beam current in the PEP-X.

7.2 CSR Wakefield

We also calculated the contribution to the longitudinal bunch wakefield of the coherent synchrotron radiation in the bending magnets of the ring. The baseline lattice has 200 bend magnets of three types with parameters presented in Table 7.2. The total length of the bending magnets in the TME cells is 466.2 m, and the length of the bending magnets in the DBA cells is

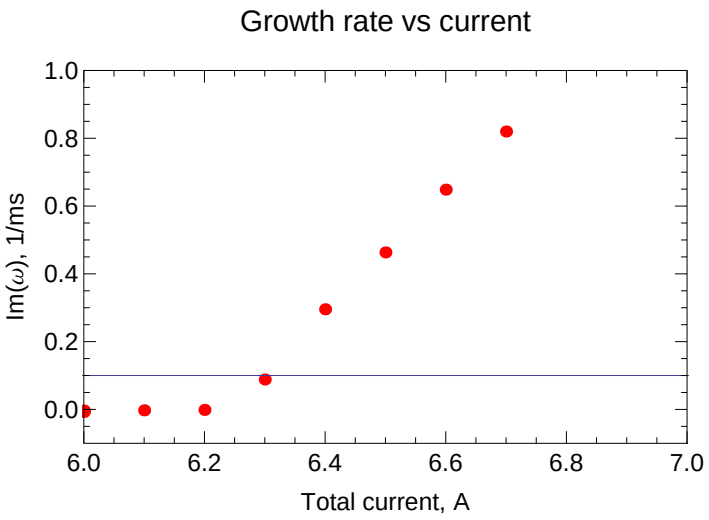

Figure 7.3: The growth rate of the microwave instability as a function of a total beam current in the ring.

	TME Bend	TME disp. Bend	DBA Bend
Field, (kG)	1.35	1.35	3.78
Length, (m)	3.5	2.28	1.3
Bending radius, (m)	111.3	111.3	39.7
Number	128	8	64

Table 7.2: Types of bend magnets in the ring

83.2 m.

The cross sections of the vacuum chamber in the bends is shown in Fig. 7.5. It basically has an elliptical shape, with dimensions shown in Fig. 7.5. Unfortunately, there is no theory available that allows to compute the CSR wakefield for a vacuum chamber with elliptical cross section. We used a recently developed theory [28] of the CSR impedance for a vacuum chamber of rectangular cross section and replaced the elliptical geometry shown in Fig. 7.5 with a rectangular one, with the horizontal size of 75 mm, and the vertical one of 25 mm. The theory of Ref. [28] also includes into consideration the transients effects of formation of the wake at the entrance to the magnet, as well as transients due to the exit into a long straight pipe. The CSR wakefield was computed for each type of magnet from Table 7.2 and added with account of the total number of magnets of each type. The computed CSR wakefield for a rms bunch length of 0.5 mm is shown in Fig. 7.6. For comparison, Fig. 7.6 also shows the wakefield com-

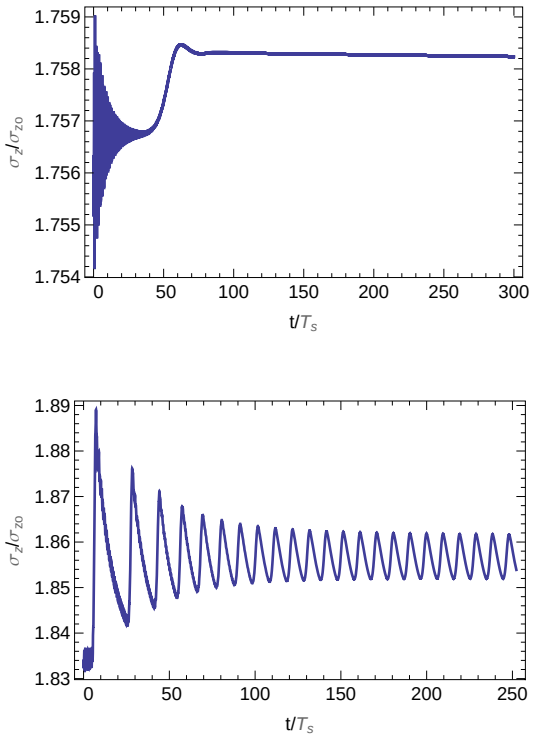

Figure 7.4: Evolution of the rms longitudinal size of the beam σ_z versus time for the beam current of 6 A (top) and 7 A (bottom).

puted for the parallel-plates model—an approximation often used in studies of shielded CSR effects. One can see a relatively small difference between the parallel-plates and the rectangular cross section results. This is a somewhat expected result, because a rectangle with an aspect ratio of 3 (75 mm over 25 mm) turns out to be a good approximation of an infinite aspect ratio, corresponding to the model of parallel plates.

Comparing this wake with the wake of all other elements in the ring shown in Fig. 7.1, one notices that the contribution of the CSR wakefield is relatively small. Based on the relative smallness of the CSR wakefield,

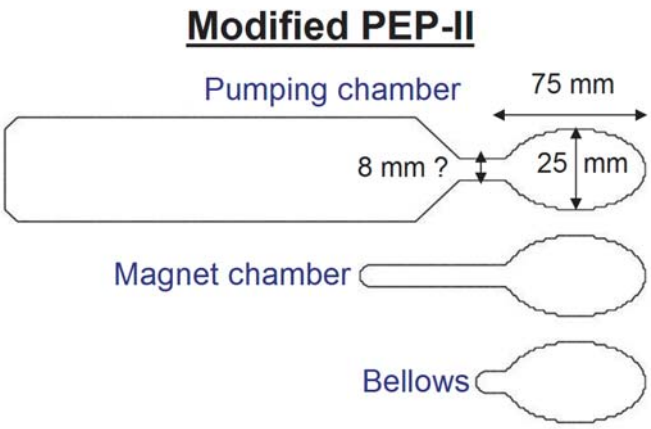

Figure 7.5: Cross sections of the vacuum chamber in the dipole magnets.

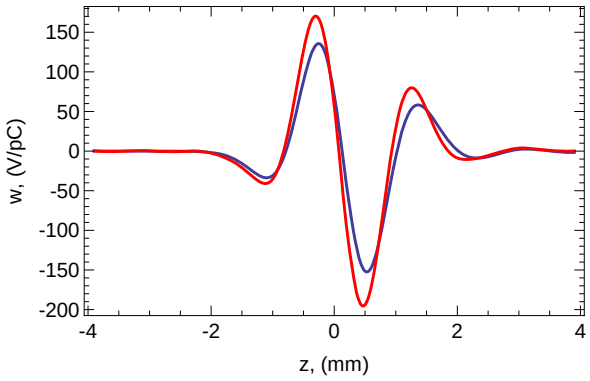

Figure 7.6: The CSR wakefield computed for rectangular vacuum chamber (blue line) and in the model of parallel plates (red line). Positive z correspond to the tail, positive wake gives the energy loss.

as well as the high threshold of the microwave instability discussed in the previous section, we conclude that the effect of the CSR wakefield is small.

7.3 Transverse Single Bunch Instability

We begin this section by noting that there were no signs of the transverse single bunch instability in the PEP-II accelerator. However, the impedance of PEP-X is significantly increased in comparison with that of PEP-II, due to the small-aperture insertion devices and transition sections. This makes it possible that the transverse mode coupling instability (TMCI) becomes an important issue in the design of the machine. In this section we consider the TMCI caused by the resistive wall impedance in the ring.

The resistive wall impedance is dominant in most of the light sources which have regions with small aperture of the vacuum chamber. The standard transverse impedance of a round pipe of length ℓ is given by [29]

$$Z_\perp(\omega) = (\mathrm{sgn}(\omega) - i)\,\frac{\ell Z_0}{2\pi b^3}\sqrt{\frac{2c}{Z_0\sigma}}\frac{1}{\sqrt{|\omega_c|}}. \tag{7.1}$$

Here $Z_0 = 377$ Ohm is the impedance of free space, b is the radius of the beam pipe, σ_c is the conductivity of the pipe material and c is the speed of light. A more realistic model of the shape of the vacuum chamber will be studied in the future. The wake function corresponding to Eq. (7.1) is

$$W_\perp(s) = \frac{c\ell}{\pi b^3}\sqrt{\frac{Z_0}{\pi\sigma_c}}\frac{1}{\sqrt{s}}, \qquad (s \geq 0). \tag{7.2}$$

We used parameters from Table 6.1 for the beam pipe dimensions, material and the length in different sections of the ring. An approximation of elliptical shape was used for the wiggler section. The impedance in the 105 meters insertion section is dominant due to its small aperture. The impedances from the arc and straight sections are negligible. Therefore, replacement of the beam pipe in arc and straight sections with copper doesn't effectively reduce the total impedance.

The resistive wall wakefield for the ring computed using parameters from Table 6.1 is shown in Fig. 7.7, where in order to eliminate the singularity at the origin, the wake was convoluted with a 0.5 mm rms length Gaussian bunch.

Three different approaches have been used in this report to study the threshold of the TMCI.

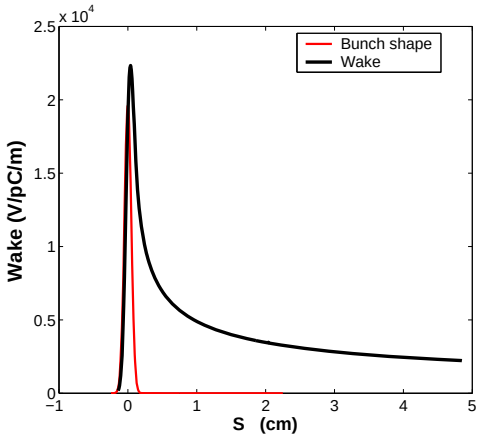

Figure 7.7: Transverse resistive wall wake convoluted with 0.5 mm Gaussian bunch.

Mode Coupling Theory. TMCI occurs when the frequencies of two neighboring head-tail modes approach each other due to the detuning with increasing beam current. For Gaussian bunches, the threshold of the instability can be related to the transverse loss factor $\kappa_\perp$ [30] by

$$I_b^{th} = \frac{2\omega_s E/e}{\sum_j \beta_{\perp,j} k_{\perp,j}} \Theta, \tag{7.3}$$

where I_b^{th} is the threshold of the bunch current, ν_s is the synchrotron tune, $\beta_{\perp,j}$is the average beta function in the jth element, and E is the beam energy and $\Theta \approx 0.7$.

Eigen-value Solver. The threshold of transverse mode coupling instability can be found by solving the following eigen-value problem [29, 31]

$$\left(\frac{\Omega - \omega_\beta}{\omega_s}\right) a_{lk} = \sum_{l',k'} M_{lk,l'k'} a_{l'k'}. \tag{7.4}$$

For the lowest radial mode ($k, k' = 0$), which we only consider here, denoting $M_{l0,l'0} = M_{ll'}$ we have

$$M_{ll'} = l\delta_{ll'} - i\frac{I_b\langle\beta_\perp\rangle}{Z_0 I_A \gamma \omega_s} i^{l-l'} \frac{1}{\sqrt{l!l'!}} \int_{-\infty}^{+\infty} d\omega Z_\perp(\omega) \left(\frac{\omega\sigma_z}{\sqrt{2}c}\right)^{l+l'} \exp\left(-\frac{\omega^2\sigma_z^2}{c^2}\right), \tag{7.5}$$

here $\langle\beta_\perp\rangle$ is the average beta function in the region where the transverse impedance is important, I_b is bunch current and $I_A = 17$ kA is the Alfven

current. The tune of each mode $(\Omega-\omega_\beta)/\omega_s$ is obtained by solving the eigen-value problem for matrix M. The frequency $\Omega = \omega_\beta \pm l\omega_s$ corresponds to the $\pm l$-th synchrotron sideband. The threshold can be found when the head-tail modes corresponding to different values of l merge.

Particle tracking. Computer simulation programs have been used for more precise calculation of the threshold. The bunch was represented by a number of macro-particles. The threshold of instability was found by tracking with different bunch currents.

The transverse loss factor corresponding to the wake shown in Fig. 7.7 is $k_\perp^{th} = 1.5 \times 10^3$ V/pC/m. Eq. 7.3, for this value of the loss factor, gives the threshold bunch current $I_b^{th} \cong 0.67$ mA, larger than the nominal current in the ring.

The result of calculations using the eigen-value solver method is shown in Fig. 7.8. This calculation gives for the threshold current $I_b^{th} \cong 0.72$ mA.

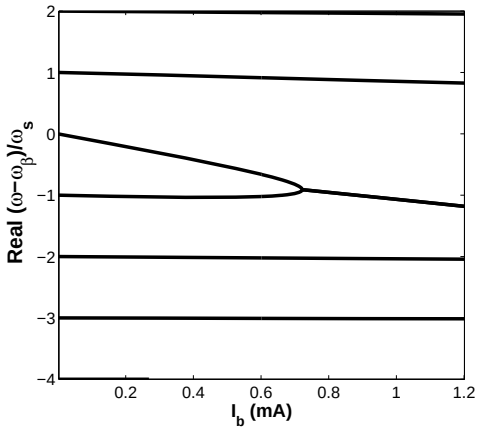

Figure 7.8: TMCI in PEP-X due to the resistive wall impedance

Finally, Fig. 7.9 shows the result of particle tracking. Oscillations of the bunch centroid for different bunch currents are plotted as a function of time. It clearly shows that the bunch becomes unstable at approximately 0.8 mA.

The three approaches show reasonable agreement. The nominal bunch current of PEP-X is 0.48 mA, which is below the threshold of the TMCI instability. We emphasize here again that only the resistive wall impedance is considered here, and the final conclusion about the beam stability should be made when the transverse impedance for other elements in the ring is available.

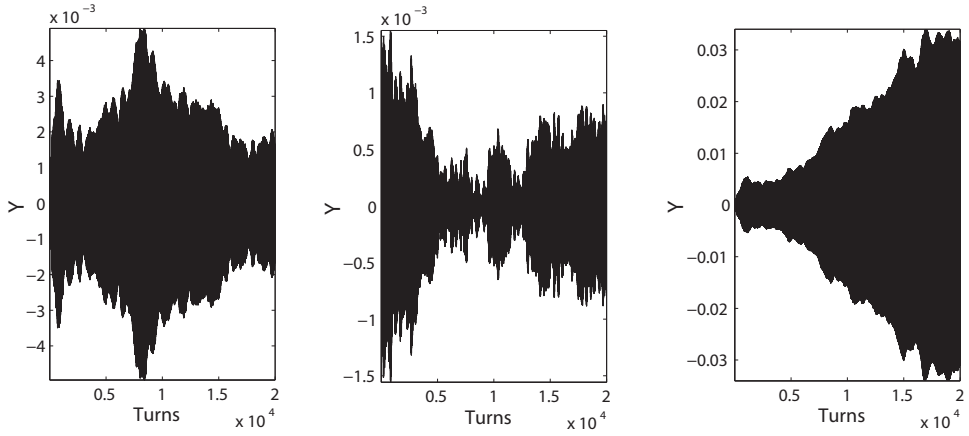

Figure 7.9: Simulated dipole oscillations in vertical plane for different bunch currents: (left) 0.78 mA; (middle) 0.79 mA and (right) 0.80 mA

7.4 Multibunch Transverse Instability

For calculation of the growth rate for the transverse multibunch instability we use the following result from [29] for the frequency shift induced by the long range wakefields:

$$\Delta\omega(l) = -i\frac{2\pi M N_b r_e}{Z_0 \gamma T_0^2 \omega_\beta} \sum_{p=-\infty}^{\infty} Z_\perp[\omega_\beta + (pM + l)\omega_0]\,, \tag{7.6}$$

where $Z_\perp(\omega)$ is the transverse impedance, M is the number of bunches in the ring, N_b is the number of particles in the bunch, r_e is the electron classical radius, γ is the relativistic factor, T_0 is the revolution period in the ring, l is an integer number of the mode, and ω_β is the betatron frequency. The formula assumes a uniform distribution of bunches in the ring and treats bunches as point charges with the charge equal to $N_b e$.

We can carry out the summation analytically, if we use wakefields instead of impedances. In terms of wakefield, Eq. (7.6) can be written as follows

$$\Delta\omega(l) = \frac{2\pi N_b r_e}{Z_0 \gamma T_0 \omega_\beta} \sum_{n=1}^{\infty} w_\perp(n s_b) e^{2\pi i (l+\nu_\beta) n/N_b}\,. \tag{7.7}$$

For the resistive wall the transverse wake decays with distance as $w_\perp = Az^{-1/2}$ and the sum can be computed analytically in terms of the polyloga-

rithm function $\mathrm{Li}_{\frac{1}{2}}(x)$: $\mathrm{Li}_k(x) = \sum_{n=1}^{\infty}(x^n/n^k)$, so that

$$\Delta\omega(l) = \frac{2\pi N_b r_e}{Z_0\gamma T_0\omega_\beta} w_\perp(s_b)\mathrm{Li}_{\frac{1}{2}}(e^{2\pi i(l+\nu_\beta)/M})\,. \tag{7.8}$$

The function $\mathrm{Li}_{\frac{1}{2}}(e^{2\pi ix})$ is a periodic function with the period equal to 1. It's imaginary part diverges, $\mathrm{Li}_{\frac{1}{2}}(e^{2\pi ix}) \to +\infty$, when $x \to +0$, which means that the maximum growth rate is attained for the minimal value of the argument $(l+\nu_\beta)/M$. This value is equal to $-(1-[\nu_\beta])/M$ where $[\nu_\beta]$ is the fractional part of the tune. For small negative values of the argument x, the function $\mathrm{Li}_{\frac{1}{2}}(e^{2\pi ix})$ can be approximated by $(1-i)/2\sqrt{-x}$ which gives the following equation for the approximate value of the growth rate of the instability

$$\mathrm{Im}\Delta\omega(l) = \frac{\pi N r_e c}{Z_0\gamma T_0\omega_\beta} w_\perp(s_b)\sqrt{\frac{M}{1-[\nu_\beta]}}\,. \tag{7.9}$$

Applying this formula for the transverse resistive wall wake we will use the following expression for the transverse resistive wall wake

$$w_\perp(z) = \frac{A}{\sqrt{z}}\,. \tag{7.10}$$

Using this expression for the wake and taking into account that $s_b = C/M$, we can rewrite Eq. (7.9) for the growth rate of the instability as follows

$$\mathrm{Im}\Delta\omega = \frac{Ac^2(I/I_\mathrm{A})}{4\gamma\omega_\beta\sqrt{C(1-[\nu_\beta])}}\,. \tag{7.11}$$

The above derivation assumes a constant beta function in the ring. A more accurate analysis that takes into account variation of the beta function shows that the quantity A in Eq. (7.11) should be replaced by its averaged value $\langle\beta A\rangle$ weighted with the local value of the beta function [32]:

$$\mathrm{Im}\Delta\omega = \frac{c(I/I_\mathrm{A})}{4\gamma\sqrt{C(1-[\nu_\beta])}}\langle\beta A\rangle, \tag{7.12}$$

where

$$\langle\beta A\rangle = \frac{c}{\pi}\sqrt{\frac{Z_0}{\pi}}\sum_i \frac{\ell_i\beta_i}{b_i^3\sqrt{\sigma_{ci}}}\,, \tag{7.13}$$

the subscript i indicates various regions of the ring (arcs, straights, insertions,

and the wiggler), ℓ_i is the length of the region i, b_i is the pipe radius, and σ_{ci} is the wall conductivity of the vacuum chamber in region i.

Using parameters from Table 6.1 and the lattice of the ring we calculated $\langle \beta A \rangle = 3769$ V$\sqrt{\text{m}}$/(pC), and the growth rate of the instability to be 0.14 ms (corresponding to approximately 19 revolutions).

7.5 Fast Ion Instability

Ions generated by beam-gas ionization can be trapped by the electron bunches. The ion-cloud can cause beam instability, emittance blow-up, and tune shift. The ion induced beam instability is a critical issue for PEP-X due to its ultra small emittance.

The exponential growth rate of fast ion instability (FII) is given by [33]

$$\frac{1}{\tau_{c,y}} = \frac{c r_e \beta_y N_b n_b}{2} \frac{\hat{W}}{\gamma}. \tag{7.14}$$

where $\hat{W}$ is the coupling force between the electron-bunches and ions,

$$\hat{W} = \frac{8\sigma_i P}{3\sqrt{3}kT} \left(\frac{r_p}{A}\right)^{1/2} \frac{(N_b s_b)^{1/2} n_b}{\sigma_y^{3/2}(\sigma_y + \sigma_x)^{3/2}}. \tag{7.15}$$

P is the pressure, σ_i is the ionization cross-section, A is the mass number of ions, r_p is the classical radius of proton, k is Boltzmann's constant, T is the temperature, n_b is the number of bunches, N_b is number of electrons per bunch, $\sigma_{x,y}$ is the transverse beam size, and s_b is the bunch spacing. The coupling force in PEP-X is about three orders of magnitude larger than that in the B-factories due to its small emittance.

On the other hand, the ultra small beam size can mitigate the instability by driving the ion unstable and providing more effective Landau damping. Without gaps in the beam fill pattern, the ions with a relative molecular mass greater than $A_{x,y}$ will be trapped horizontally (vertically), where

$$A_{x,y} = \frac{N_b r_p s_b}{3(\sigma_x + \sigma_y)\sigma_{x,y}}. \tag{7.16}$$

If the beam size is small enough, the strong beam's force can over focus the ions and cause the ion's motion to be unstable. Fig. 7.10 shows the critical mass number $A_{x,y}$ along the circumference of the ring (only a fraction of the ring is shown) for 5% beam coupling. The H_2^+, CH_4^+, H_2O^+ are unstable in most of the regions and CO^+/N_2^+ ions are unstable at partial regions as shown in the figure. According to Eq. (7.16), there are less number of ions

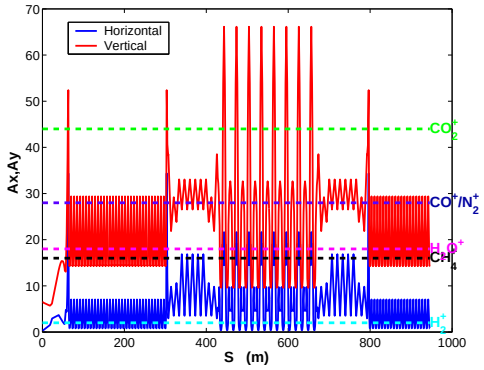

Figure 7.10: Critical mass number along the ring. The mass number of H_2, CH_4, H_2O, CO and CO2 is marked in the plot.

trapped with a smaller coupling.

One important damping mechanism is the ion oscillation frequency spread $\Delta\omega_i$ along the ring due to the variation of the beam size [34]

$$\frac{1}{\tau_e} \approx \frac{1}{\tau_c} \frac{c}{2\sqrt{2} n_b s_b \Delta\omega_i}. \tag{7.17}$$

The oscillation frequency of the trapped ions is given by

$$\omega_{i,x(y)} = \left(\frac{4 N_b r_p c^2}{3 A s_b (\sigma_x + \sigma_y) \sigma_{x,y}} \right)^{1/2}. \tag{7.18}$$

The large frequency spread provides a significant Landau damping of the beam instability. The DBA sections have a larger spread than the TME sections.

A gap between bunch trains can be added to suppress the ion trapping. Our study shows that the ion density exponentially decays in a train gap. With a multi-train beam filling pattern, the ion density can be reduce by a factor of F_{train} [35]

$$F_{\text{train}} = \frac{1}{N_{\text{train}}} \frac{1}{1 - \exp\left(-\tau_{\text{gap}}/\tau_{\text{ions}}\right)}. \tag{7.19}$$

Here, τ_{ions} is the diffusion time of the ion-cloud, which is close to the ion oscillation period, τ_{gap} is the length of bunch train gaps and N_{train} is the number of bunch trains.

The beam instability is simulated with a strong-weak code. Each bunch is represented by one macro-bunch, but the ions are represented by many macro-particles. The electron bunches interact with the ions at each element

when they are passing by. Therefore, the effects of trapping condition, train gap and the Landau damping are all included in the simulation. The assumed residual gas molecular species in the vacuum chamber are shown in Table 7.3. We assume a constant pressure of 1 nTorr along the whole ring. For a beam filling pattern with 19 bunch trains, each train consisting of 166 bunches, and the total number of bunches 3154, the vertical growth time is 34 μs for 5% coupling as shown in Fig. 7.11. Different beam filling patterns have been investigated. Simulations give a growth time of 42 μs for a 30 bunch-train filling pattern.

	Cross section (Mbarn)	Mass number	Percentage
H_2	0.35	2	75%
CO	2.0	28	14%
CO_2	2.92	44	7%
CH_4	2.1	16	4%

Table 7.3: Parameters of the main molecular species in the vacuum.

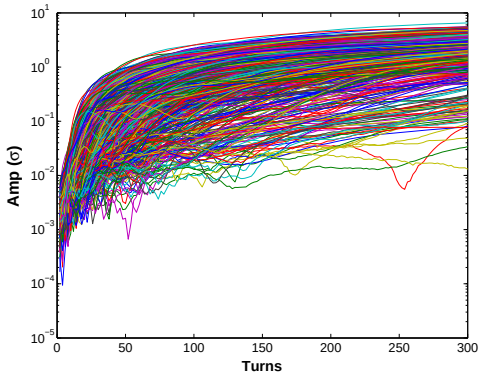

Figure 7.11: Simulated vertical amplitude of all bunches as a function of time. The beam consists of 19 bunch-trains. The amplitude is normalized by the beam size.

The feedback time of the present PEP-II feedback system is about 500 μs. The FII growth time (of order of 50 μs) is ten times faster than the feedback. A better vacuum ($P \leq 0.1$ nTorr) and a larger number of bunch trains is required for a 500 μs of FII growth time. For instance, with a pressure of 0.1 nTorr (and other parameters kept the same as in Fig. 7.11), the growth time is 250 μs. Another mitigation is to use a larger ion-cleaning gap by reducing the total number of bunches. For instance, the growth time increases to 260 μs with 183 bunch-trains (total gap 20%) and 1 nTorr pressure. The feedback also can be faster.

Chapter 8

Partial Lasing

In this section, we discuss the partial lasing possibility when a long undulator ($\sim$ 100 m) is integrated in one of the straight sections of PEP-X. Preliminary studies [36] show that for an ultra-low emittance, high peak current storage ring such as PEP-X, FEL exponential gain (without saturation) at soft x-ray wavelengths can occur on a turn-by-turn basis, with only a very modest degradation in beam energy spread.

As a numerical example, we discuss a soft x-ray FEL at $\lambda_r = 3.3$ nm using $\lambda_u = 5$ cm and $\bar{\beta} = 4$ m (see Table 8.1). The single bunch peak current from the instability chapter is estimated to be 150 A. We assume that the lattice can be adjusted slightly to accommodate a more aggressive peak current of 300 A. The total charge stored per bunch (with 3 mm rms bunch length) is 7.5 nC. More studies on the microbunching instability driven by CSR with realistic vacuum chamber geometry are necessary to determine the threshold current more accurately. Based on the numerical solutions of Ref. [36], we calculate the equilibrium energy spread and the radiation power as a function of the planned undulator length (see Fig. 8.1). For an undulator length less than 50 m, the FEL interaction induces negligible energy spread, and the FEL power grows exponentially with undulator distance. For a longer undulator, the equilibrium energy spread starts to increase to 1.26×10^{-3} in a 100-m long undulator. The increased equilibrium energy spread lengthens the bunch slightly and reduces the peak current from 300 A to 270 A. At equilibrium, the FEL peak power in the fundamental mode is about 200 kW. As the SASE pulse length is comparable to the electron bunch length (rms $\sim$ 10 ps), the average FEL power is about 0.7 W for a single electron bunch circulating in the ring (with about 1 mA average current).

To confirm these calculations, we performed a GENESIS simulation with $\hat{I}_e = 270$ A and $\sigma_{\delta e} = 1.26 \times 10^{-3}$. Figure 8.2 shows that the SASE power reaches 500 kW at 100 m, which includes contributions from the fundamental mode and higher-order transverse modes. Thus, the radiation at this stage of

Table 8.1: Parameters for a soft x-ray FEL using PEP-X.

Description	Value
Longitudinal damping time τ_s (with wigglers)	10.8 msec
normalized transverse emittance after IBS $\gamma\varepsilon_{x,y}$	0.6 μm
peak current $\hat{I}_e$ (at equilibrium)	270 A
rms energy spread $\sigma_{\delta e}$ (at equilibrium)	1.26×10^{-3}
undulator period λ_u	5 cm
undulator parameter	4.3
peak magnetic field	0.92 T
average beta in undulator $\bar{\beta}$	4 m
active undulator length z	100 m
FEL wavelength λ_r	3.3 nm
FEL peak power (at equilibrium)	$\sim$ 200 kW
RMS pulse duration	$\sim$ 10 ps
repetition rate (single bunch)	136 kHz
FEL average power (single bunch)	$\sim$ 0.7 W

the exponential growth has not reached full transverse coherence. If needed, a monochromator can be used to select the fundamental mode just like the selection of the centrol cone radiation in a spontaneous source. This mode will be transversely coherent as the beam emittance is smaller than $\lambda_r/(4\pi)$ and should have a power level of about 200 kW. The spontaneous radiation power of a 100 m undulator in a 0.1% bandwidth is estimated to be 1 kW. Thus, the FEL gain is about a factor of 200 higher than the spontaneous level. We also performed a seeded FEL simulation at this wavelength and confirmed a gain factor of 200 for a well-defined transverse mode (see Fig. 8.2). With a stored average current of about 1.5 A (about 1500 bunches in the ring), the average brightness will be enhanced by the same gain factor in the soft x-ray regime, from $\sim 10^{22}$ to $\sim 10^{24}$ photons/sec/(mm)^2/(mrad)^2 in 0.1% BW, or about 10^{19} photons/sec within the FEL bandwidth ($\sim 3 \times 10^{-3}$). Figure 8.3 shows the instantaneous power at $z = 100$ m for a small section (about 1%) of the entire SASE pulse. There are more than 1000 temporal modes (spikes) in this pulse, so the statistical fluctuation of the radiated energy is less than 3% for a single bunch, and less than 0.1% when averaged over 1500 bunches.

8.1 Discussion

We note that placing a long undulator in PEP-X may have other beam dynamics consequences that can affect the ring operation. For instance, with

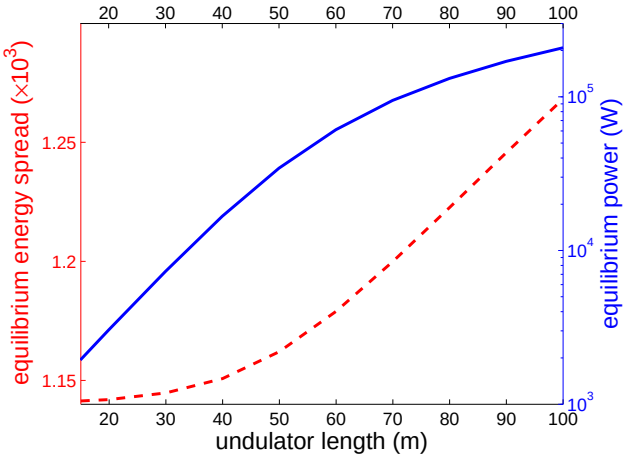

Figure 8.1: Equilibrium energy spread (red dashed curve) and FEL power at $\lambda_r = 3.3$ nm (blue solid curve) as a function of the undulator length.

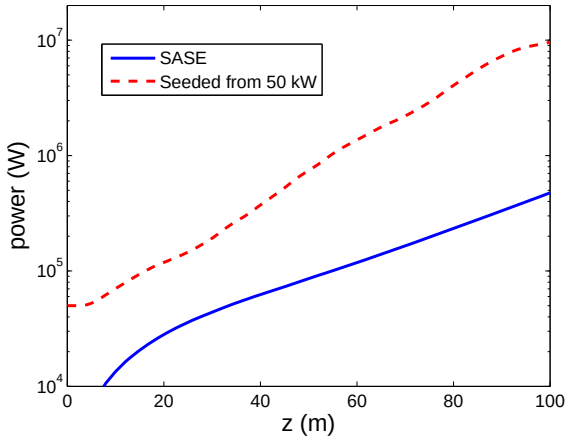

Figure 8.2: Power evolution for a soft x-ray SASE FEL at $\lambda_r = 3.3$ nm. For comparison, we also included a seeded FEL simulation (see Table 8.1).

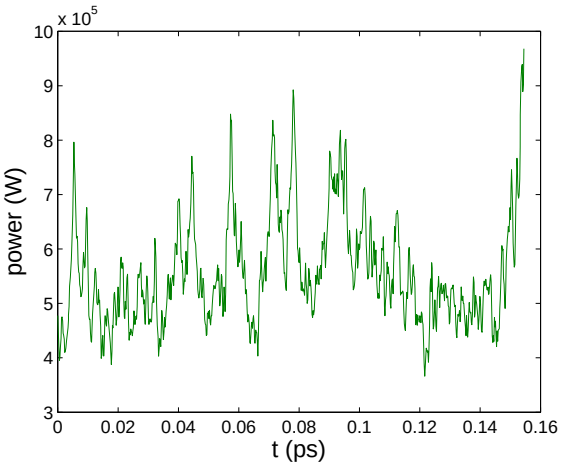

Figure 8.3: Instantaneous power at $z = 100$ m for a small section (about 1%) of the entire SASE pulse.

a peak magnetic field on the order of 1 T for the 100-m long undulator, the effects of a spontaneous undulator radiation are almost equivalent to those of the damping wigglers for the ultra-low emittance PEP ring. Such a long undulator eliminates the requirement for a large number of the damping wigglers, but the remaining damping wigglers must be adjustable in their field strengths to compensate for the change of the spontaneous radiation level due to undulator gap variations (for FEL wavelength tuning). For a permanent-magnet undulator having 5-cm in period, the full undulator gap is slightly above 1 cm to generate ~ 1 T on-axis magnetic field. The resulting transverse resistive wall wakefield in a 100-m small-gap vacuum chamber (or in the conducting image charge sheets for an in-vacuum undulator) may be a concern for multi-bunch instability. Preliminary estimates of the resistive wall instability for 1.5 A average current in this ring shows that it may be cured by a narrowband feedback system. Further studies are necessary to make a practical design of a high-gain FEL in PEP-X.

8.2 Acknowledgments

We would like to thank Tom Knight for carefully reading the manuscript prior to its publication.

Bibliography

[1] G. Hoffstaeter, presentation for the 37th ICFA Advanced Beam Dynamics Workshop on Future Light Sources, Hamburg, (2006).

[2] G. Hoffstaeter *et al.*, Proceedings of 27th Particle Accelerator Conference, Albuquerque, (2007).

[3] Y. Cai, *et al.*,"A Modular Accelerator Design Code", SLAC–PUB–7642 (1997).

[4] "Handbook of Accelerator Physics and Engineering", edited by A. Chao and M. Tigner, World Scientific Publishing, p. 189 (2002).

[5] http://mad.web.cern.ch/mad/mad8web/mad8.html .

[6] Karl L. Brown, Roger V. Servranckx,"Optics Modules for Circular Accelerator Design", NIM A258, pp.480-502 (1987).

[7] L. Smith, "Effect of wigglers and undulators on beam dynamics", LBNL ESG TECH NOTE-24 (1986).

[8] P. Elleaume, "A new approach to the electron beam dynamics in undulators and wigglers", EPAC 92 (1992)

[9] A. Terebilo, "Accelerator Modeling with Matlab Accelerator Toolbox", PAC' 01, Chicago (2001)

[10] NSLS-II Conceptual Design Report, December (2006).

[11] J.D. Bjorken and S.K. Mtingwa, Particle Accelerators **13**, 115 (1983).

[12] S. Nagaitsev, Phys. Rev. ST-AB **8**, 064403 (2005).

[13] K. Bane, in Proceedings of 8th European Particle Accelerator Conference, Paris, (2002).

[14] T. Raubenheimer, Particle Accelerators **45**, 111 (1994).

[15] K. Kubo and K. Oide, Phys. Rev. ST-AB **4**, 124401 (2001).

[16] H. Brück, Accelérateurs Circulaires de Particules, PUF (1966).

[17] A. Piwinski, in *Handbook of Accelerator Physics*, 3rd Printing, p. 142. (World Scientific, New Jersey, 2006)

[18] C.Rivetta,T.Mastorides,J.DFox,D.VanWinkle, SLAC-TN-08–003 December (2008).

[19] M.Neubauer,M.Allen,K.Fant,A.Hill,M.Hoyt,J.Judkins,H.Schwarz, A.Rimmer,SLAC-PUB-7209 June (1996).

[20] R.A.Rimmer,J.M.Byrd,D.Li, Phys. Rev. ST Accel. Beams **3**, 102001 (2000).

[21] P.McIntosh,S.Allison,P.Bellomo,A.Hill,S.Park,V.Pacak,J.Sebek, D.Sprehn, Proceedings of EPAC 2004, p.1084,Lucerne, Switzerland, (2004).

[22] R.Pendleton,K.Ko,C.Ng,M.Neubauer,H.Schwarz,R.Rimmer, Proceedings of PAC 1995, p.1800,Dallas, Texas, (1995).

[23] A. Candel et al., "Parallel higher-order finite-element method for accurate field computations in wakefield and PIC simulations", SLAC-PUB-13667, June (2009).

[24] A. Chao and M. Tigner, eds., *Handbook of Accelerator Physics*, 3rd Printing, pp. 230–237 (World Scientific, New Jersey, 2006)

[25] K. Yokoya, "Resistive wall impedance of beam pipes of general cross-section", KEK Preprint 92–196, February (1993).

[26] R.A Rimmer et al., "Updated impedance estimate of the PEP-II rf cavity", SLAC-PUB-95-7089, December (1995).

[27] Y. Cai, "A Vlasov-Fokker-Planck Solver for Longitudinal Dynamics", unpublished, (2008).

[28] , G. Stupakov and I. Kotelnikov, "Calculation of Coherent Synchrotron Radiation Impedance Using the Mode Expansion Method", Phys. Rev. ST Accel. Beams **12**, 104401 (2009).

[29] A. Chao, Physics of Collective Beam Instabilities in High Energy Accelerators, Wiley-Interscience Publication, John Wiley & Sons, Inc., (1992).

[30] S. Krinsky, in the proceedings of PAC07, TUPMS074, (2007).

[31] Kohtaro Satoh and Y. Chin, Nucl. Instr. And Meth. V207, p309, (1983).

[32] A. Wolski, J. Gao and A. Guiducci, editors. "Configuration Studies and Recommendations for the ILC Damping Rings", LBNL59449, (2006).

[33] T. Raubenheimer and F. Zimmermann, Phys. Rev. E52, No. 5, 5487 (1995).

[34] G.V. Stupakov, Proc. Int. Workshop on Collective Effects and Impedance for B-Factories KEK Proc. 96-6, p243 (1996).

[35] L. Wang, Y. Cai and T. Raubenheimer, in the Proceedings of PAC2007, FRPMS080, (2007).

[36] Z. Huang *et. al.*, Nucl. Instrum. Method A **593**, 120 (2008).